

In presenting this thesis in partial fulfillment of the requirements for an advanced degree at Idaho State University, I agree that the Library shall make it freely available for inspection. I also state that permission to download and print my thesis for scholarly purposes may be granted by the Dean of the Graduate School, Dean of my academic division, or by the University Librarian. Copying or publication of this dissertation for financial gain shall not be allowed without my written permission.

Signature _____

Date _____

LOCALIZED LATE MIOCENE FLEXURE NEAR THE WESTERN MARGIN OF THE EASTERN
SNAKE RIVER PLAIN, IDAHO, CONSTRAINED BY REGIONAL CORRELATION OF SNAKE
RIVER-TYPE RHYOLITES AND KINEMATIC ANALYSIS OF SMALL-DISPLACEMENT FAULTS

by

Kyle L. Schusler

A thesis

submitted in partial fulfillment

of the requirements for the degree of

Master of Science in the Department of Geosciences

Idaho State University

Spring 2018

To the Graduate Faculty:

The members of the committee appointed to examine the thesis of Kyle L. Schusler find it satisfactory and recommend that it be accepted.

Dr. David M. Pearson – Primary advisor

Dr. Michael McCurry – Committee Member

Dr. René G. Rodriguez – Graduate Faculty Representative

ACKNOWLEDGEMENTS

First and foremost, I thank Dr. David M. Pearson for his guidance, patience, and countless hours of pushing me to complete this research. Thank you for invaluable assistance with writing this thesis, improving my field skills, and always being a supportive advisor throughout this project. I also thank Dr. Mike McCurry for always helping me with thin section analyses, and providing me the key concepts to understand geochemistry, and improving my laboratory skills throughout my time at ISU. Lastly, I thank Dr. René Rodriguez for providing his assistance to this project and being part of this committee. Words cannot describe my appreciation with everything my committee has done for me.

A very special thanks to Roy Bartholomay and Mary Hodges with their never-ending guidance with thesis writing, core description, understanding key concepts of the eastern Snake River Plain aquifer, and providing invaluable feedback on the interpretations of my thesis. Their never-ending support has given me the drive to accomplish a task that seemed impossible at first.

This project was funded by a grant from the USGS (RGE02A) with cooperation with the DOE. Without these funds, I would not have been able to complete this thesis.

Thank you to Diana Boyack, Kate Zajanc, Melissa Neiers, Breane Fitzgerald, and the rest of the office staff for always helping me out with printing, DML anomalies, and keeping my eye on the ball.

Thanks to all of my friends at ISU, who have made these two years an amazing adventure filled with hiking, mountain biking, tennis, and Wacke Wednesdays.

A special thanks to Dylan Colon who processed our stable isotope analyses, and provided valuable information of the fractionation factors of minerals in a rhyolite melt. In

addition, I would like to thank Mark Anders and Tanzhuo Liu for their ongoing collaboration and for running our eruption age dating.

This research relied heavily on the academic license for Move (2017.2) provided by Midland Valley. Thank you to Midland Valley for providing a user-friendly software that helped me produce 3D models of the subsurface architecture of the eastern Snake River Plain.

In addition, I used the programs FaultKin (version 7.5) and Stereonet (version 9.5), produced by Richard Allmendinger throughout this thesis project. These free and user-friendly programs are outstanding for any geologist.

Finally, I would like to thank my future wife, Nicole Volpe, who held my sanity together and gave me the drive to finish strong with my thesis. Your continuous support has made me a better man every day.

TABLE OF CONTENTS

List of Figures.....viii

List of Tables.....x

Abstract.....xi

CHAPTER 1: INTRODUCTION.....1

 1.1 Purpose and Scope.....1

 1.2 Approach4

 1.3 Geologic Background.....4

 1.3.1 ESRP Volcanism.....4

 1.3.2 Structural Geology of the ESRP and Adjacent Regions.....11

 1.3.3 Hydrogeologic Setting of the ESRP17

CHAPTER 2: METHODS.....20

 2.1 Overview.....20

 2.2 Rhyolite Correlations.....20

 2.2.1 Thin section Analysis.....20

 2.2.2 U-Pb Zircon Geochronology and Lu-Hf Isotopic Analysis.....21

 2.2.3 Ar-Ar Geochronology.....22

 2.2.4 $\delta^{18}\text{O}$ Isotope Analysis.....23

 2.2.5 XRF Analysis.....25

 2.3 Structural Analysis.....25

 2.3.1 Data Collection in the Field.....26

 2.3.2 Analysis of Fault Data.....28

2.4 Cross Section from the Arco Hills through Deep Boreholes.....	34
CHAPTER 3: RESULTS.....	36
3.1 Results for Rhyolite Analysis.....	36
3.1.1 Macroscopic and Microscopic Observations.....	36
3.1.2 Phenocryst Textures.....	40
3.1.3 U-Pb Zircon Geochronology and Hf Analysis.....	48
3.1.4 Ar-Ar Geochronology.....	50
3.1.5 $\delta^{18}\text{O}$ Isotope Analysis.....	51
3.1.5 XRF Analysis.....	53
3.2 Results for Fault Analysis.....	58
3.2.1 Collective Analysis of Northeast-Striking Faults.....	58
3.2.2 Spatial Pattern in Brittle Deformation.....	63
CHAPTER 4: DISCUSSION.....	70
4.1 Rhyolite Correlation.....	70
4.1.1 Rhyolite of USGS-142.....	75
4.1.2 Rhyolite of Butte Quarry.....	78
4.1.3 Rhyolite of the East Side of the Arco Hills.....	81
4.2 Kinematic Analysis of Northeast-striking Faults.....	83
4.3 Geometry of the Western Boundary of the ESRP near the Arco Hills.....	86
4.3.1 Subsurface Architecture of the ESRP.....	88
4.4 Implications for the Hydrogeology of the Western Idaho National Laboratory...89	
4.5 Implications for the Subsidence of the Eastern Snake River Plain.....	91
4.5.1 Estimation of the Amount of Subsidence of the ESRP.....	91

4.5.2 Implications for Flexure along the Margins of the ESRP	93
4.5.3 Migration of the Flexural Hinge Line.....	97
CHAPTER 5: CONCLUSIONS.....	103
CHAPTER 6: SUGGESTIONS FOR FUTURE WORK.....	105
REFERENCES.....	108
Appendices.....	118
Appendix A: Zircon Separation.....	118
Appendix B: Separating Phenocrysts from Vitrophyre Using HF Dissolution.....	120
Appendix C: Method for Calculating $\delta^{18}\text{O}$ of Melt from $\delta^{18}\text{O}$ of Phenocrysts.....	123
Appendix D: Simplified Stratigraphic Column of Borehole USGS-142.....	125
Appendix E: Eigenvalues used for Calculating Fabric Shape.....	126
Appendix F: Raw data for Ar-Ar age dating.....	127
Appendix G: Measured northeast-striking faults of the Arco Hills.....	128
Appendix H: Data Tables for U-Pb, Hf, and CL Images of Zircons.....	129

LIST OF FIGURES

1.1 Study area.....	3
1.2 Location of volcanic fields and the seismic parabola.....	8
1.3 Schematic representation of a caldera.....	11
1.4 Areas previously researched for flexure.....	15
2.1 Fault surface.....	27
2.2 Offset marker bed.....	28
2.3 Representation of a synthetic fault plane solution.....	29
2.4 Illustration of clustered vs. girdled fabric shapes.....	30
2.5 Division of fault data.....	32
2.6 Schematic representation of rotated fault planes.....	33
2.7 Location of section trace.....	35
3.1 Phenocrysts found in the rhyolite of USGS-142.....	44
3.2 Phenocrysts found in the rhyolite of Butte Quarry.....	45
3.3 Phenocrysts found in the West Pocatello rhyolite.....	47
3.4 Weighted mean average U-Pb zircon age of the rhyolite of USGS-142.....	49
3.5 Weighted mean average U-Pb zircon age of the rhyolite of Butte Quarry.....	50
3.6 Plot of calculated $\delta^{18}\text{O}$ melt values.....	52
3.7 Spider diagram of major element geochemistry of the rhyolite of USGS-142.....	54
3.8 Spider diagram of major element geochemistry of the rhyolite of Butte Quarry.....	55
3.9 Stereogram for all measured faults.....	59
3.10 Hand sample of microcrystalline breccia.....	60
3.11 Stereogram for northeast-striking faults.....	61

3.12	Fault plane solution for northeast-striking faults.....	62
3.13	Location of measured northeast-striking faults in the Arco Hills.....	64
3.14	Fault plane solution for northeast-striking faults in the distal domain.....	65
3.15	Fault plane solution for northeast-striking faults in the proximal domain.....	65
3.16	Mean vector analysis of shortening axes.....	67
3.17	Stereograms of northeast-striking faults	69
4.1	Cross section A-A'	89
4.2	Cumulative tilting plots.....	95
4.3	Schematic representation of a migrating flexural hinge line.....	99
4.4	3D block model of the temporal evolution of the ESRP.....	101
4.5	Schematic cross sections for the temporal evolution of the ESRP.....	102

LIST OF TABLES

1.1 Locations and elevations of deep boreholes.....	19
3.1 Point counting results.....	40
3.2 Ar-Ar age dating results.....	51
3.3 $\delta^{18}\text{O}$ results.....	52
3.4 Trace element geochemistry of the rhyolite of USGS-142.....	56
3.5 Trace element geochemistry of the rhyolite of Butte Quarry.....	57
3.6 Fit and habit of shortening and extension axes for collective fault analysis.....	62
3.7 Mean vector analysis of poles to fault planes in each fault domain.....	66
3.8 Fit and habit of kinematic axes and poles to fault planes in each fault domain.....	68
4.1 Data compilation of Snake River-type rhyolites.....	71
4.2 Snake River-type rhyolite whole rock geochemistry data compilation.....	73
4.3 Correlation matrix for the rhyolite of USGS-142.....	78
4.4 Correlation matrix for the rhyolite of Butte Quarry.....	81
4.5 Correlation matrix for the rhyolite of the east side of the Arco Hills.....	82
4.6 Table of elevations of selected subsurface rhyolites.....	92

LOCALIZED LATE MIOCENE FLEXURE NEAR THE WESTERN MARGIN OF THE EASTERN
SNAKE RIVER PLAIN, IDAHO, CONSTRAINED BY REGIONAL CORRELATION OF SNAKE
RIVER-TYPE RHYOLITES AND KINEMATIC ANALYSIS OF SMALL-DISPLACEMENT FAULTS

Thesis Abstract – Idaho State University (2018)

This research involved the investigation of the geometry of subsurface Snake River-type rhyolites near the western margin of the eastern Snake River Plain (ESRP). A recently drilled rhyolite in borehole USGS-142 is tentatively correlated to the Walcott Tuff B in borehole WO-2. Another rhyolite, exposed at the surface southeast of Arco, Idaho, dips 20° south toward the ESRP, and is tentatively correlated to the uppermost Picabo-aged rhyolite found in borehole INEL-1. These correlations suggest that the tilts of surface and subsurface rhyolites must shallow toward their correlative units from the margin to the center of the ESRP; the tilts of subsurface rhyolites are localized near the margin of the ESRP and northern Basin and Range.

This research also involved a kinematic analysis of northeast-striking, small-offset faults due east of Arco, Idaho as a basis for inferring the tectonic evolution of the western margin of the ESRP. Northeast-striking faults record nearly pure dip-slip offset and a northwest-southeast extension direction. In addition, faults proximal to the ESRP record a northwest-plunging extension direction, whereas faults distal to the ESRP record a shallowly southeast-plunging extension direction. These observations suggest that the northeast-striking faults likely formed as a result of early stages of flexure from the subsidence of the ESRP and were later rotated similarly to Mesozoic fold-hinges.

Key words: Eastern Snake River Plain, Snake River-type Rhyolites, Flexure, Kinematic Analysis, Eastern Snake River Plain Aquifer.

CHAPTER 1: INTRODUCTION

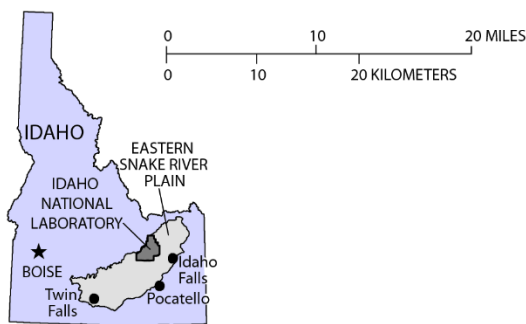
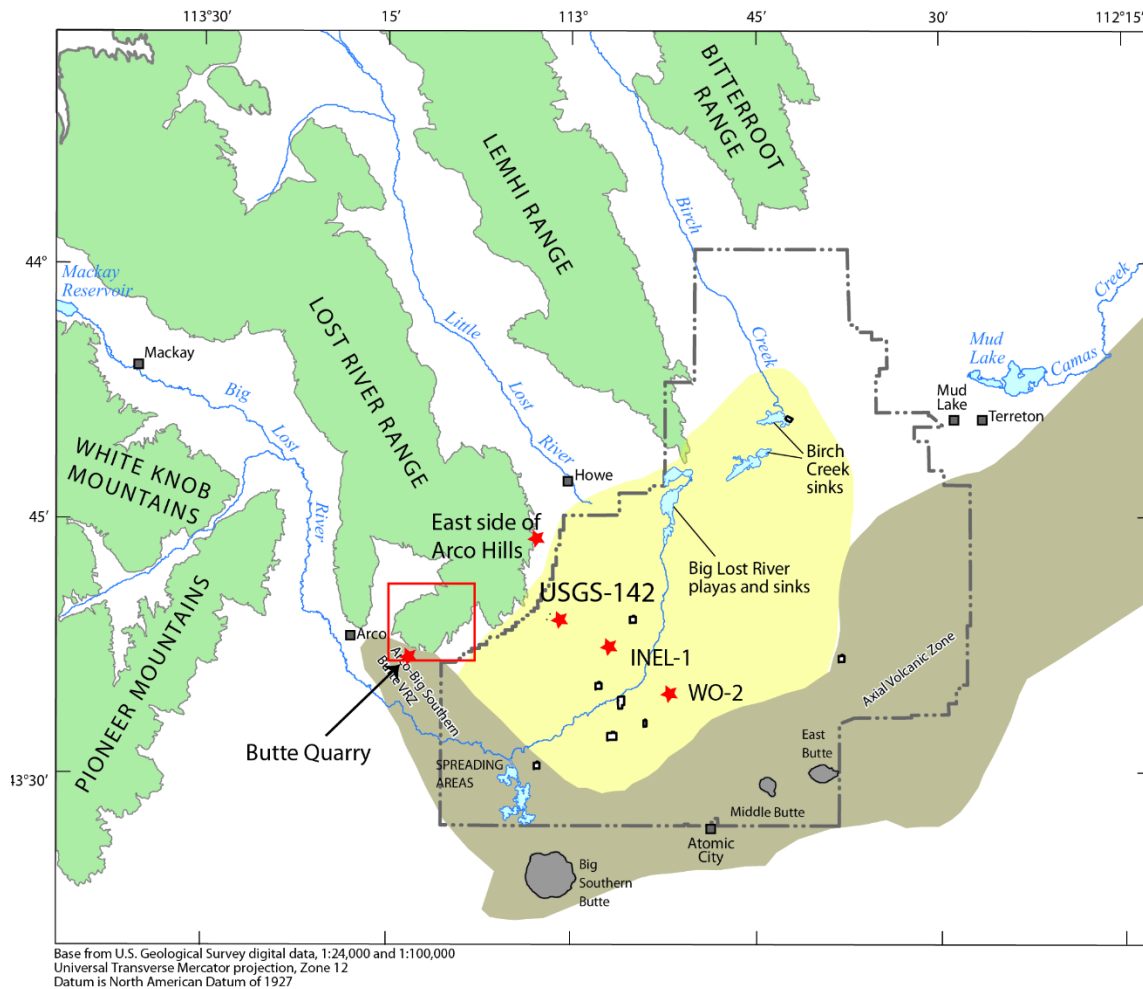
1.1 Purpose and Scope

The eastern Snake River Plain (ESRP) is a northeast-trending volcanic province that is interpreted to represent the North American plate's migration over the stationary Yellowstone hotspot (e.g. Anders et al., 1989; Pierce and Morgan, 1992; Branney et al., 2008, and references cited therein). The Idaho National Laboratory (INL) is located in the west-central portion of the ESRP (Fig. 1.1), and lies over one of the most productive aquifers in the United States (U.S. Geological Survey, 1985). The U.S. Geological Survey (USGS) has collected borehole information at the INL in order to investigate the subsurface stratigraphy of the ESRP and to characterize the ESRP aquifer with respect to the migration of radioactive and chemical wastes (e.g. Bartholomay et al., 2017). Most of the water in the ESRP aquifer flows through basalt, which is inferred to be underlain by rhyolite throughout the ESRP (Doherty et al., 1979; Mazurek, 2004; McCurry et al., 2016; Twining et al., 2017). Basalt and sedimentary rocks thin toward the western INL (Doherty et al., 1979; Mazurek, 2004; Twining et al., 2017), so the ESRP aquifer is likely in contact with subsurface rhyolite in the western INL. However, the geometry of the basalt-rhyolite contact throughout much of the west-central ESRP is poorly constrained.

One major goal for this project was to determine the geometry of the basalt-rhyolite contact in the western INL. This was accomplished by correlating subsurface and surface rhyolites to rhyolites found in deep boreholes at the INL (Fig. 1.1). Not only does this provide insight into the nature of the basalt-rhyolite contact in the subsurface of the western INL, but it also constrains the subsidence evolution of the ESRP in this region, namely whether a fault down-dropped the ESRP relative to the northern Basin and Range

tectonic province. A faulted boundary between these two provinces would suggest through going fractures in the generally impermeable subsurface Snake River-type rhyolites (Mann, 1986) and provide a potential conduit for fluid exchange between the ESRP aquifer and geothermal waters below the ESRP aquifer in the western portion of the INL. In contrast, an unfaulted boundary may effectively seal lower geothermal waters.

In addition to correlating subsurface and surface rhyolites to determine the subsurface geometries of rhyolites in the ESRP, this research also investigated surficial faulting in the Arco Hills to evaluate its role in contributing to 1) lateral displacement of the ESRP relative to the adjacent Basin and Range province (Payne et al., 2012) or 2) the subsidence and tectonic evolution of the ESRP (Fig. 1.1). Steeply-dipping (70° - 90°), small offset (≤ 100 m) northeast-striking faults occur ≤ 30 km from the margins of the ESRP (Allmendinger, 1982; Zentner, 1989; Rodgers et al., 2002). Several hypotheses have been proposed for the formation of the northeast-striking faults such as: a response to flexure from the subsidence of the ESRP (Zentner, 1989; Rodgers et al., 2002), accommodation of lateral displacement between the ESRP and the northern Basin and Range (Payne et al., 2012), ring fractures associated with caldera subsidence (Morgan et al., 1984), or accommodation of an along-strike decrease in slip of Basin and Range faults as they approach the ESRP (Bruhn et al., 1992). Paleozoic sedimentary rocks exposed northwest of the INL in the Arco Hills (Fig. 1.1) are offset by several northeast-striking faults (Skipton et al., 2009), so the Arco Hills provides a useful area to investigate the regional significance of these faults.



EXPLANATION

- Selected facilities at the Idaho National Laboratory
- - - Idaho National Laboratory boundary
- Big Lost Trough
- Approximate area of Volcanic Rift Zones (VRZ) and Axial Volcanic Zone - contact inferred
- Pleistocene rhyolite dome

Figure 1.1: Geographic location of the borehole USGS-142, rhyolite of Butte Quarry, rhyolite of the east side of the Arco Hills, borehole INEL-1, and borehole WO-2 (red stars). The light red box outlines the area where fault data were collected (Chapter 2). Figure modified from Twining et al. (2017).

1.2 Approach

This research sought to investigate the temporal evolution of the ESRP with regards to both the geometries of subsurface rhyolites and the interpreted regional significance of northeast-striking faults.

- I. To determine the geometry of the basalt-rhyolite contact in the subsurface of the ESRP in the western INL, this research involved correlation of a subsurface rhyolite found in borehole USGS-142 and surface rhyolites exposed near the Arco Hills (Fig. 1.1) to previously analyzed rhyolites found along the ESRP. Thin section analysis, U-Pb zircon geochronology, Ar-Ar sanidine geochronology, and radiogenic and stable isotope analyses were used for correlation.
- II. This research also involved a kinematic analysis of northeast-striking faults that occur in the Arco Hills to evaluate their regional structural significance to the development and subsidence of the ESRP.

1.3 Geologic Background

1.3.1 Eastern Snake River Plain Volcanism

From mid-Miocene to present, voluminous silicic eruptions emplaced rhyolitic lavas and tuffs along the margins and within the ESRP that generally decrease in age from the McDermitt volcanic field (~16 Ma; Coble and Mahood, 2012) toward present-day Yellowstone (Fig. 1.2; Pierce and Morgan, 1992). The ESRP contains products of “Snake River-type” super eruptions, which produced rhyolitic, high-temperature, intensely welded and often rheomorphic “lava-like” ignimbrites, thick ash fall deposits, and some lava flows (Branney et al., 2008). Snake River-type rhyolitic ignimbrites are a product of pyroclastic density currents, and are thought to have blanketed the margins and interior of the ESRP in

voluminous (tens to thousands km³) and regional sheet-like deposits (Branney et al., 2008). In contrast, rhyolitic lavas are thought to have been erupted from nearby vents and are products of localized eruption events. Both Snake River-type ignimbrites and lava flows are typically bounded by an upper and lower vitrophyre, which are glassy portions of the unit produced from the thermal contrast between their high-temperature of deposition and the cooler country rock and ambient air. Between the vitrophyres is a central microcrystalline (lithoidal) center zone, which consists of the devitrified interior of an ignimbrite or lava flow (Branney et al., 2008).

Time-transgressive clusters of overlapping and nested calderas are interpreted to constitute each volcanic field along the track of the ESRP (Bindeman et al., 2007; Drew et al., 2013). Near the Arco Hills, eruptions from the Picabo (~10-7 Ma) and Heise (~7-4 Ma; Morgan and McIntosh, 2005) volcanic fields likely emplaced Snake River-type rhyolites in the western INL. Basalt flows conceal these rhyolitic volcanic fields, so the geographic extents of Snake River-type rhyolites and their calderas have been inferred from surficial exposures and cored subsurface rhyolitic ignimbrites and lava flows (e.g. Anders et al., 2014).

Snake River-type rhyolites are exposed along the margins of the ESRP and were encountered by deep boreholes that penetrate subsurface rhyolites, such as INEL-1, WO-2, and more recently, USGS-142 (Fig. 1.1). A 150 m thick rhyolite was encountered at the base of the 573 m deep borehole USGS-142 (hereby referred to as the “rhyolite of USGS-142”); the base of this rhyolite was not encountered (Twining et al., 2017). Petrographic examinations of the upper and lower portions of this rhyolite documented eutaxitic textures, which indicate a pyroclastic origin (McCurry et al., 2016). Preliminary

examination of the major and trace element geochemistry and petrography by McCurry et al. (2016) indicated that the rhyolite of USGS-142 was not correlative to any major Heise ignimbrites. Further analysis of the rhyolite of USGS-142 was accomplished for this study in order to provide a robust correlation to previously studied rhyolites along the margins and in the subsurface of the ESRP.

A surface rhyolite exposed southeast of Arco (Fig. 1.1; hereby referred to as “the rhyolite of Butte Quarry”) was also analyzed in this research. The rhyolite of Butte Quarry crops out just south of the Arco Hills and dips 20° south (Fig. 1.1). In addition, this research also involves investigation of a rhyolite exposed on the eastern side of the Arco Hills (Fig. 1.1; hereby referred to as the “rhyolite of the east side of the Arco Hills”). Correlation of these rhyolites exposed at the surface to other subsurface rhyolites provides a useful constraint on the continuity and geometry of subsurface rhyolites within the west-central INL.

1.3.1.1 Volcanic fields

The presumed Picabo and Heise volcanic fields were previously interpreted to occur southwest and northeast, respectively, of the Arco Hills (Fig. 1.2) and follow the northeast trending time-transgressive nature of the ESRP (Fig. 1.2; Anders et al., 1989). The Picabo volcanic field ignimbrites range in eruption age from 10.41 ± 0.01 Ma to 7.58 ± 0.01 Ma (Anders et al., 2014). The northern extent of the Picabo volcanic field is thought to occur south of the Arco Hills (Fig. 1.2), based largely on the correlation between the West Pocatello rhyolite and the uppermost Picabo-age ignimbrite found in deep borehole INEL-1 (found at a depth of 3686' below land surface; Drew et al., 2013).

Within each of these volcanic fields, prior workers have utilized distinct $\delta^{18}\text{O}$ stable isotopic analyses of individual phenocrysts to further fingerprint magma sources and to provide constraints on the chemistry and petrogenesis of the magma chambers. Within Picabo-aged units, Drew et al. (2013) demonstrated that $\delta^{18}\text{O}$ stable isotopes of volcanic phenocrysts progressively decrease with time. The Arbon Valley Tuff, the first regional eruption of the Picabo volcanic field (~ 10.44 Ma U-Pb zircon geochronology age), produced a high value of $\delta^{18}\text{O}$ (+7.9 to +8.3‰); later eruptions, such as the West Pocatello rhyolite (~ 8.25 Ma U-Pb zircon geochronology age), produced a lower value of $\delta^{18}\text{O}$ (+3.3‰). The progressive decrease in $\delta^{18}\text{O}$ in younger Picabo-aged rhyolites was interpreted by Drew et al. (2013) to reflect recycling of hydrothermally altered intracaldera rhyolites from continued caldera subsidence in the Picabo volcanic field, which would allow older rhyolites to be reincorporated into younger magma chambers prior to their eruptions.

The Heise volcanic field is thought to occur northeast of the Picabo volcanic field (Fig. 1.2). The Heise ignimbrites range in eruption age from 6.66 ± 0.01 Ma to 4.61 ± 0.01 Ma (Anders et al., 2014). Similarly to the Picabo volcanic field, phenocrysts in Heise volcanic units were also shown to decrease in $\delta^{18}\text{O}$ with progressively younger eruptions (Bindeman et al., 2007; Watts et al., 2011). For example, the Blacktail Creek Tuff, the first eruption of the Heise volcanic field (~ 6.92 Ma U-Pb zircon geochronology age), produced a $\delta^{18}\text{O}$ value of +6.6‰ (Watts et al., 2011) to +6.0‰ (Bindeman et al., 2007). A younger Heise ignimbrite, the Kilgore Tuff (~ 4.59 Ma U-Pb zircon geochronology age), produced a lower $\delta^{18}\text{O}$ value of +3.3‰ (Bindeman et al., 2007). Bindeman et al. (2007) interpreted that this temporal trend reflects recycling of hydrothermally altered intracaldera rhyolites.

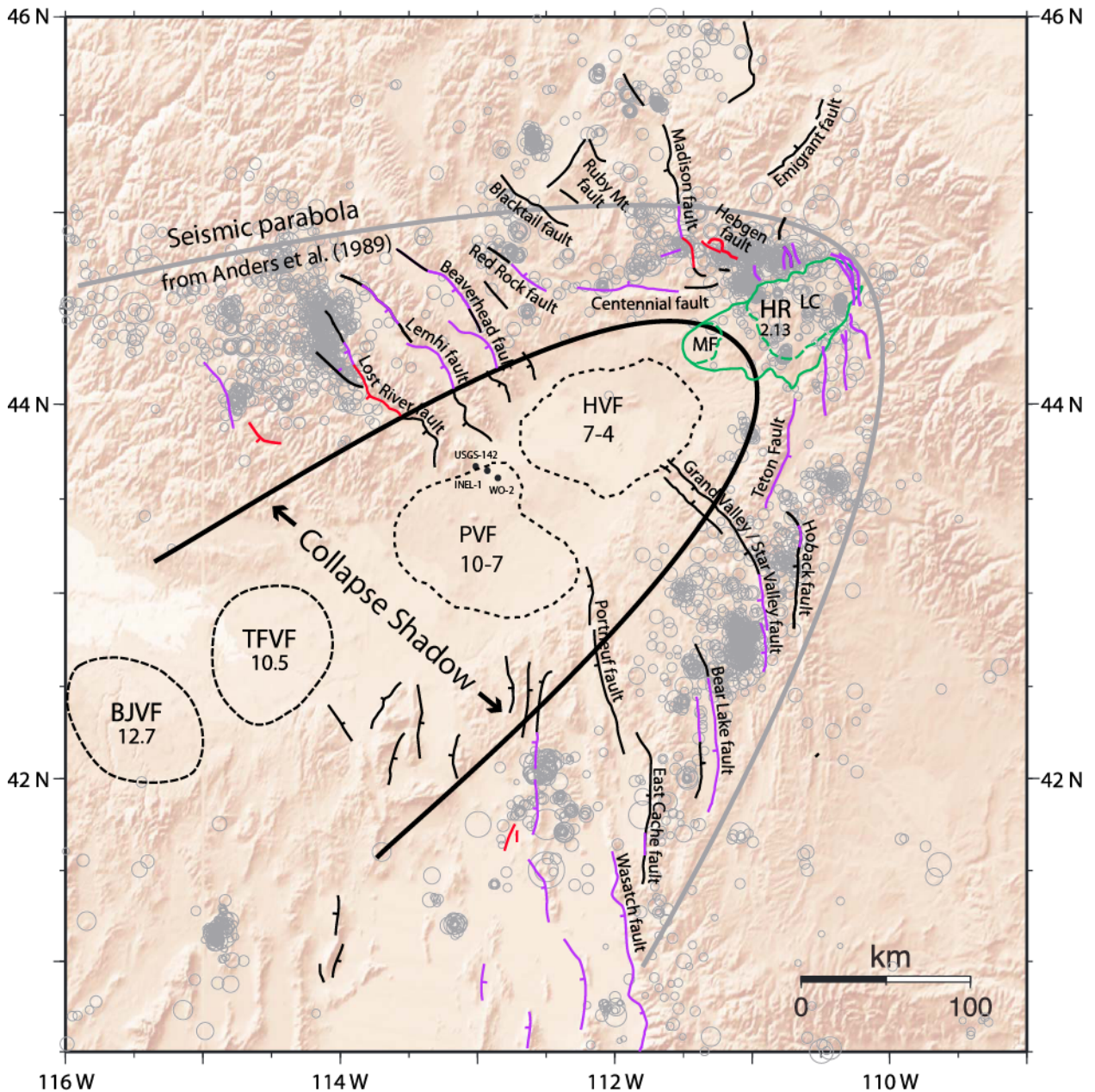


Figure 1.2: Locations of volcanic fields along the Snake River Plain, modified figure 1 from Anders et al. (2014). Projections of volcanic fields were modified from Anders et al. (2014) to include the interpreted spatial extents of several caldera locations within the associated volcanic field. Note that the Picabo Volcanic Field (PVF) is located south-southwest of the Arco Hills (southern extent of the Lost River Fault). The Centennial fault is located northeast of the Arco Hills, which is thought to be accommodating right-lateral strike-slip deformation associated with the Centennial shear zone (Payne et al., 2012). Active faults are colored purple and red, whereas the faults labeled in black were most recently active in the Neogene to the latest Quaternary. BJVF (Bruneau-Jarbidge volcanic field), TFVF (Twin Falls volcanic field), PVF (Picabo volcanic field), HVF (Heise volcanic field), HR (Huckleberry Ridge Tuff), MF (1.30 Ma Mesa Falls), and LC (649 ka Lava Creek). The outer

seismic parabola is outlined in gray, and the inner parabola is outlined in black; areas inside the inner parabola are referred to as the “collapse shadow” (Anders et al., 1989). USGS-142, INEL-1, and WO-2 deep boreholes are located in the northern portion of the Picabo volcanic field.

Calderas form in response to rapid and voluminous magma evacuation from the middle crust, creating an overlying subsided region (Branney and Acocella, 2015), which occurs inboard of steeply dipping faults that define a ring fracture zone (Fig. 1.3). A ring fracture zone is thought to produce regionally curved and steeply dipping ($\geq 70^\circ$) faults during caldera subsidence. A collar zone forms outside of a caldera due to instability of the rock that surrounds the subsided region (Fig. 1.3) from removal of material via mass wasting (Lipman, 1997). The Yellowstone caldera (0.64 Ma) and the Island Park caldera (1.3 Ma) provide examples of recent caldera subsidence along the hotspot track in the present-day Yellowstone volcanic field (Christiansen, 2001).

According to Branney and Acocella (2005), ignimbrites extruded from a caldera largely infill the subsided caldera floor (intracaldera), but some flows travel away from the caldera as outflow sheets (Fig. 1.3). Intracaldera ignimbrites are typically thicker, more intensely welded, and show higher grades of hydrothermal alteration compared to outflow ignimbrites (Branney and Acocella, 2015). Although ignimbrites are thought to be regional sheet-like deposits along the track of the ESRP, calderas may provide a localized zone of accommodation space where ignimbrites may be substantially thicker.

Caldera subsidence has been suggested as a possible mechanism for ESRP subsidence (e.g. Morgan et al., 1984; Branney et al., 2008), given that extensive rhyolitic ignimbrite sheets along the margins of the ESRP have no apparent sources (Morgan et al., 1984), yet volumes of these eruptions are estimated to range from $\sim 300 \text{ km}^3$ to 1800 km^3

(Morgan and McIntosh, 2005). Voluminous eruptions on the ESRP are hypothesized to have produced 1-3 km deep calderas that can be 20 to 50 km across (Morgan and McIntosh, 2005; McCurry et al., 2016), potentially overlapping the Basin and Range province north of the ESRP. This was suggested by Morgan et al. (1984), who interpreted northeast-striking faults affecting Heise-aged rhyolites at the southern tip of the Lemhi Range as ring-fracture faults associated with caldera subsidence.

The locations of ESRP calderas are mostly inferred from the spatial distributions of their ignimbrites, and from a few deep boreholes at the INL that have penetrated the thick and hydrothermally-altered subsurface rhyolites. Previous researchers assigned depositional environments for these flows based largely on their thicknesses and degrees of alteration (e.g. Drew et al., 2013; Anders et al., 2014). For example, Drew et al. (2013) hypothesized that the ~2 km thick package of hydrothermally altered Picabo-aged rhyolite at the base of borehole INEL-1 was a localized zone of subsidence, where statistically indistinguishable U-Pb zircon age ignimbrites infilled a subsided caldera and were later hydrothermally altered.

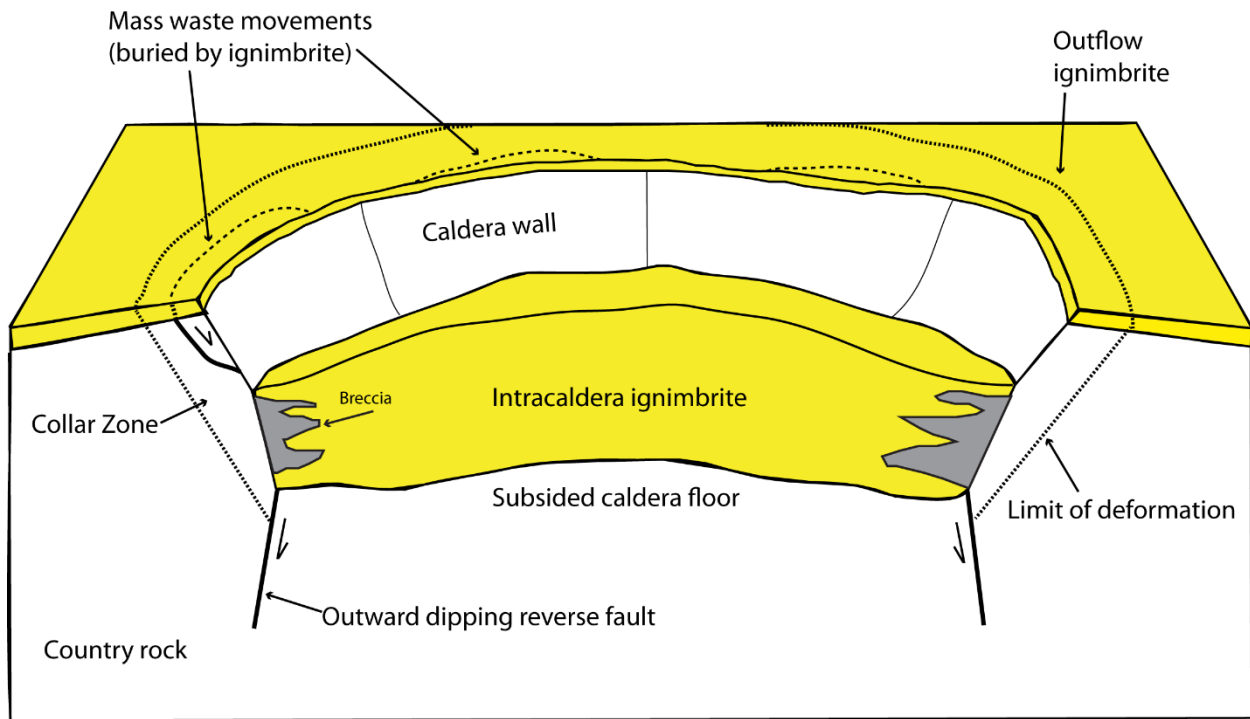


Figure 1.3: Schematic representation of a caldera. Modified from Branney and Acocella (2005).

1.3.2 Structural Geology of the Eastern Snake River Plain and Adjacent Regions

1.3.2.1 Pre-Neogene deformation

During Mesozoic time, shortening in east-central Idaho was accommodated by east-verging folds and west-dipping thrust faults (Skipp, 1988). Map-scale folds with wavelengths ranging from 250 to 3000 m involve rocks of Mississippian through Permian age north of the ESRP, and were interpreted to have been originally horizontal after shortening ceased (McQuarrie and Rodgers, 1998).

Following Mesozoic crustal shortening, Eocene volcanism and northwest-southeast-directed extension associated with Challis volcanism occurred dominantly north of the given study area (Janecke, 1992). However, the Arco Pass fault system, located on the western margin of the study area, is inferred to have been active in Eocene-Oligocene time

because basin fill adjacent to the Arco Pass fault is composed of dominantly Challis-aged volcanic clasts (Janecke, 1995; Link and Janecke, 1999; Skipp et al., 2009). The Arco Pass fault system is north-northeast striking and dips primarily to the northwest (Skipp et al., 2009); these faults may have deformed the western margin of the study area in the southern Arco Hills (Fig. 1.1).

1.3.2.2 Northern Basin and Range extension

North of the ESRP, high-angle, northwest-striking Basin and Range normal faults accommodate active crustal extension (Fig. 1.2). The range-bounding faults become less recently active as they approach the boundary of the ESRP (Bruhn et al., 1992). The Lost River, Lemhi, and Beaverhead faults may transition within the ESRP into volcanic rift zones that are defined by similarly-oriented vents, fractures, and minor faults (Kuntz et al., 2002; Rodgers et al., 2002). Basin and Range extension surrounding the ESRP began ~16 Ma and continues presently (Rodgers et al., 2002). Most seismic activity occurs outboard of the margins of the ESRP (Fig. 1.2; Anders et al., 1989). At a regional scale, the distribution of earthquake epicenters forms a parabolic shape centered about the axis of the eastern Snake River Plain (Fig. 1.2); this is thought to represent an area of active brittle deformation surrounding an area of no brittle deformation (Fig. 1.2; Anders et al., 1989). The area of minimal seismicity in the center of the parabola encompassing the ESRP and areas ≤ 40 km from the margin of the ESRP is referred to as the “collapse shadow” (Anders et al., 1989) (Fig. 1.2).

1.3.2.3 Flexure and subsidence of the eastern Snake River Plain

Snake River-type rhyolites infilled an actively subsiding ESRP. A model for ESRP subsidence was proposed by McQuarrie and Rodgers (1998), who documented progressive

southeastward tilting of Mesozoic fold-hinges and Miocene volcanic and volcanoclastic deposits toward the margin of the ESRP in the northern Basin and Range province. Approximately 20 km outside the margin of the ESRP (relative to the Lost River Range), these fold-hinges progressively tilt from zero to a maximum of 30 degrees, increasing toward the ESRP, which is interpreted to reflect flexure associated with 4.5 to 8.5 km of subsidence of the ESRP relative to the northern Basin and Range province (McQuarrie and Rodgers, 1998). The point where Mesozoic fold-hinges are horizontal and tilt southeast toward the ESRP is defined as the “flexural fold-hinge.” The subsidence of the ESRP has been explained by emplacement of a dense crustal sill beneath the ESRP (Sparlin and Braile, 1982, McQuarrie and Rodgers, 1998; Shervais et al., 2006). In order to produce the measured flexure, the sill is hypothesized to have a half width of 40-50 km (in map view), a thickness ranging from 17-25 km, and a density of 2.88 g/cm³ (McQuarrie and Rodgers (1998).

Lake Hills area

Michalek (2009) conducted a study in the Lake Hills area (Fig. 1.4) attempting to constrain the timing of flexure near the southern extent of the Pioneer Mountains. Michalek (2009) interpreted that crustal flexure initiated prior to the emplacement of ~9.2 Ma Snake River-type rhyolites because they display an average dip ~5° less than the maximum plunges of Mesozoic fold-hinges (15°) found 15 km east of their study area. Overlying the Mesozoic fold-hinges, ~9.2 Ma rhyolites dip 10° south, whereas overlying ~8.5 Ma rhyolites dip 7° south, which was interpreted to reflect minor flexure between 9.2 Ma to 8.5 Ma (Michalek, 2009). A 4.2 Ma basalt flow overlies the ~8.5 Ma rhyolites, and dips ~6°, so Michalek (2009) interpreted that flexure was inactive from 8.5 Ma to 4.2 Ma in the Lake

Hills area. Finally, crustal flexure must have reinitiated after 4.2 Ma to produce the tilt of the basalt flow and underlying units.

Howe Point

The Blacktail Creek Tuff (emplaced at 6.66 Ma; Anders et al., 2014) is exposed at Howe Point (Morgan et al., 1984) and was encountered at the base of borehole WO-2 (Anders et al., 2014); the structural relief (vertical elevation change) between these correlative units is ~1.5 km. Furthermore, the Blacktail Creek Tuff and Walcott Tuff (6.27 ± 0.04 Ma; Morgan and McIntosh, 2005) at Howe Point dip $\sim 12^\circ$ south, which is 18° less than the maximum plunge of Mesozoic fold-hinges (30°), suggesting that Mesozoic fold-hinges were tilted 18° prior to the emplacement of these units. Rodgers et al. (2002) concluded that flexure (and possibly subsidence of the ESRP) initiated prior to the emplacement of the Blacktail Creek Tuff and the Walcott Tuff, with some gentle flexure after their emplacement to accommodate their southward dips and structural relief from the southern Lemhi Range to borehole WO-2.

Beaverhead Mountains

Hough (2001) also conducted a study attempting to constrain the timing of flexure in the southern Beaverhead Mountains (Fig. 1.4). Hough (2001) interpreted that crustal flexure initiated prior to 10.3 Ma, given that the 10.3 Ma to 6.66 Ma Formation of Round Timber Spring (Hodges, 2006) is tilted 7° south, whereas underlying Mesozoic fold-hinges plunge 20° south-southeast; this suggests that Mesozoic fold-hinges were tilted 13° prior to the emplacement of the Formation of Round Timber Spring (10.3 Ma). Hough (2001) interpreted that there was a period of flexural quiescence from 10.3 Ma to 6.66 Ma because the Formation of Round Timber Spring, overlain by the Blacktail Creek Tuff, displayed only

disconformable contacts between units associated with this formation. Crustal flexure (and possible subsidence of the ESRP) reinitiated from 6.66 Ma to present day to produce the tilts of the Formation of Round Timber Springs and the overlying Blacktail Creek Tuff.

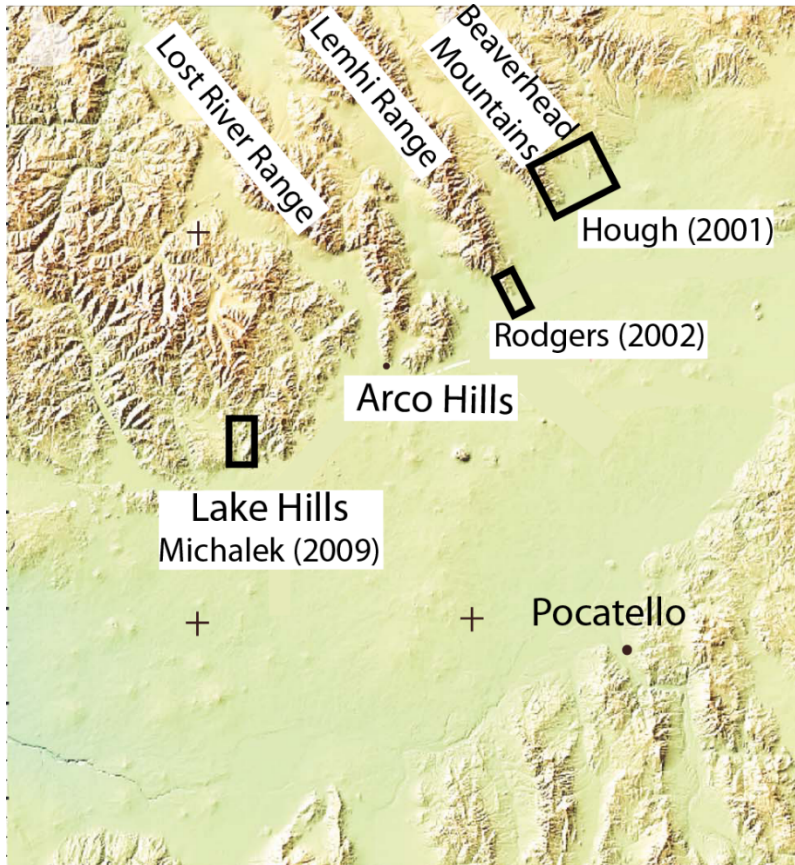


Figure 1.4: Regional map illustrating approximate field areas (black boxes) where previous research of flexure was conducted along the northern margin of the ESRP by Hough (2001), Rodgers et al. (2002), and Michalek (2009).

1.3.2.4 Northeast-striking faults

Roughly perpendicular to the Basin and Range normal faults, located ≤ 30 km from the ESRP margin, are closely spaced, northeast-striking faults that dip both toward and away from the ESRP and do not display significant vertical offset (Zentner, 1989; Rodgers et al., 2002). These faults display regionally consistent strikes ($\sim 040^\circ$ to 080° ; Allmendinger, 1982; Zentner, 1989) that are nearly parallel to the trend of the ESRP; they

offset Snake River-type rhyolites in the Blackfoot Mountains (Allmendinger, 1982), Lemhi Range (Kuntz et al., 1994), and in the southern Beaverhead Mountains (Zentner, 1989) indicating that they were active after rhyolite emplacement. These northeast-striking faults were previously interpreted to have formed as a result of flexure outboard of a down-warped ESRP volcanic basin (Zentner, 1989; Rodgers et al., 2002).

Some previous researchers hypothesized that the ESRP and the Basin and Range province to the north coevally extend, where ESRP extension is accommodated by dike injection and the Basin and Range by normal faulting (Rodgers et al., 1990). However, current Global Positioning Systems (GPS) observations indicate that the Basin and Range north of the ESRP is actively extending, while the ESRP moves as one coherent block (Payne et al., 2012). At a regional scale, GPS data suggest an active dextral component of slip along a northeast-trending shear zone between the Basin and Range and ESRP near the Centennial Mountains ~120 km northeast of the Arco Hills. This is referred to as the “Centennial shear zone,” and was projected into the Arco Hills by Payne et al. (2012). The presence of active dextral shear associated with the Centennial shear zone was corroborated by field observations of pressure solution pits on quartzite cobbles within a conglomerate exposed west of the Centennial Mountains, which documented a sub-horizontal (15°) greatest principal stress (σ_1) orientation of $256 \pm 22.0^\circ$ (Parker, 2016). This estimated σ_1 orientation is nearly parallel to the estimated trend of the Centennial shear zone.

We hypothesize that the northeast-striking faults in the Arco Hills could be the expression of the Centennial shear zone during an active or earlier phase of development of the ESRP. Rather than large-scale right-lateral strike-slip faults accommodating differential

extension between the northern Basin and Range and the ESRP (which have not been identified) the small-offset northeast-striking faults may accommodate dextral shear in a widely distributed zone.

1.3.3 Hydrogeologic Setting of the Eastern Snake River Plain

Water flow within the ESRP aquifer is primarily controlled by highly permeable rubble zones between the sides, tops, and bottoms of basalt layers (Welhan et al., 2002). The base of the ESRP aquifer does not correlate with elevation, depth below ground surface, age of host rocks, or occurrence of large packages of sedimentary interbeds (Morse, 2002; Mazurek, 2004). Helm-Clark et al. (2005) defined the base of the ESRP aquifer near the Advanced Test Reactor Complex of the INL based on a large temperature fluctuation that occurred below a thick sedimentary interbed ~350 m below the top of the ESRP aquifer. The base of the ESRP aquifer, as defined by an increase in groundwater temperature, correlated with a gradational contact between unaltered basalt and altered basalt that contains significant authigenic minerals within fractures, vesicles, and diktytaxitic cavities. Authigenic minerals were precipitated after basalt deposition under elevated water temperatures (Morse, 2002; Mazurek, 2004). Ackerman et al. (2006) defined the base of the ESRP aquifer on the basis of 13 deep boreholes drilled at the INL along with regional surface-based electrical resistivity surveys (Whitehead, 1992). Mann (1986) indicated that a significant portion of groundwater moves through the upper 60 to 250 m of basaltic rock and that the hydraulic conductivity of deeper (older) basalt is an order of magnitude smaller than the overlying younger basalts. The increase in authigenic minerals in deeper and older basalts reduced their effective permeability and hydraulic conductivity (Morse, 2002; Mazurek, 2004).

In the western INL, basalt and interbedded sedimentary rocks thin toward the northern margin of the ESRP (Doherty et al., 1979; Mazurek, 2004; Twining et al., 2017). Consequently, underlying Snake River-type rhyolites occur at shallower depths toward the margin of the ESRP near the northern Basin and Range, as evidenced by deep boreholes WO-2, INEL-1, and USGS-142 (Fig. 1.1, Table 1.1; Doherty et al., 1979; Mazurek, 2004; Twining et al., 2017). Mann (1986) indicated that the hydraulic conductivity of subsurface rhyolites in borehole INEL-1 is smaller than the oldest overlying basaltic units (0.01 ft/day compared to 0.03 ft/day, respectively), suggesting that the subsurface rhyolites are less permeable for groundwater flow.

Temperature logs and depth to water were measured during different drilling phases of borehole USGS-142 (Twining et al., 2017). During an earlier phase of drilling to a depth of 256 m, incrementally measured groundwater temperature produced a nearly uniform temperature profile. This suggests hydrologic connectivity (mixing) of deeper and shallower groundwater, and likely a single aquifer. These results thus indicate that the base of the ESRP aquifer was not encountered after the earliest phases of drilling. During this earlier phase of drilling, the depth to the top of the ESRP aquifer was 162 m (Twining et al., 2017).

After drilling was completed to a depth of 573 m, groundwater temperature was again incrementally measured to the base of the borehole; this time there was a distinct increase in temperature at a depth of 183 m (Twining et al., 2017). Furthermore, the top of the water level increased in elevation 9 to 24 m compared to the earlier phase of drilling; this rise in water level is similar to the amount of rise measured after drilling into rhyolite in borehole INEL-1 (Mann, 1986).

Table 1.1: Location and elevation of deep boreholes					
Borehole	Latitude (decimal degrees)	Longitude (decimal degrees)	Land surface (m)	Depth of rhyolite below land surface (m)	Elevation of rhyolite (m)
USGS-142	43.6437	-113.0193	1522	425	1097
INEL-1	43.6214	-112.943	1485	686	799
WO-2	43.5808	-112.876	1503	1146	357

Table 1.1: Table of location and elevation of boreholes USGS-142, INEL-1 and WO-2, depth of rhyolite below land surface, and elevation of rhyolite above mean sea level. Note that the contact between basalt and rhyolite occurs at shallower depths and higher elevations toward the Arco Hills (see figure. 1.1 for borehole locations). Latitude, longitude and elevation are relative to World Geodetic System 1984 (WGS-84).

Because basalt and interbedded sedimentary rocks thin toward the margin of the ESRP and northern Basin and Range, subsurface rhyolites occur at shallower depths toward the margin of the ESRP (Table 1.1). Beneath the western INL, the base of the ESRP aquifer may be confined by the contact between basalt and underlying subsurface Snake River-type rhyolites near the margin between the ESRP and the northern Basin and Range where borehole USGS-142 was drilled.

The geometry of the contact between basalt and underlying subsurface Snake River-type rhyolites between the margin of the ESRP and the northern Basin and Range is poorly constrained. Correlating surface and subsurface Snake River-type rhyolites to other rhyolites found within the subsurface the ESRP can thus 1) determine the geometry of the basalt and rhyolite contact and 2) constrain the base of the ESRP aquifer in the western INL near the margin of the ESRP.

CHAPTER 2: METHODS

2.1 Overview

This research interprets the temporal evolution of the ESRP near the Arco Hills by 1) constraining the degree of continuity and geometry of subsurface Snake River-type rhyolites, 2) establishing the relative structural elevations of subsurface units within the ESRP and correlative units exposed in mountains adjacent to the ESRP, and 3) determining the regional significance of northeast-striking faults near the margin of the ESRP.

2.2 Rhyolite Correlations

In spite of origination from different volcanic fields (e.g. Heise and Picabo) many interbedded Snake River-type rhyolites are composed of a similar, primarily anhydrous, mineralogical makeup; thus, a data suite must be compiled for a robust correlation to previously analyzed rhyolites. In this study, Snake River-type rhyolites were correlated by thin section analyses, U-Pb zircon age dating, Ar-Ar sanidine age dating, Lu-Hf isotope analyses, $\delta^{18}\text{O}$ stable isotope analyses, and major and trace element geochemistry.

2.2.1 Thin Section Analysis

Thin section billets were cut from: 1) the upper and lower vitrophyres, and in several intervals of the microcrystalline center zone of the rhyolite of USGS-142, 2) the lower vitrophyre and microcrystalline center zone of the rhyolite of Butte Quarry, 3) the lower vitrophyre of the West Pocatello rhyolite, and 4) the lower vitrophyre of the rhyolite of the east side of the Arco Hills. Billets were sent to Wagner Petrographic and were filled with clear epoxy.

Petrographic analyses were conducted to identify the primary mineral phases in each studied rhyolite for comparison to previously analyzed Snake River-type rhyolites,

and to determine if each rhyolite is a lava flow or an ignimbrite. Thin sections were analyzed for mineral assemblages, phenocryst abundance, and phenocryst and matrix textures using a Nikon Eclipse E400 polarizing petrographic microscope. Phenocrysts were identified by evaluating birefringence, interference figures, and distinctive cleavage planes. Individual phenocrysts were quantified as a percentage of total rock by counting 1000 points per thin section using a standard point counter; results were normalized after removing any natural vesicles that were found in thin section. Most thin sections were nearly aphanitic ($\leq 6\%$ total phenocryst content). Additional petrographic examinations of thin sections were conducted to identify minerals that were not counted while using the standard point counter.

2.2.2 U-Pb Zircon Geochronology and Lu-Hf Isotopic Analysis

U-Pb zircon ages, which are often interpreted to reflect the timing of initial subsurface magma crystallization in volcanic rocks, are useful tools for correlation of Snake River-type rhyolites (e.g. Drew et al., 2013). U-Pb zircon ages record the age of initial magma crystallization, because zircon has a high closure temperature ($>900^{\circ}\text{C}$); however, separate and chemically distinct magma chambers may have similar zircon ages, so U-Pb zircon ages must be paired with whole rock geochemistry, isotope analyses, and/or Ar-Ar age-dating techniques. Approximately 10-15 pounds of the microcrystalline center zones of both the rhyolites of USGS-142 and Butte Quarry were sampled and separated for zircons under protocol detailed in Appendix A (methods adapted from Gehrels and Pecha, 2014). Separated zircons were analyzed at the University of Arizona LaserChron Center using Laser Ablation Multi-Collector, Inductively Coupled Plasma Mass Spectrometry (LA-MC-ICP-MS). Individual zircon cores were targeted with a laser diameter of 20 μm , and ages

were interpreted from the weighted mean ratios of ^{206}Pb to ^{238}U . Each weighted mean average plot was created using Isoplot, a plug-in for Excel 2003, which uses the U-Pb ages including uncertainties of measured ratios of ^{206}Pb to ^{238}U in zircon grains to produce a reliable average U-Pb geochronology age (Ludwig, 2008). Random and systematic errors were quadratically combined to produce reliable uncertainties for ages.

Lu-Hf isotopic analyses were also conducted at the University of Arizona LaserChron center using LA-MC-ICP-MS; 40 μm diameter Lu-Hf laser spots were centered atop existing U-Pb zircon geochronology analysis locations. Data were analyzed and interpreted from the weighted mean ratios among both ^{176}Hf and ^{177}Hf , and ^{176}Lu and ^{176}Hf , where ^{176}Lu decays to ^{176}Hf , and ^{177}Hf is a stable isotope. These ratios and associated uncertainties were used to calculate the initial epsilon (ϵ) Hf value for each zircon phenocryst. This method compares the weighted mean ratio of radiogenic and stable isotopes of Hf to that of the bulk silicate earth, also known as the chondritic uniform reservoir (CHUR). In general, positive ϵHf are considered to have been recently derived from the mantle, or “juvenile,” whereas negative ϵHf values are considered derived from the mantle long ago, or “evolved.” Results also provide a useful fingerprinting tool for correlation. To compare these results with ϵNd data from previously-researched Snake River-type rhyolites, ϵHf was calculated from previously published ϵNd data using the “Terrestrial Array” equation of Vervoort et al. (1999): $\epsilon_{\text{Hf}} = 1.36\epsilon_{\text{Nd}} + 2.95$.

2.2.3 Ar-Ar Geochronology

Ar-Ar geochronology was also conducted on sanidine to measure the timing of eruption for each studied rhyolite. Relative to the U-Pb zircon geochronology, this isotopic system has a relatively low closure temperature ($\sim 300^\circ\text{C}$; Kelly, 2002); given the high

eruption temperatures of Snake River-type rhyolites (~900-1050° C; Branney et al., 2008), isotopic closure through ~300° C thus records the timing of rhyolite emplacement and cooling. In this system, parent isotopes of ^{40}K decay to daughter isotopes of ^{40}Ar . Given the different states of parent (solid) and daughter (gas), ^{39}Ar is produced in the laboratory from neutron irradiation of a stable ^{39}K in individual sanidine phenocrysts. Thus, ^{39}Ar is used as a proxy for ^{39}K (which has a known ratio to ^{40}K), which is a proxy for ^{40}K ; this allows for simultaneous measurements of Ar and K (by proxy) in a sample in the gas phase, which provides a precise age of cooling (Kelley, 2002). These ratios are compared to a standard with a known age (assuming ratios between isotopes of K and Ar are constant on Earth; Kelley, 2002). Therefore, the calculated age is a reliable constraint on the timing of emplacement of a rhyolite, which provides another correlation tool to previously analyzed Snake River-type rhyolites (e.g. Morgan and McIntosh, 2005; Anders et al., 2014).

The upper vitrophyre of the rhyolite of USGS-142 and the lower vitrophyre of the rhyolite of east side of the Arco Hills were sampled for Ar-Ar geochronology. Each sample was crushed as described in Appendix B. Crushed samples were sent to the Argon Geochronology for the Earth Sciences Laboratory at Lamont-Doherty Earth Observatory of Columbia University, where the analyses were conducted by laser fusion of single sanidine phenocrysts (methods described in Anders et al., 2014). Due to instrument problems, preliminary ages are reported in this thesis.

2.2.4 $\delta^{18}\text{O}$ Isotopic Analysis

The upper vitrophyre of the rhyolite of USGS-142, the lower vitrophyre of the rhyolite of Butte Quarry, and the lower vitrophyre of the rhyolite of the east side of the Arco Hills were sampled for $\delta^{18}\text{O}$ isotope analysis on individual plagioclase, quartz, and/or

pyroxene phenocrysts. $\delta^{18}\text{O}$ provides useful constraints on whether fluids interacting with subsurface magmas consisted of isotopically light meteoric water or isotopically heavy, likely mantle-derived fluids. These analyses also provide fingerprint tools for correlation among the studied and previously analyzed rhyolites, where lighter $\delta^{18}\text{O}$ values reflects younger emplacement of rhyolites in either the Heise or Picabo volcanic fields and heavier $\delta^{18}\text{O}$ (+6.6‰ to +8.3‰; Watts et al., 2011; Drew et al., 2013) reflects older emplacement of rhyolites in a volcanic field.

Each sample was crushed and separated for phenocrysts following protocols detailed in Appendix B. Separated phenocrysts and some crushed sand-sized ($425\mu\text{m} \leq X \leq 1.18\text{ mm}$) samples were sent to the Stable Isotope Laboratory at the University of Oregon. Oxygen isotope ratios of quartz, plagioclase, and/or pyroxene were measured using laser fluorination on one to two phenocrysts. $\delta^{18}\text{O}$ was measured from the mean ratio between ^{18}O and ^{16}O compared to standards with known values of VSMOW (Vienna Mean Standard Ocean Water; ratio of ^{18}O to ^{16}O has an absolute ratio of 0.020052) used during analysis.

Individual phenocrysts were analyzed with this method. However, ^{18}O does not fractionate evenly into different mineral phases during magma crystallization (Zheng, 1993). For example, quartz typically produces a higher $\delta^{18}\text{O}$ value compared to pyroxene in the same analyzed rhyolite (e.g. Watts et al., 2011; Drew et al., 2013) because ^{18}O fractionates into quartz more readily than pyroxene (Zheng, 1993). Therefore, values of $\delta^{18}\text{O}$ measured for individual phenocrysts were used to calculate the $\delta^{18}\text{O}$ value for a melt by using known isotope fractionation factors in a rhyolitic melt assuming a melt temperature of 900°C (Bindeman and Valley, 2003). This allowed for comparison among the studied rhyolites and previous analyses of Snake River-type rhyolites conducted by

Watts et al. (2011) and Drew et al. (2013) (Appendix C). An assumed melt temperature of 900°C was used because this value fell between the melt temperatures (850°C-950°C) used for calculated $\delta^{18}\text{O}$ melt values published by Watts et al. (2011). Drew et al. (2013) assumed a melt temperature of 850°C; however, reducing or raising the assumed melt temperature by 50° C typically changed the calculated $\delta^{18}\text{O}$ melt value by $\leq 0.1\%$.

2.2.5 X-ray Fluorescence Analysis

Geochemical analyses were conducted using X-ray fluorescence (XRF), which provides another useful tool for correlation among Snake River-type rhyolites. Although major element compositions are sensitive to alteration, and trace element compositions are sensitive to phenocryst fractionation (e.g. Watts et al., 2011), this method provides a useful comparison between previously analyzed Snake River-type rhyolites with similar whole rock geochemistry.

The microcrystalline center zones of the rhyolites of USGS-142 and Butte Quarry were analyzed using XRF. Each sample and the sample preparation area was thoroughly cleaned with isopropanol alcohol to insure there was no potential for contamination. Each sample was individually hand crushed to ~1 to 2 cm pieces, which were powdered in a clean shatterbox for approximately two minutes. Powdered samples were sent to Brigham Young University, and were analyzed via an XRF spectrometer to measure their major and trace element compositions.

2.3 Structural Analysis of Small-Displacement Faults

A kinematic analysis of northeast-striking faults found in the Arco Hills was done to evaluate the regional significance of these faults, namely whether they are regional features accommodating 1) lateral displacement between the ESRP and the Basin and Range (e.g.

Payne et al., 2012); 2) along strike decrease in slip of Basin and Range normal faults toward the ESRP (Bruhn et al., 1992); 3) ring fracture faults associated with caldera subsidence (Morgan et al., 1984); or 4) flexure as a result of subsidence of the ESRP (Zentner, 1989; Rodgers et al., 2002). The kinematic analysis was conducted to establish the regional geometries and relative displacements of faults. Data were collected in the Arco Hills by recording the strikes and dips of fault planes, the trends and plunges of slickenlines on each fault plane, and determining the sense of slip of each fault (e.g. normal versus reverse). Recording this data for several faults in a given field area allowed for the determination of the regional strain. For example, if the majority of measured faults display normal displacement (e.g. down-dip slickenlines), this suggests that the recorded faults accommodated crustal extension.

2.3.1 Data Collection in the Field

From preliminary observations in the southern Beaverhead Mountains, the preservation of fault surfaces and striations occurs predominantly along offset chert-bearing layers; this is likely related to a higher preservation potential of silicified fault surfaces. The primary stratigraphic unit targeted in this research was the Mississippian Scott Peak Formation, a dark to medium gray, fossiliferous, cliff-forming, and locally chert-bearing limestone (Skipp et al., 2009). Given that the Mississippian Scott Peak Formation contains intervals of chert, and crops out in a nearly north-south transect in the southern Arco Hills (Skipp et al., 2009), this formation was investigated for fault kinematic analysis. Previously mapped faults found on the Geologic Map of the Arco 30 X 60 Minute Quadrangle, South-Central Idaho by Skipp et al. (2009) were targeted, and nearly every outcrop of the Mississippian Scott Peak Formation was investigated in the study area.

A standard Brunton compass was used to measure the orientation of each fault surface. The acute angle between the strike of each fault plane and slickenlines on the fault surface was measured to determine the orientation of slip direction (recorded as rake; Fig. 2.1). Where possible, the relative displacement across faults was determined by recognizing offset marker beds along fault planes (Fig. 2.2). All faults found in the Arco Hills were measured, regardless of orientation and slip direction, to create a quantitative and unbiased data set that best represented the regional brittle deformation in the Arco Hills.



Figure 2.1: A fault surface exposed in the Arco Hills, which shows the method for fault measurement. The horizontal line is the strike of the fault surface, and the nearly vertical lines are striations; the acute angle between these lines was recorded to determine the orientation of slip (rake).

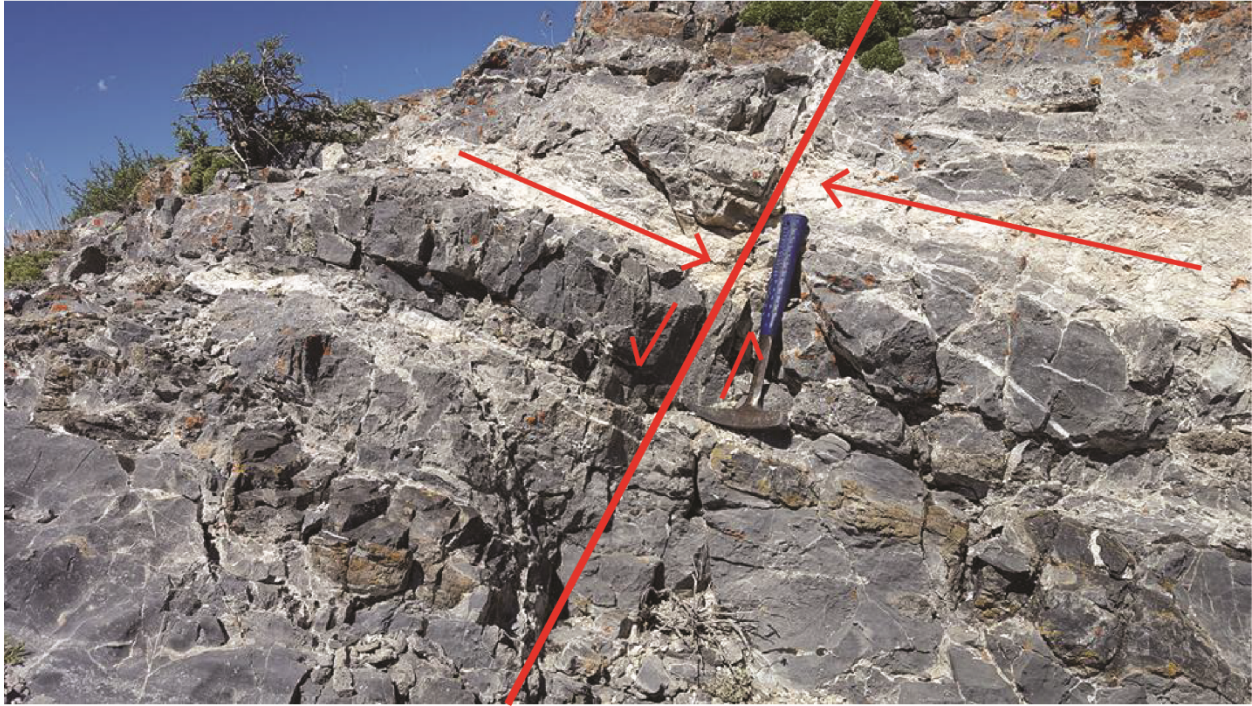


Figure 2.2: An example of an offset marker bed that demonstrates normal displacement. Arrows indicate offset beds and relative direction of offset.

2.3.2 Analysis of Fault Data

The fault-slip data were analyzed using the program FaultKin, which uses data collected from small-displacement faults to interpret the regional kinematics of faulting in an area (Marrett and Allmendinger, 1990; Allmendinger et al., 2012). The shortening (P) and extension (T) axes (kinematic axes) occur in a plane defined by slickenline lineation and pole to fault plane; the kinematic axes occur 45° from either the slickenline lineation or pole to fault plane depending on the sense of slip (Fig. 2.3). Collectively, these kinematic axes are used in FaultKin to produce fault plane solutions, where the mean shortening axis occurs in the center of the maximum shortening direction (white quadrant; Fig. 2.3) and the extension axis occurs in the center of the minimum shortening direction (gray quadrant; Fig. 2.3). Fault plane solutions are useful to illustrate the strain that produced

regional faulting. The mean direction of the shortening and extension axes are used to infer the principal directions of strain in the Arco Hills. These data were used to evaluate whether these faults record pure dip-slip or could have accommodated oblique dextral extension associated with the hypothesized Centennial shear zone (Payne et al., 2012).

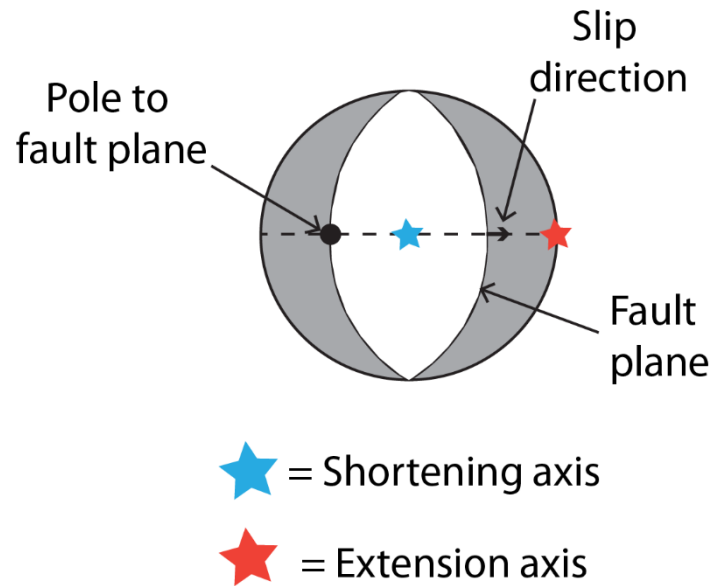


Figure 2.3: Schematic representation of a synthetic focal mechanism/ fault plane solution. Shortening and extension axes occur 45° from the pole to a fault plane and the slickenline, depending on the direction of slip. The shortening axis occurs in the center of the maximum shortening direction quadrant (white), and the extension axis occurs in the center of the minimum shortening direction quadrant (gray). This example displays a north-striking normal fault that accommodated pure dip-slip displacement.

In addition, poles to fault planes, shortening axes, and extension axes were plotted on equal-area, lower hemisphere stereographic projections. These were classified by ratios among eigenvalues ($\lambda_1, \lambda_2, \lambda_3$) calculated in Stereonet[®] 9 (Allmendinger et al., 2012); eigenvalues correspond to the magnitude of principal strain axes, where λ_1 corresponds to the point where the majority of data points fall. Calculating eigenvalues allows for a quantitative analysis of fit, clustering and girdling (Fig. 2.4, Woodcock, 1977), referred to as

fabric shape. Figure 2.4 provides illustrations of fabric shape with regards to clustering and girdling. Perfect clustering is represented as $\ln(\lambda_1/\lambda_2)/\ln(\lambda_2/\lambda_3)$ (referred to as “K”) approaches infinity; perfect girdling is represented as K approaches 0; and K=1 signifies no preference. As fit increases and scatter decreases, $\ln(\lambda_1/\lambda_3)$ increases. Clustered fabric shape suggests that data points plot in a nearly uniform point, whereas girdled fabric shape suggests that a great circle (plane) encompasses the data points.

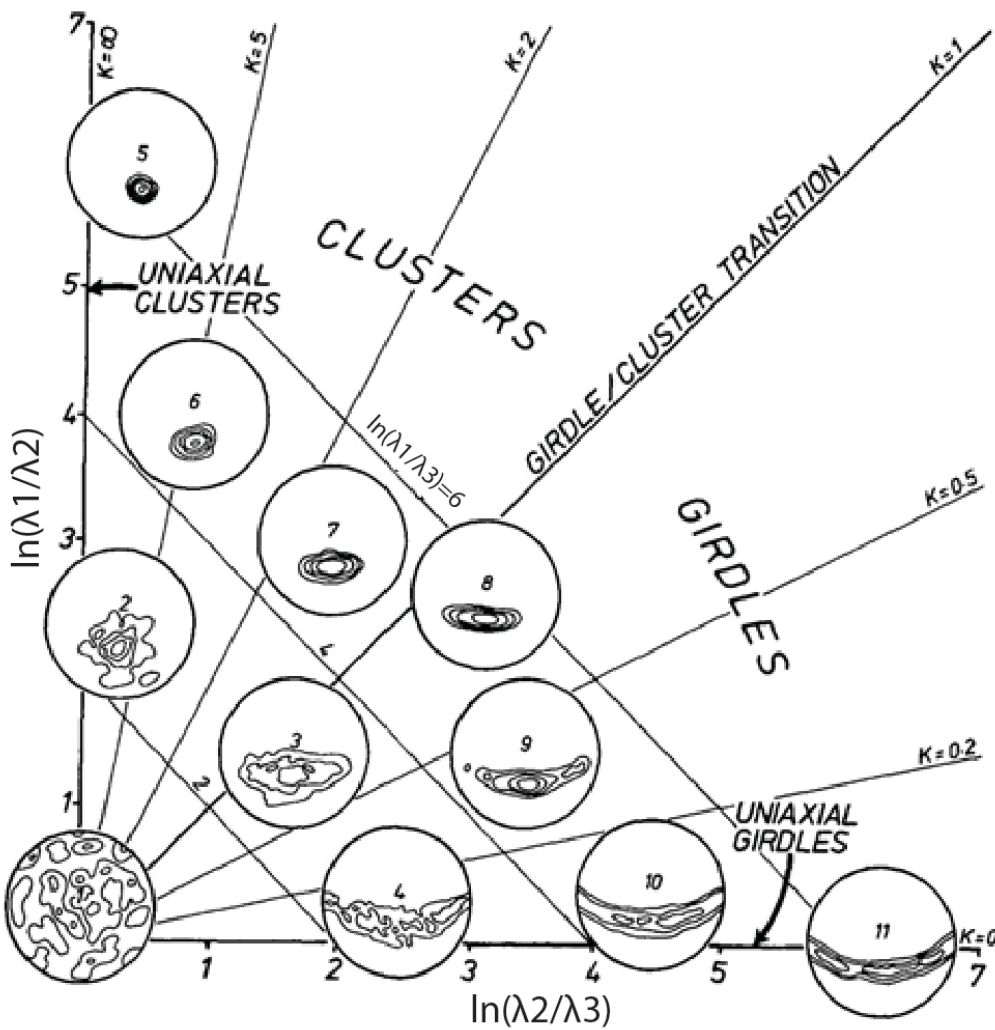


Figure 2.4: Two-axis logarithmic plot of ratios of normalized eigenvalues (λ_1 , λ_2 , and λ_3) with examples of fabric shapes with different K values. Modified from Woodcock (1977).

An assumption with kinematic analysis is that the collected fault data reflect a uniform stress field and there has been no deformation after faulting ceased. To determine if brittle deformation in the southern Arco Hills varies spatially with regards to the ESRP, fault data points were divided relative to the 20° Mesozoic fold-plunge contour of McQuarrie and Rodgers (1998) to test if the northeast-striking faults of the Arco Hills were also affected by flexure. Divided fault data are referred to as “proximal” and “distal” (relative to the ESRP) fault domains (Fig. 2.5).

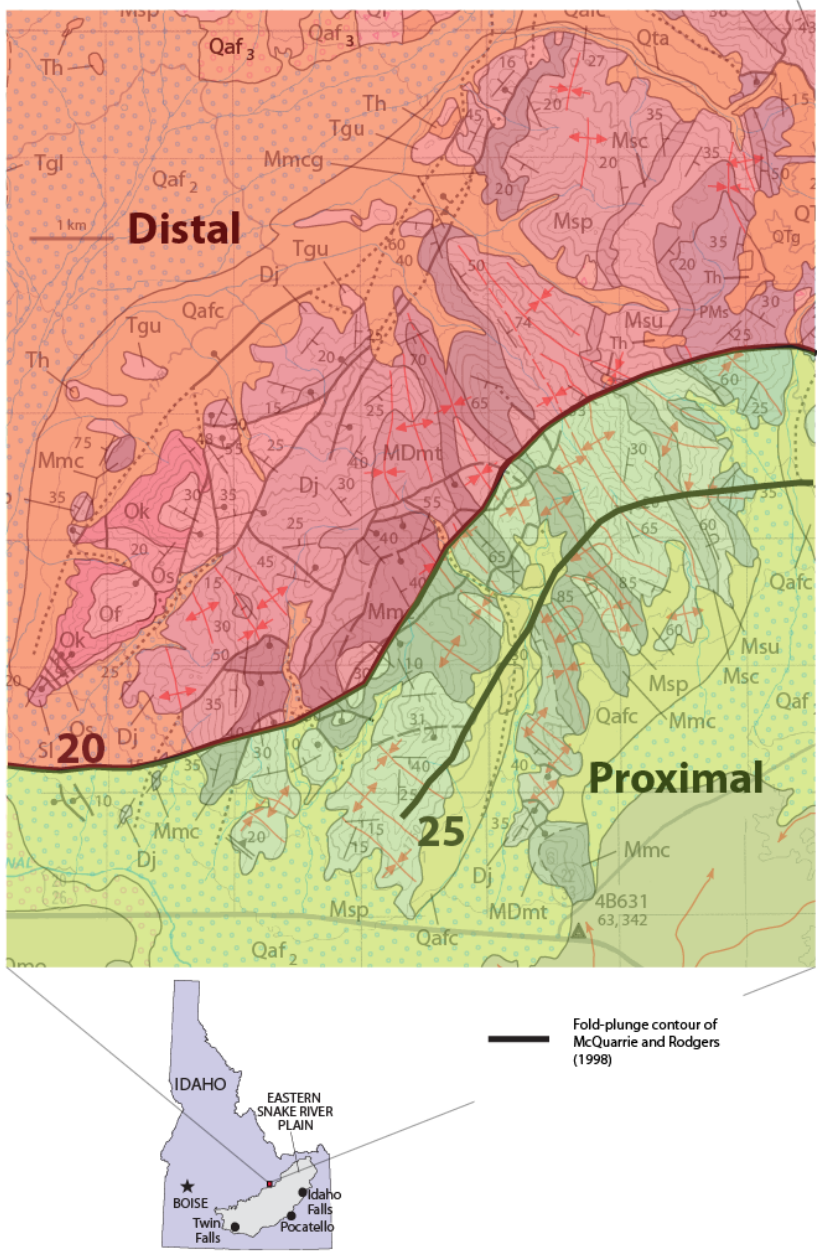


Figure 2.5: Division of fault data relative to the 20° fold-plunge contour of McQuarrie and Rodgers (1998). The red section highlights the distal fault domain, and the green section highlights the proximal fault domain (relative to the ESRP). Geologic map modified from Skipp et al. (2009).

Given that the northeast-striking faults that surround the ESRP dip both toward and away from the ESRP (Zentner, 1989), if these faults were rotated like the Mesozoic fold-hinges (McQuarrie and Rogers, 1998), then faults that originally dipped toward the ESRP (southeast in the Arco Hills) should have increased in average dip magnitude toward the ESRP (Fig. 2.6). Conversely, faults that originally dipped away from the ESRP (northwest in the Arco Hills) should have decreased in average dip magnitude toward the ESRP (Fig. 2.6). Similarly, calculated shortening axes would have decreased in magnitude of plunge toward the ESRP. Thus, a mean vector analysis was conducted for poles to fault planes and shortening axes for both the proximal and distal fault domains; analyses for poles to fault planes were separated into southeast-dipping faults and northwest-dipping faults for each domain.

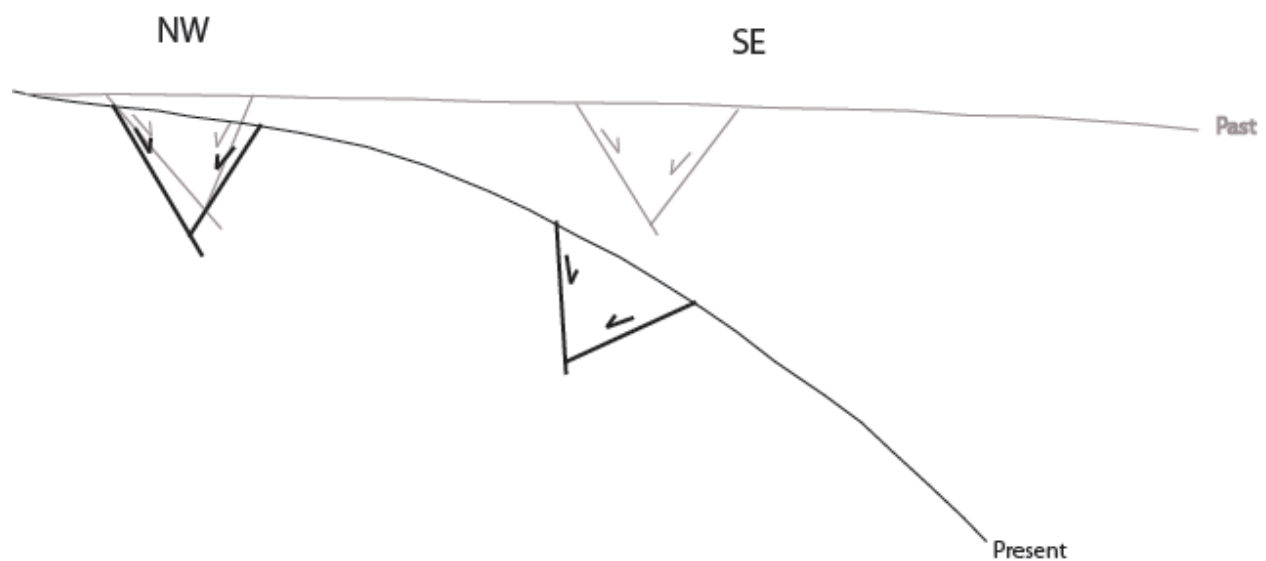


Figure 2.6: Schematic representation of rotated fault planes. Gray lines represent faults prior to being rotated (black lines).

2.4 Cross Section from the Arco Hills through Deep Boreholes

A cross section (location shown in figure 2.7) was created through the Arco Hills using Midland Valley's Move software. The cross section interprets the subsurface architecture of Snake River-type rhyolites in the ESRP relative to the previously drilled deep boreholes USGS-142, INEL-1, and WO-2. This was accomplished by correlating the rhyolites of USGS-142, Butte Quarry and east side of the Arco Hills to deep boreholes within the west-central INL (see Results and Discussion). Given that the exposure of the rhyolite of Butte Quarry is not aligned with boreholes USGS-142, INEL-1, and WO-2, the base of the rhyolite of Butte Quarry was contoured around the Arco Hills to a cross section in line with deep boreholes USGS-142, INEL-1, and WO-2, relative to the fold-plunge contours of McQuarrie and Rodgers (1998) and assuring that the projection of the rhyolite of Butte Quarry made geologic sense with the presented age dates.

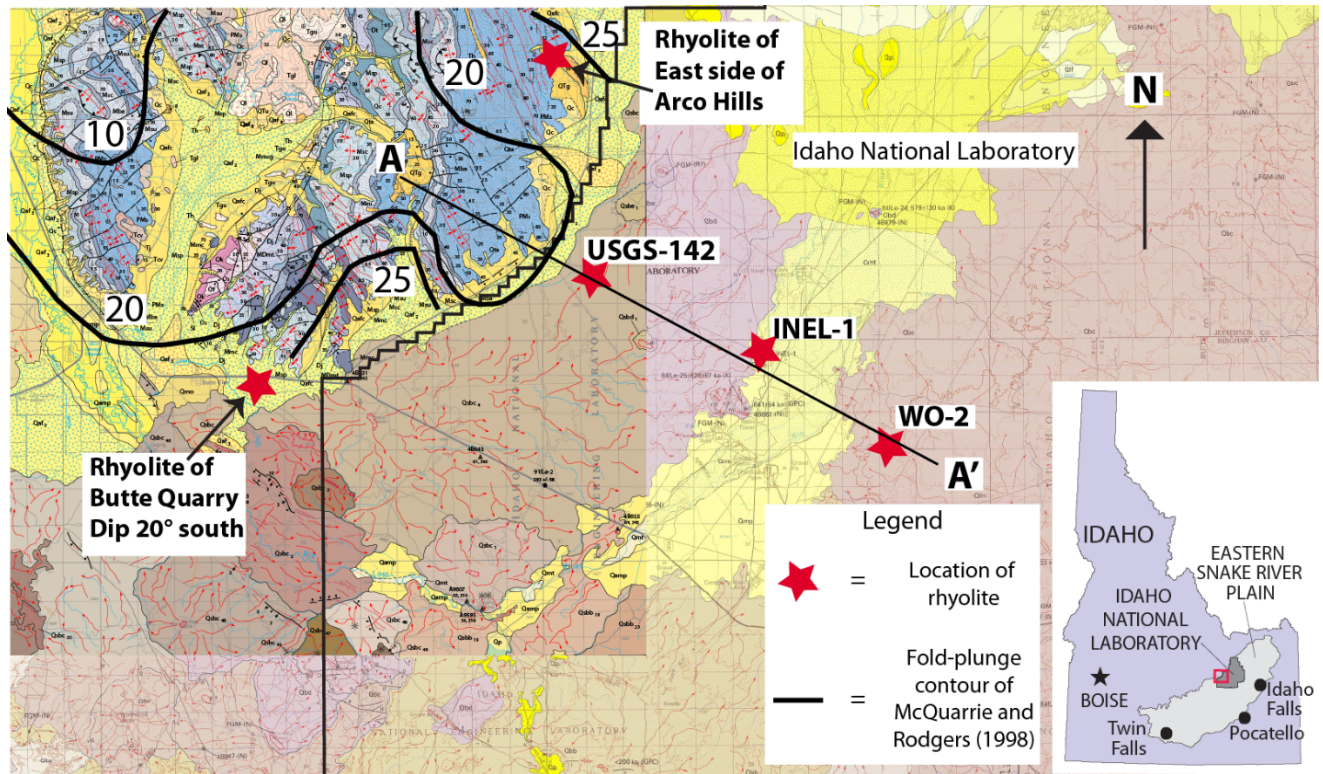


Figure 2.7: Location of section trace A-A', boreholes USGS-142, INEL-1, and WO-2, and surface exposures of the rhyolites of Butte Quarry and east side of the Arco Hills. Map legend indicates the location of the INL, and the geographic limit of this figure (red box). Two base geologic maps are modified from Skipp et al. (2009) and Kuntz et al. (1994). Map legends for each geologic unit are provided in the original publications.

CHAPTER 3: RESULTS

3.1 Results of Rhyolite Correlation

Results of thin section analysis, XRF analysis, U-Pb zircon geochronology, Lu-Hf isotope analysis, and $\delta^{18}\text{O}$ isotope analysis for the rhyolites of USGS-142 and Butte Quarry are presented below. Preliminary results for Ar-Ar age dating are presented for the rhyolites of USGS-142 and east side of the Arco Hills. Results for thin section analysis and $\delta^{18}\text{O}$ isotope analysis are also presented for the rhyolite exposed on the east side of the Arco Hills. Additional thin sections were analyzed for the West Pocatello rhyolite to determine if its mineralogy matches any of the studied rhyolites. These analyses were used to correlate each studied rhyolites to other rhyolites found in deep boreholes within the INL and surficial exposures found near the margins of the ESRP.

3.1.1 Macroscopic and Microscopic Observations

Field observations and thin section observations for the rhyolites of Butte Quarry and the east side of the Arco Hills are described below. Thin section observations for the rhyolite of USGS-142 and the West Pocatello rhyolite are also described below. Twining et al. (2017) provided a detailed description of the rhyolite of USGS-142 in their Appendix C. Appendix E illustrates a simplified stratigraphic column of borehole USGS-142, and depths where this rhyolite was sampled for thin section analysis, XRF analysis, and U-Pb zircon ages.

Thin sections from the rhyolite vitrophyres were analyzed to determine their petrogenesis, namely whether or not they contained textures resulting from emplacement by a pyroclastic density current, versus a lava flow. Thin sections from both the microcrystalline center zones and vitrophyres were analyzed to determine the

mineralogical makeup and percentage of each population of phenocrysts. Table 3.1 displays the results from point-counting selected thin sections. Figures 3.1, 3.2, and 3.3 show selected photomicrographs for the matrix and phenocrysts textures described below.

3.1.1.1 Rhyolite of USGS-142

The upper ~1 m of the rhyolite of USGS-142 is a glassy vitrophyre. The upper ½ m of this deposit is densely welded with a nearly uniform amorphous glassy matrix, while thin sections from the lower ½ m of the upper vitrophyre display well-defined cusped glass shards. Eutaxitic texture, where the cusped glass shards are flattened, is found throughout the ½ m of the upper vitrophyre. Spherulites are commonly observed and are nearly spherical, and range in size from 0.5 to 1 mm.

Below the upper vitrophyre and nearly to the lower vitrophyre, the microcrystalline center zone displays a densely welded, devitrified, microcrystalline core. Natural vesicles are commonly lined with tridymite. Several phenocrysts, notably plagioclase, are highly fractured and “weathered”.

The devitrified core rapidly grades downward into a moderately to densely welded vitrophyre, where cusped glass shards are still present, but have been clearly flattened and plastically deformed. Significant spherulitic devitrification is also apparent, where spherulites are commonly oblate and range from 1 to 1.5 mm in size.

The lower vitrophyre, found at a depth of 568 m, appears to grade downward to the base of the borehole (575 meters) into a poorly sorted unwelded tephra. This lower portion of the rhyolite of USGS-142 displays well-defined and undeformed cusped glass shards, and contains sparse broken crystal fragments that are mostly composed of plagioclase, pyroxene, and opaque phenocrysts.

3.1.1.2 Rhyolite of Butte Quarry

The rhyolite of Butte Quarry crops out just south of the Arco Hills (Fig. 1.1), where a lower vitrophyre and an overlying microcrystalline core are exposed. Outcrops of both the lower vitrophyre and microcrystalline core are crystal poor, composed of ~5% phenocrysts of dominantly white euhedral-subhedral plagioclase phenocrysts, with lesser amounts of pyroxene and quartz. This rhyolite dips 20° south as defined by distinct foliation planes; it displays nearly east-west flow indicators from stretched lithophysae (vesicle) cavities. The outcrop of the rhyolite of Butte Quarry exposes approximately 50 meters vertical thickness of rhyolite; the upper vitrophyre is not exposed.

The lower vitrophyre of the rhyolite of Butte Quarry is the lowest exposed portion of this deposit. Thin sections created from the lower vitrophyre contain flattened cusped glass shards that form a eutaxitic fabric. Down dip from the lower vitrophyre, the rhyolite of Butte Quarry becomes a densely welded devitrified tuff. Natural vesicles are clearly aligned with foliation, and are commonly lined with tridymite. Rotated plagioclase phenocrysts are often observed, where the matrix warps around the phenocrysts.

3.1.1.3 Rhyolite of the east side of the Arco Hills

The rhyolite of the east side of the Arco Hills crops out southwest of Howe, Idaho, where a lower vitrophyre and an upper microcrystalline core are exposed and overlie a stratified, welded ashfall deposit. The sampled lower vitrophyre is composed of ~5% phenocrysts of dominantly plagioclase, with lesser amount of pyroxene and opaque phenocrysts. The overlying microcrystalline core contains ~5-10% phenocrysts of dominantly plagioclase, with lesser amount of pyroxene, quartz, and opaque phenocrysts. However, the microcrystalline center zone of this rhyolite was not sampled for thin section

analysis. The microcrystalline center zone is dark gray, but dark red where lithophysae cavities occur. The outcrop is approximately 3 meters thick where exposed.

Thin sections for the lower vitrophyre of the rhyolite of the east side of the Arco Hills were analyzed in this study. Two samples were collected from this lower vitrophyre: one that was poorly consolidated, and one that was more “intact.” The poorly consolidated sample displays intense spherulitic devitrification, and is nearly completely aphanitic, so this was not point-counted (16KSO2A&B; Table 3.1). The intact sample of this deposit contains slightly flattened cusped glass shards, which define a eutaxitic fabric.

3.1.1.4 West Pocatello rhyolite

Thin sections from the lower vitrophyre of the West Pocatello rhyolite was analyzed for this study; two thin sections were created from one sample of the vitrophyre. Both showed signs of extreme welding to the point where a eutaxitic fabric (if present to begin with), was not recognized in thin section. There was not sufficient evidence to categorize this rhyolite as either an ignimbrite or lava flow (see Chapter 4). Therefore, these thin sections were not point-counted to determine the mineralogical mode present.

Sample	Type		Phenocryst content	Point Count	Plag	San	Qtz	Cpx undiff	Opx	Mt	Ilm	Zircon	Apatite
USGS-142-1394'	WT	V	5.2%	1000	4.0%	Minor	Minor	0.9%	Minor	0.3%	-	Minor	Minor
USGS-142-1475'	WT	LCZ	4.9%	1000	3.8%	0.1%	-	0.5%	Minor	0.5%	-	Minor	Minor
USGS-142-1862'	WT	V	1.1%	1000	0.7%	Minor	-	0.3%	Minor	0.1%	-	Minor	Minor
Butte Quarry -1	WT	V	1.9%	1000	1.5%	Minor	0.1%	0.1%	Minor	0.2%	Trace (?)	Minor	Minor
Butte Quarry -2	WT	LCZ	4.0%	1000	3.1%	Minor	0.1%	0.6%	Minor	0.2%	-	Minor	Minor
16KS02A	WT	V	1.7%	1000	1.3%	Minor (?)	Minor	0.1%	-	0.3%	-	Minor	Minor
16KS02B	WT	V	0.9%	1000	0.7%	-	Minor	0.1%	-	0.1%	-	Minor	Minor

Table 3.1: Volume percentages of phenocrysts normalized after removing natural vesicles for the rhyolite of USGS-142, the rhyolite of Butte Quarry, and the rhyolite of the east side of the Arco Hills. WT = welded tuff; V = vitrophyre; LCZ = lithoidal (microcrystalline) center zone.

3.1.2 Phenocryst Textures

Glomerocrysts, where phenocrysts are clustered into aggregates, are the most obvious phenocryst texture in the studied rhyolites, and are found in all samples. These crystal aggregates can be subdivided into two distinct populations from the presence or absence of pyroxene.

Type 1 glomerocrysts are composed of subhedral to euhedral plagioclase (Type 1 plagioclase, see below), anhedral sieved plagioclase (Type 2 plagioclase, see below), clinopyroxene, orthopyroxene, equant opaques, quartz, sanidine, zircon, and/or apatite phenocrysts. Type 1 glomerocrysts range in size from 1 to 1.5 mm, and are dominantly composed of plagioclase phenocrysts.

Type 2 glomerocrysts are composed of subhedral to euhedral plagioclase (Type 1 plagioclase), quartz, sanidine, zircon, and apatite phenocrysts. Type 2 glomerocrysts are dominated by plagioclase, but lack pyroxene. Type 2 glomerocrysts range in size from 1 to

1.5 mm, and were only found in the rhyolite of Butte Quarry and the West Pocatello rhyolite.

Plagioclase - type 1

Type 1 plagioclase phenocrysts are subhedral to euhedral with an average phenocryst size of 0.5 to 2.5 mm. Minor dissolution is present at the edges of phenocrysts, especially in the microcrystalline center zones of rhyolites. Type 1 plagioclase phenocrysts display well-defined polysynthetic twinning. Weak oscillatory zonation is less common. Type 1 plagioclase phenocrysts occur as isolated grains and in type 1 and 2 glomerocrysts. Inclusions of apatite and equant opaque phenocrysts are common. In the rhyolite of Butte Quarry, type 1 plagioclase phenocrysts often enclose clinopyroxene phenocrysts.

Plagioclase - type 2

Type 2 plagioclase phenocrysts are anhedral to subhedral with an average phenocryst size of 0.5 to 2.5 mm. Type 2 plagioclase phenocrysts are heavily sieved from the core to the edges, and display moderate to weak oscillatory zonation. Weak polysynthetic twinning is less common to absent. Type 2 plagioclase phenocrysts occur as isolated phenocrysts and within type 1 glomerocrysts. Inclusions of apatite phenocrysts rarely occur within type 2 plagioclase phenocrysts.

Clinopyroxene

Clinopyroxene phenocrysts of two distinct compositions are present in the rhyolite of Butte Quarry. Pigeonite and ferroaugite were identified, and differentiated by measuring their 2V angle. Pigeonite phenocrysts are euhedral, equant, and range in size from 0.2 to 0.5 mm, and display low (0 to 20°) positive 2V angles. Ferroaugite phenocrysts are subhedral, slightly elongated, range in size from 0.2 to 0.5 mm, and have moderate (50 to 60°) positive

2V angles. The rhyolite of USGS-142 and the rhyolite of the east side of the Arco Hills only contain ferroaugite phenocrysts. Clinopyroxene phenocrysts occur as isolated phenocrysts and within type 1 glomerocrysts. Inclusions of apatite are common in clinopyroxene; zircon is less common.

Orthopyroxene

Orthopyroxene phenocrysts are subhedral, slightly elongated, and range in size from 0.2 to 0.3 mm. These phenocrysts were differentiated from clinopyroxene by measuring a low (0 to 20°) negative 2V angle; the low 2V angle suggests that these phenocrysts are ferrosilite. In addition, orthopyroxene is moderately pleochroic, and extinction is parallel to cleavage. Orthopyroxene occurs as isolated phenocrysts and within type 1 glomerocrysts. Orthopyroxene is confidently identified in the rhyolites of USGS-142 and Butte Quarry, but not in the West Pocatello rhyolite nor the rhyolite of the east side of the Arco Hills.

Quartz

Quartz phenocrysts are euhedral to subhedral, rounded, and range in size from 0.3 to 0.5 mm. Quartz phenocrysts were found as isolated phenocrysts, and within type 1 glomerocrysts. Fluid inclusions are commonly observed within quartz phenocrysts.

Sanidine

Sanidine phenocrysts are euhedral to subhedral, tabular, and range in size from 0.1 to 0.2 mm. Sanidine phenocrysts were found as isolated phenocrysts, although they *may* occur within both type 1 and 2 glomerocrysts; however, an interference figure could not be measured for individual feldspar phenocrysts in glomerocrysts.

Opaque phenocrysts

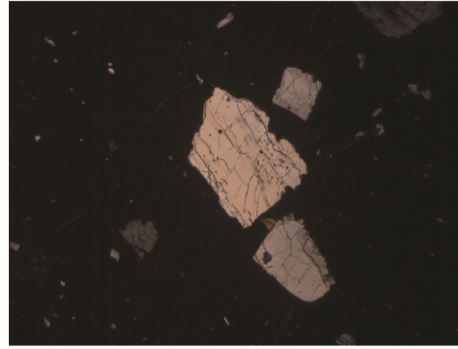
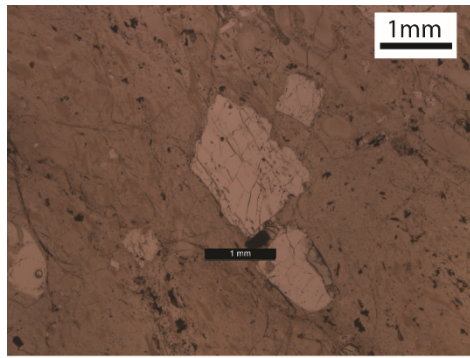
Opaque phenocrysts are euhedral to subhedral, equant to slightly elongated, and range in size from 0.1 to 0.4 mm. These phenocrysts are found as isolated phenocrysts, within type 1 glomerocrysts, and as inclusions within type 1 plagioclase and clinopyroxene. Apatite is often closely associated with the opaque phenocrysts. All studied rhyolites contain dominantly equant opaque phenocrysts, and rare to absent amounts of elongated opaque phenocrysts, suggesting magnetite is volumetrically more abundant in all studied rhyolites.

Zircon

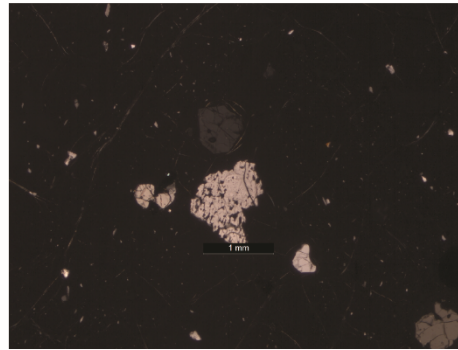
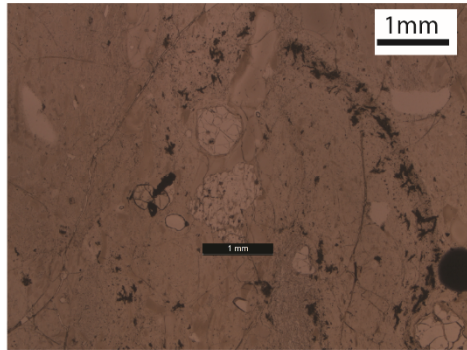
Zircon phenocrysts are subhedral to euhedral, prismatic, and are $\leq 100\mu\text{m}$ in size. Zircon phenocrysts are commonly found as inclusions within clinopyroxene and orthopyroxene, and as isolated phenocrysts within type 1 and 2 glomerocrysts often in close proximity to equant opaque and pyroxene phenocrysts.

Apatite

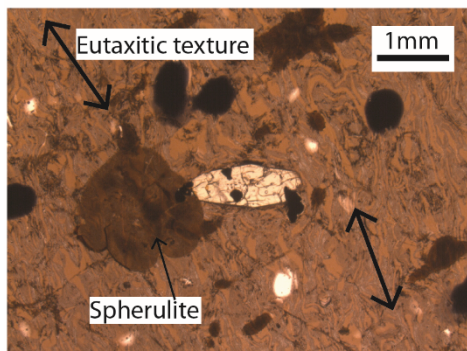
Apatite phenocrysts are euhedral, elongated to needle-like, and are $\leq 100\ \mu\text{m}$ in size. Apatite phenocrysts are found as isolated phenocrysts closely associated with opaque and pyroxene phenocrysts, and as inclusions within type 1 plagioclase and pyroxene phenocrysts.



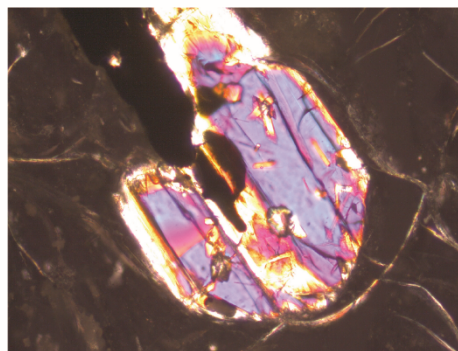
Type 1 plagioclase phenocrysts



Type 2 plagioclase phenocryst with a quartz phenocryst above.

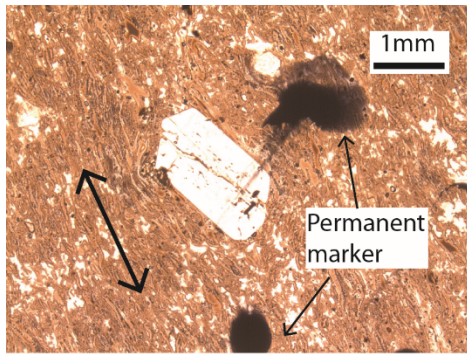


Ferroaugite phenocryst, spherulite, and eutaxitic texture indicated by double-ended arrows

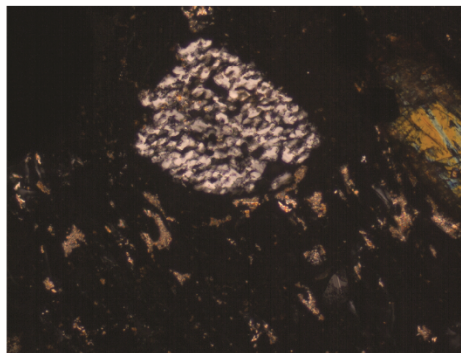
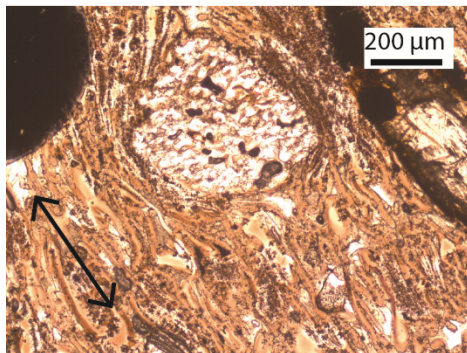


Orthopyroxene phenocryst (likely ferrosillite) with opaque (magnetite?) phenocrysts.

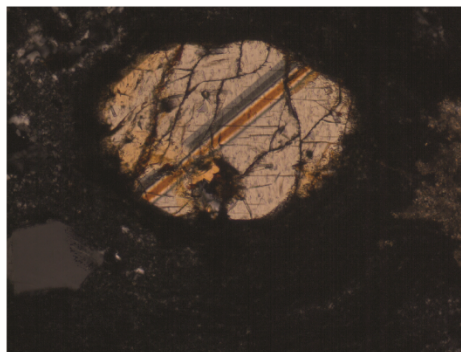
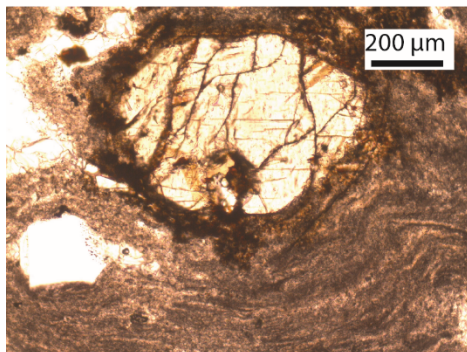
Figure 3.1: Selected photomicrographs of phenocrysts and textures found in the rhyolite of USGS-142, with plane-polarized photos on the left and cross-polarized photos on the right.



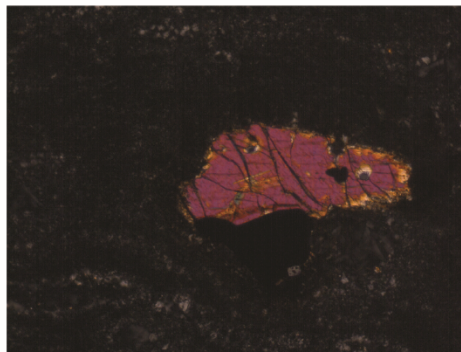
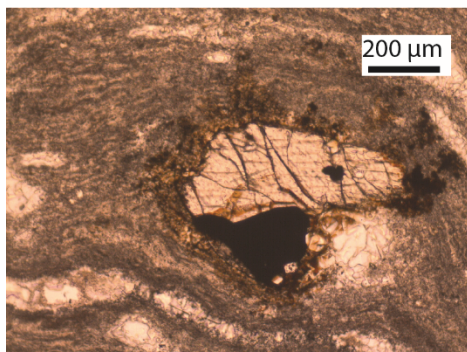
Type 1 plagioclase phenocryst. Double-ended arrow indicates eutaxitic texture.



Type 2 plagioclase phenocryst with notable sieved texture. Double-ended arrow indicates eutaxitic texture.

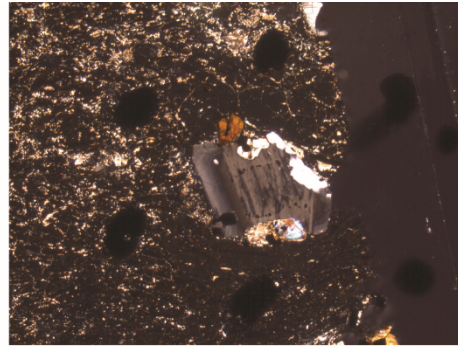
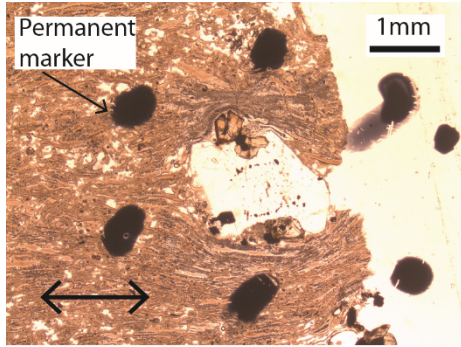


Pigeonite phenocryst.

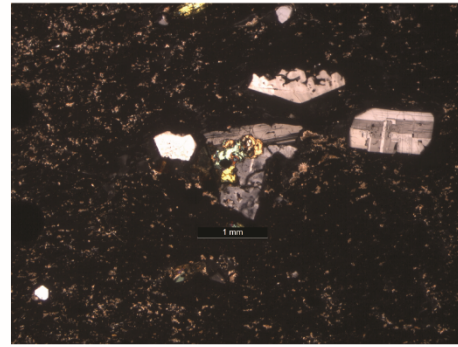
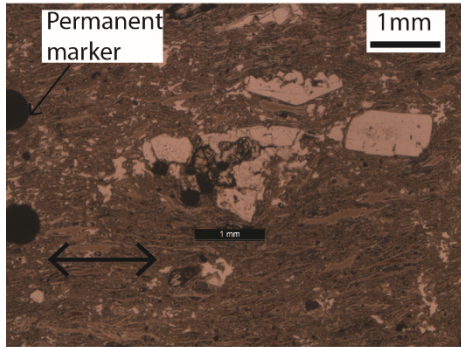


Ferroaugite phenocryst with an opaque (magnetite?) phenocryst.

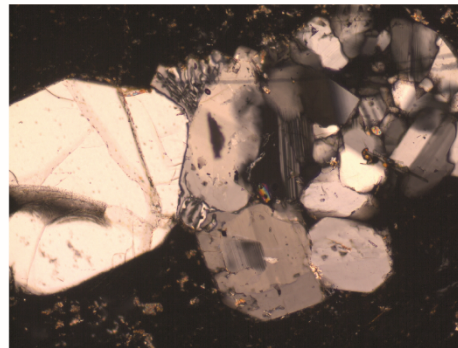
Figure 3.2: Selected photomicrographs of phenocrysts and textures found in the rhyolite of Butte Quarry with plane-polarized photos on the left and cross-polarized photos on the right.



Type 1 glomerocryst with type 1 plagioclase, orthopyroxene (top), and clinopyroxene (bottom) phenocrysts. Double-ended arrow indicates eutaxitic texture

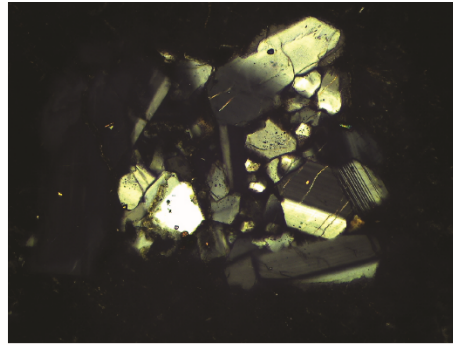
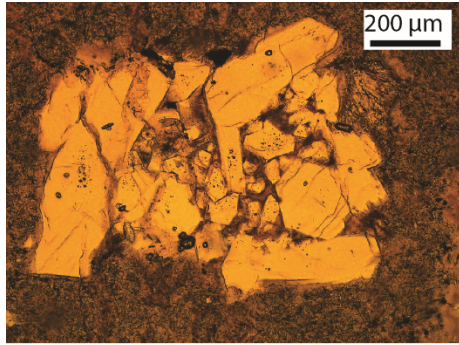


Type 1 glomerocryst with type 1 plagioclase, clinopyroxene, and magnetite phenocrysts. Double-ended arrow indicates eutaxitic texture.

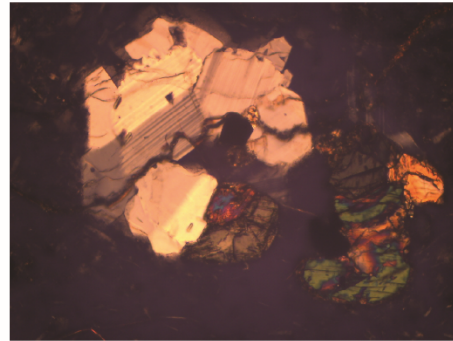
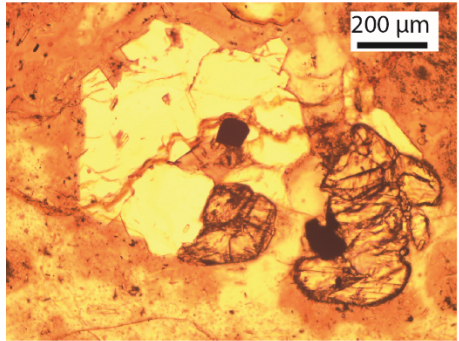


Type 2 glomerocryst with type 1 plagioclase and zircon phenocrysts

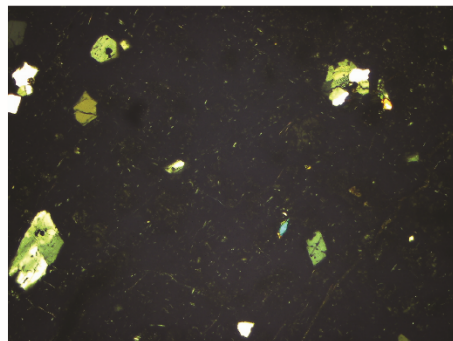
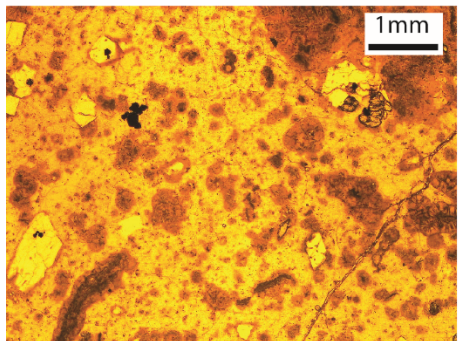
Figure 3.2 continued



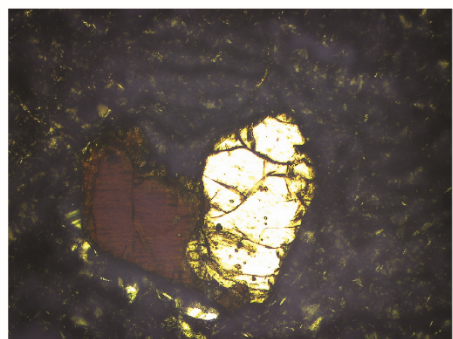
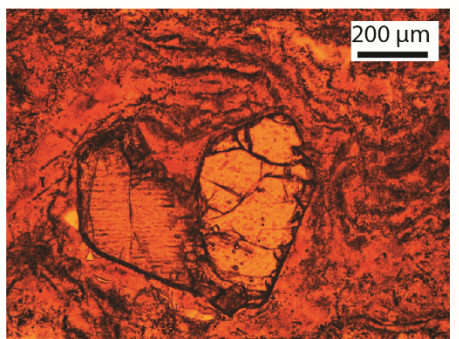
Type 1 glomerocryst composed of dominantly type 1 plagioclase and some zircons



Type 2 glomerocryst composed of plagioclase, pigeonite, and opaque phenocrysts



Matrix with no eutaxitic texture. Small white specs in matrix are likely tridymite.



Pigeonite phenocrysts

Figure 3.3: Selected photomicrographs of phenocrysts and textures found in the West Pocatello rhyolite. Photos on the left are in plane-polarized light, and right photos are cross-polarized.

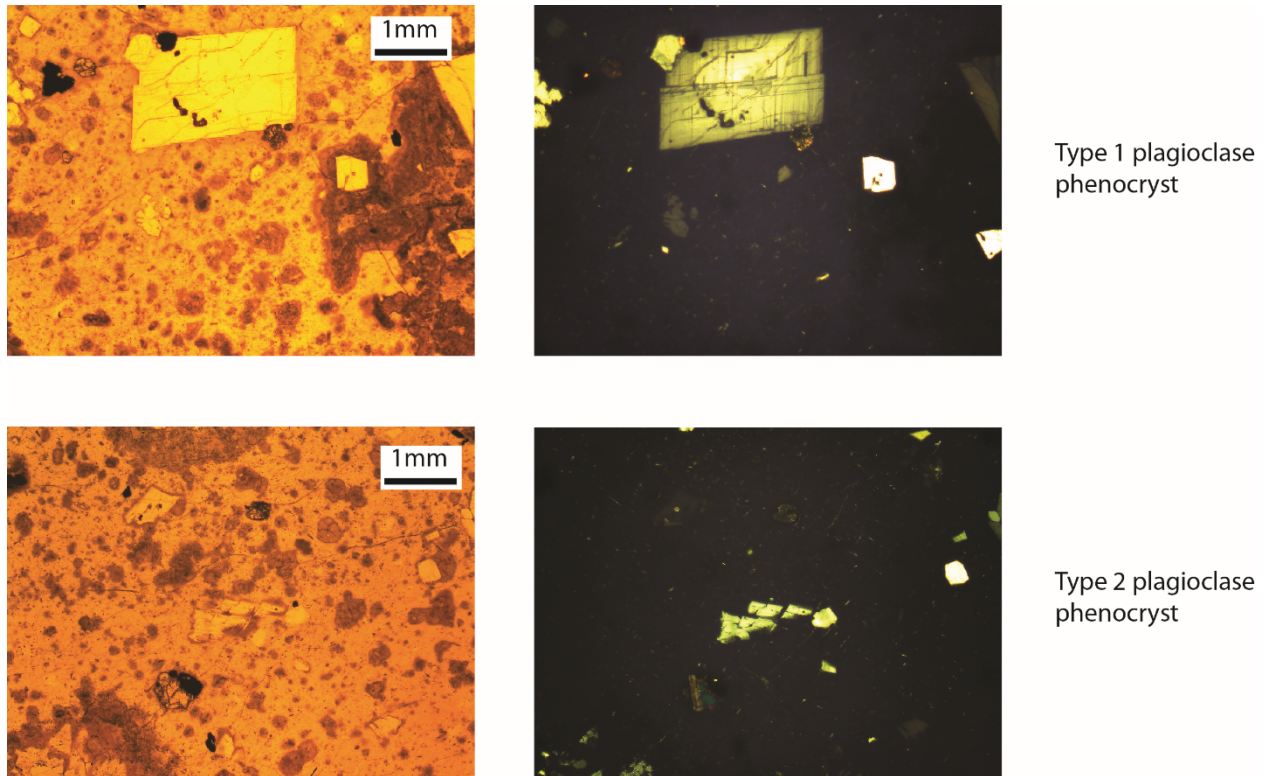


Figure 3.3 continued.

3.1.3 U-Pb Zircon Geochronology and Hf Analysis

Zircons separated from the microcrystalline core of the rhyolite of USGS-142 are pink to orange, euhedral to subhedral, and range from 50 to 100 μm long. A few phenocrysts are broken, which likely occurred during crushing of the rock sample. Zircons from the rhyolite of USGS-142 produced an average U-Pb age of 6.25 ± 0.7 (n = 17; 2σ here and henceforth, which includes random and systematic errors; Fig. 3.4) and a range of initial ϵHf values with a normal distribution from -9.7 to -5.5 (n = 12; average of -8.5 ± 0.9), and one outlier with an initial ϵHf value of -19.9 (U-Pb age of 6 Ma). Data tables for U-Pb and Hf analyses and cathodoluminescence images with spot locations for each zircon are provided in Appendix H.

Zircons separated from the microcrystalline core of the rhyolite of Butte Quarry are dark pink, euhedral, and range from 50 to 200 μm long. Zircons from the rhyolite of Butte Quarry produced an average U-Pb age of 8.13 ± 0.7 Ma ($n = 24$; Fig. 3.5) and a range of initial ϵ_{Hf} values with a normal distribution from -8.0 to -2.2 ($n = 14$; average of -5.3 ± 0.9).

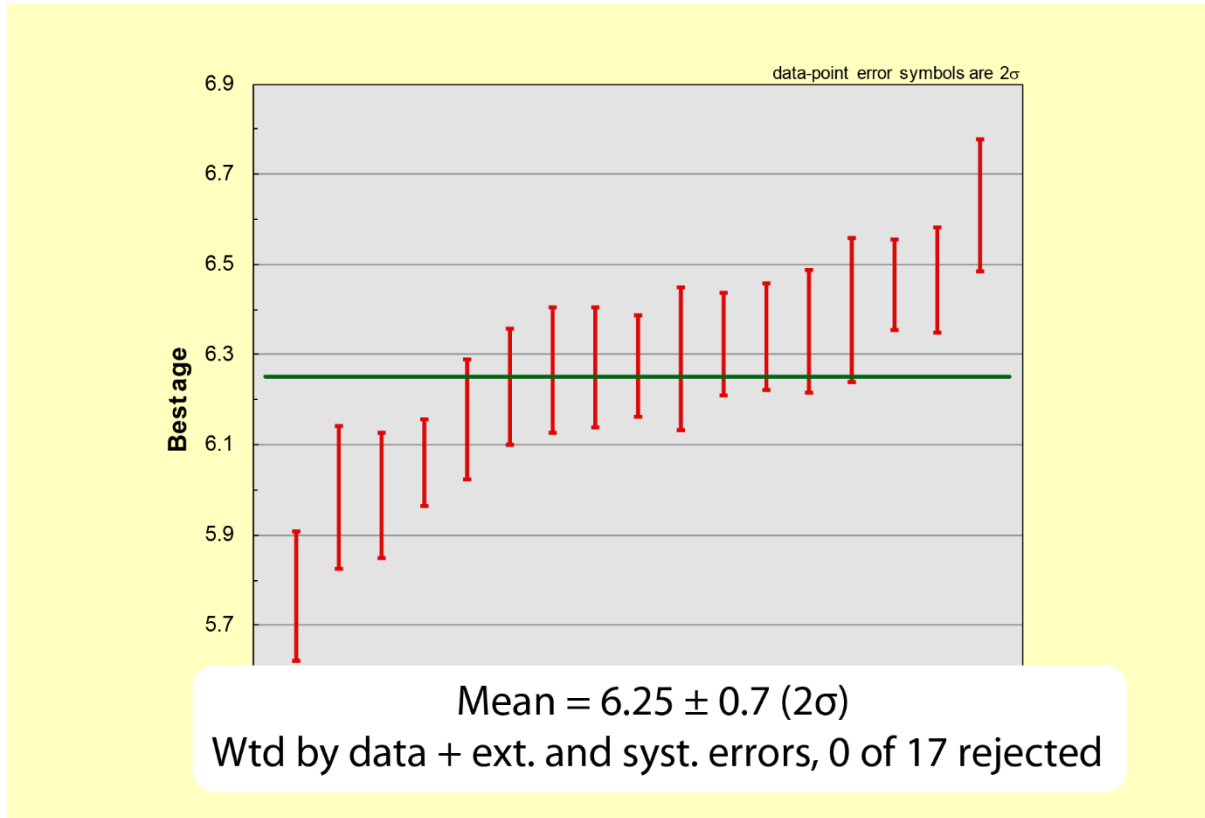


Figure 3.4: Weighted mean average age (green line) of U-Pb zircon geochronology for the rhyolite of USGS-142.

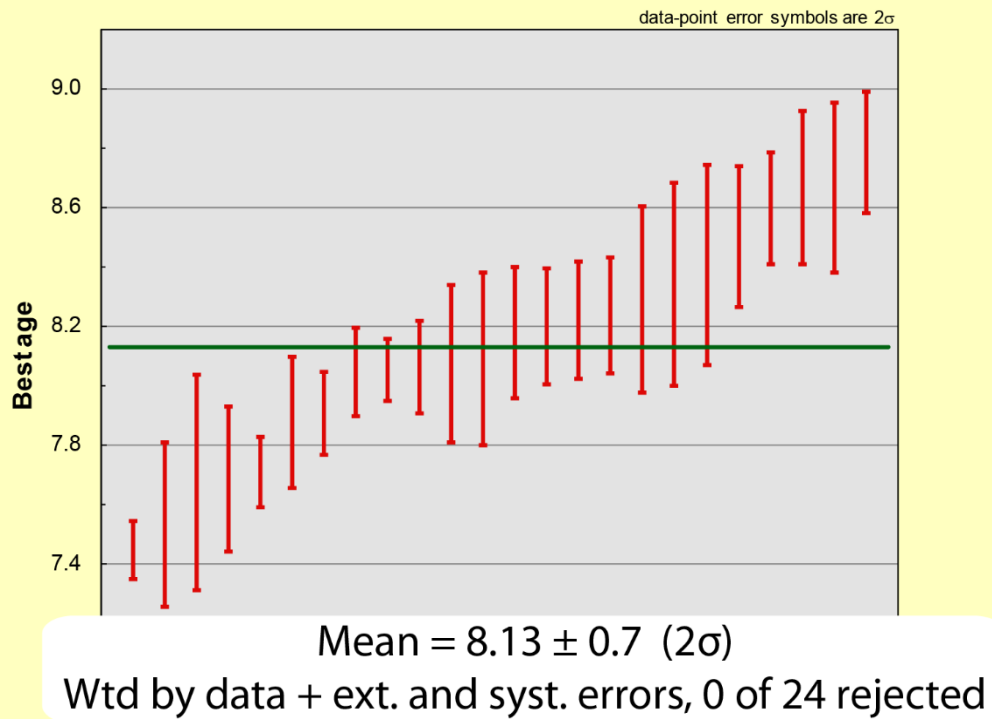


Figure 3.5: Weighted mean average age of U-Pb zircon geochronology (green line) for the rhyolite of Butte Quarry.

3.1.4 Ar-Ar Geochronology

Table 3.2 presents preliminary Ar-Ar age dating results for the rhyolites of USGS-142 and east side of the Arco Hills and Appendix F provides the raw data used to calculate the mean Ar-Ar age for each rhyolite. The rhyolite of USGS-142 produced an Ar-Ar age of 6.39 ± 0.13 Ma. The rhyolite of the east side of the Arco Hills produced an Ar-Ar age of 6.63 ± 0.05 .

Table 3.2: Ar-Ar age dating results

Unit	Age
USGS-142	6.39 ± 0.13
East side of the Arco Hills	6.63 ± 0.05

Table 3.2: Ar-Ar age dating results for the rhyolites of USGS-142 and east side of the Arco Hills.

3.1.5 $\delta^{18}\text{O}$ Isotope Analysis

Table 3.3 presents the $\delta^{18}\text{O}$ isotope analyses conducted on individual phenocrysts, which were calculated to produce a reliable $\delta^{18}\text{O}$ value for the melt to compare to previously studied Snake River-type rhyolites. Figure 3.6 illustrates the calculated $\delta^{18}\text{O}$ value of melt relative to VSMOW for several major and minor Heise and Picabo-aged rhyolites compared to the rhyolites of USGS-142 and Butte Quarry. The rhyolite of USGS-142 produced a $\delta^{18}\text{O}$ melt value of +4.7‰ to +5.0‰. The rhyolite of Butte Quarry produced a range of $\delta^{18}\text{O}$ melt values of +2.4‰ to +4.2‰. The rhyolite of the east side of the Arco Hills (16KS02) produced a calculated $\delta^{18}\text{O}$ melt value of +6.1‰. Uncertainties associated with individual phenocrysts analyses were consistently less than 0.1 ‰ (Appendix C). Isotope fractionation values, the method for calculating $\delta^{18}\text{O}$ of the melt, and the raw data given from the Stable Isotope Laboratory at University of Oregon are provided in Appendix C.

Table 3.3: $\delta^{18}\text{O}$ results

Unit	$\delta^{18}\text{O}_{\text{mineral}}$ (‰)			$\delta^{18}\text{O}_{\text{melt}}$	$\delta^{18}\text{O}_{\text{melt}}$
	Qtz	Plag	Pyx	(‰) Range	(‰) Average
USGS-142	-	-	3.2, 3.5	4.7-5.0	4.8
Butte Quarry	4.6, 2.3	2.1	-	2.4-4.2	3.3
East side of the Arco Hills	-	-	4.6	6.1	6.1

Table 3.3: $\delta^{18}\text{O}$ isotope analyses results measured from individual phenocrysts, recalculated for melt using methods and isotope fractionation values from Bindeman and Valley (2003) assuming 900°C for the temperature of the melt.

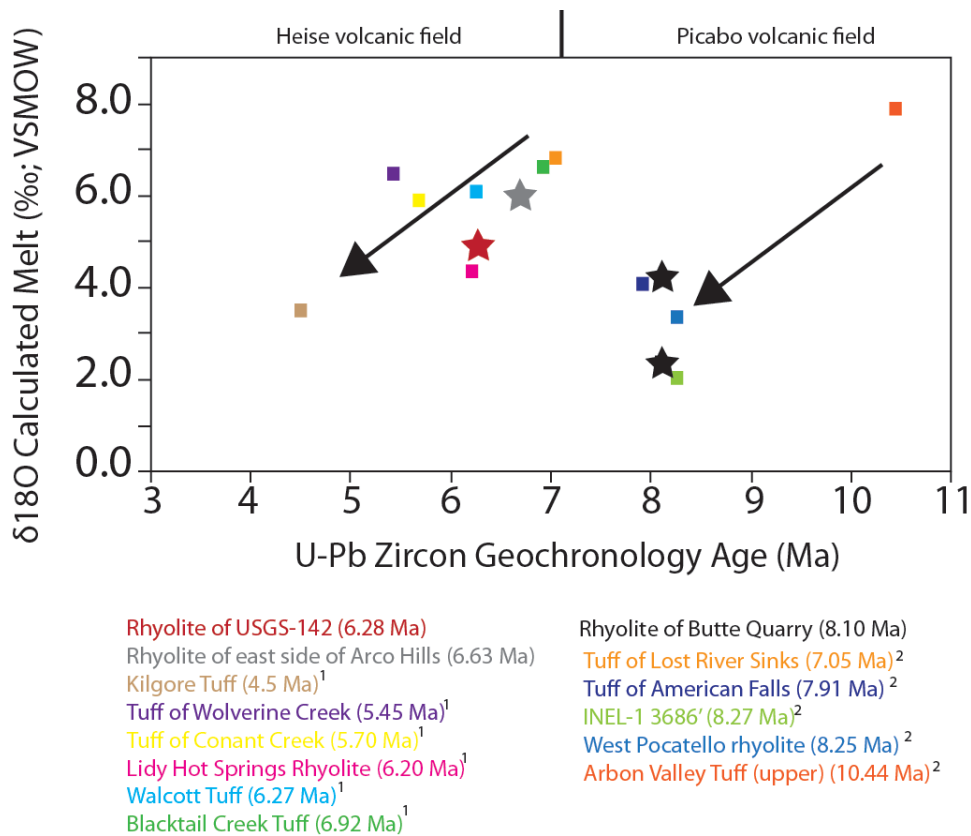


Figure 3.6: Calculated $\delta^{18}\text{O}$ melt values versus U-Pb zircon geochronology age for the rhyolites of USGS-142 and Butte Quarry compared to analyses conducted on other Heise and Picabo-aged rhyolites; the rhyolite of the east side of the Arco Hills is displayed relative to its Ar-Ar age. Black arrows show the decreasing $\delta^{18}\text{O}$ values with time for each volcanic field. Values for Heise and Picabo-aged rhyolites are taken from (1) Watts et al. (2011) and (2) Drew et al. (2013).

3.1.6 X-Ray Fluorescence

XRF analyses from the rhyolites of USGS-142 and Butte Quarry were compared to previously analyzed major and minor Heise and Picabo rhyolites (Figs. 3.7 and 3.8).

Because the U-Pb zircon ages presented above allow for the rhyolites of USGS-142 and Butte Quarry to be categorized into the Heise and Picabo volcanic fields, respectively, comparison between major and trace elements for either rhyolite was constrained to previously-studied rhyolites that have similar U-Pb zircon ages.

3.1.6.1 Major element geochemistry

Spider diagrams are presented below that compare the major element geochemistry of the rhyolites of USGS-142 (Fig. 3.7) and Butte Quarry (Fig. 3.8) to other known Heise and Picabo-aged ignimbrites, respectively, conducted by Watts et al. (2011), McCurry and Rodgers (2009), and Drew et al. (2013). Major elements were normalized to the published data for the Blacktail Creek Tuff by Watts et al. (2011) to allow for differentiation among Snake River-type rhyolites, which have similar major element geochemistry.

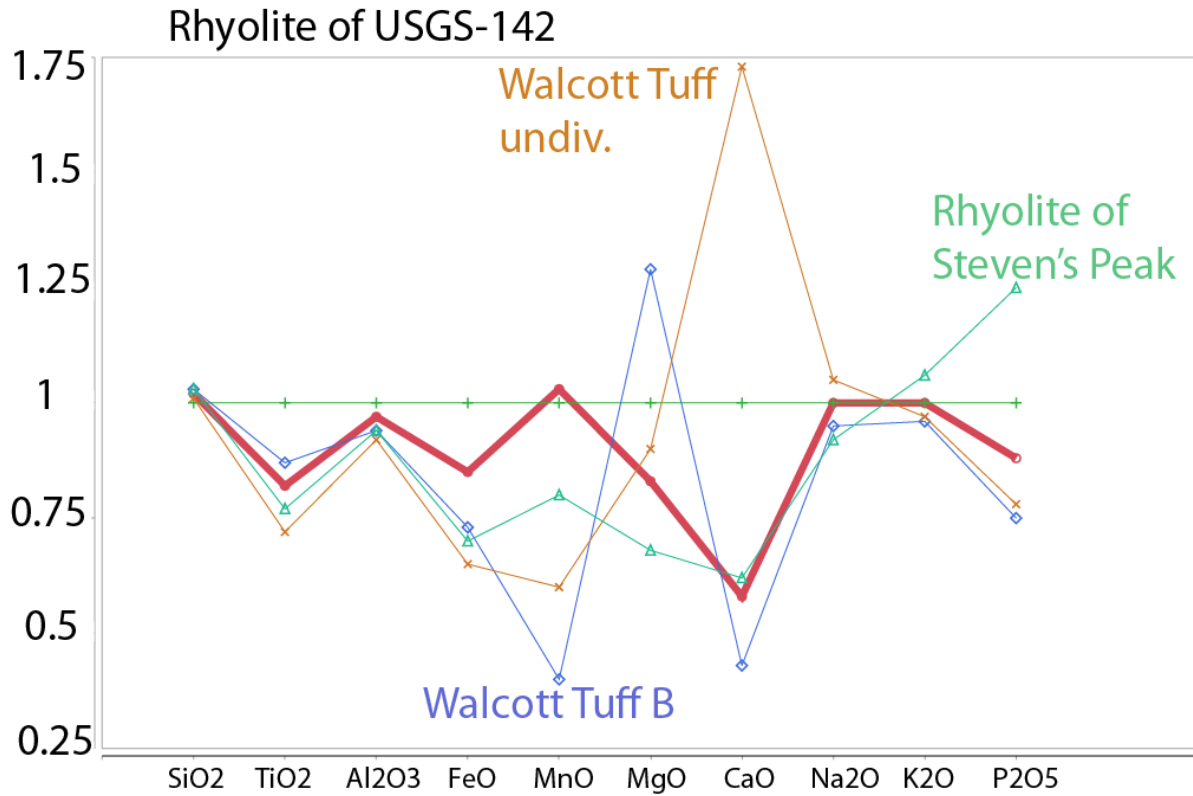


Figure 3.7: Spider diagram comparing the major element geochemistry of the rhyolite of USGS-142 (thick red line) and selected Heise-aged rhyolites normalized to the major element geochemistry of the Blacktail Creek Tuff (thin horizontal green line) conducted by Watts et al. (2011). Whole rock geochemistry data is provided in section 5.1.

Rhyolite of Butte Quarry

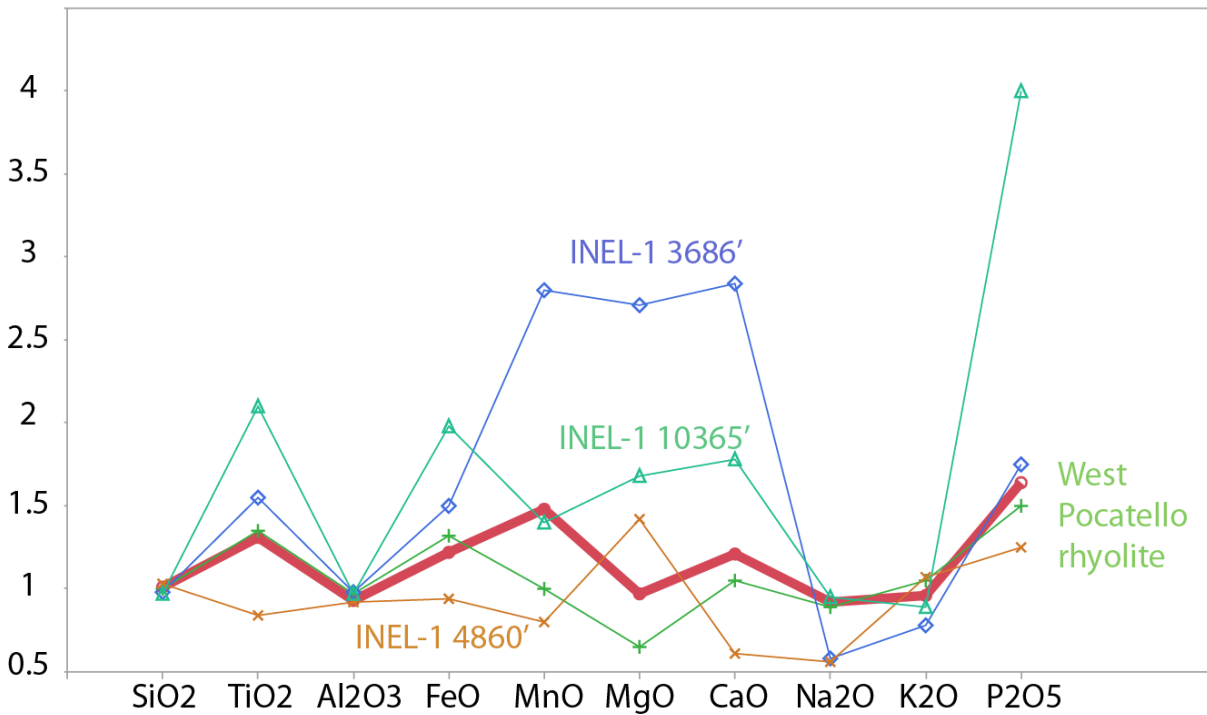


Figure 3.8: Spider diagram comparing the major element geochemistry of the rhyolite of Butte Quarry (thick red line) and Picabo-aged rhyolites normalized to the major element geochemistry of the Blacktail Creek Tuff (thin horizontal green line) conducted by Watts et al. (2011). Whole rock geochemistry data is provided in section 5.1.

3.1.6.2 Trace element geochemistry

Tables 3.4 and 3.5 provide summaries of the trace element geochemistry (in parts per million) for the rhyolites of USGS-142 and Butte Quarry compared to analyses conducted on Heise and Picabo-aged ignimbrites, respectively, by Watts et al. (2011), McCurry and Rodgers (2009), and Drew et al. (2013).

Unit	Rhyolite of USGS-142	Kilgore Tuff (1)	Conant Creek Tuff (1)	Wolverine Creek Tuff (1)	Lidy Hot Springs Rhyolite (1)	Rhyolite lava of WO-2 (2)	Walcott tuff B (2)	Rhyolite lava of lower WO-2 (2)	Walcott Tuff undivided (1)	Blacktail Creek Tuff of WO-2 (2)	Blacktail Creek Tuff (1)	Rhyolite of Steven's Peak (3)	Rhyolite of Steven's Peak 2 (3)
<i>Trace element analyses by XRF (ppm)</i>													
Trace													
Ba	1057.9	889.80	509	573	840	1069	1015	643	914	607	1099	888.2	1044
Ce	162.1	156.40	159	154	126				136		120	132.4	132.9
Cl	92												
Cr	2.2	2.83	5	8	1				2		2	4.2	4
Cu	4.4	6.50	4	5	0				5		1	2.5	1.8
F	385												
Ga	21	19.67	22	22	17				17		18	16.7	18.1
La	92.5	85.80	81	78	67				71		66	67.9	69.9
Nb	50.3	47.83	56	54	41				41		32	43.4	44.3
Nd	70.6	62.17	65	61	48				54		45	53	57.2
Ni	4.4	3.17	2	5	0				3		4	1.6	1.6
Pb	31.8	25.33	26	28	25				23		26	26.9	31
Rb	204	176.60	147	165	181				171		174	167	149.1
S	n.d.												
Sc	2.2	4.17	3	2	3				3		5	2.8	5.6
Sm	12.2												
Sr	47.1	27.40	25	40	29	65	40	34	39	38	84	27.3	95.2
Th	32.5	26.60	26	25	28				26		27	27	24.2
U	7.4	6.60	5	6	9				7		7	8.3	6.5
V	8.4	5.17	2	9	2				24		9	8.5	8.1
Y	68.6	55.00	77	75					54		44	57.6	65.6
Zn	91.5	64.67	90	86	45				41		61	56.8	75.7
Zr	300.1	320.40	273	185	239	399	258	259	221	226	327	234.7	510.4

Table 3.4: Trace element geochemistry of the rhyolite of USGS-142 compared to other Heise-aged rhyolites. Numbers in the top row indicate the publication; (1) = Watts et al. (2011), (2) = McCurry and Rodgers (2009), (3) = Drew et al. (2013).

Table 3.5: Trace element geochemistry of the rhyolite of Butte Quarry compared to previously analyzed Picabo-aged rhyolites

Unit	Rhyolite of Butte Quarry	West Pocatello rhyolite (3)	INEL-1 3686' (2)	INEL-1 4860' (2)	INEL-1 10365' (2)	Tuff of Lost River Sinks (3)	Tuff of American Falls (3)
<i>Trace element analyses by XRF (ppm)</i>							
Trace							
Ba	1109.7	1085.6	1090	970	963	837.5	1869.6
Ce	168.5	143.4				119.5	125.2
Cl	79						
Cr	0.7	3.9				5.6	11.4
Cu	5.3	2.7				2.2	9.9
F	328						
Ga	17.8	18.9				16.8	21
La	87	74.6				63.8	67.2
Nb	49.9	46.2				35.3	40
Nd	73.1	59.2	79	71	55	44.3	54.6
Ni	2.4	4.6				4.8	6.8
Pb	27.6	25.3				28.7	23
Rb	165.7	165.4	129	216	171	176.7	114.2
S	1472						
Sc	5.9	4.1				2.5	7.4
Sm	11.8			14	11		
Sr	74.3	87.2	118	70	128	69	174.5
Th	29.9	25.6	32.3	29.9	27.4	29.4	18.4
U	8.1	8.1	5.3	6.9	6.5	8	6.1
V	9.1	7.5				6.8	32.1
Y	71.6	62.4				49.9	54.7
Zn	68.7	66.4				57.8	84.4
Zr	584.5	523	523	420	539	299.6	719.8

Table 3.5: Trace element geochemistry of the rhyolite of Butte Quarry compared to other Picabo-aged rhyolites. Numbers in the top row indicate the publication; (2) = McCurry and Rodgers (2009), (3) = Drew et al. (2013).

3.2 Results for Fault Analysis

3.2.1 Collective Analysis of Northeast-Striking Faults

The southern Arco Hills contain a bimodal distribution of fault orientations: northeast-striking and northwest-striking (Fig. 3.9). Due to the limited exposures of fault surfaces, cross-cutting relationships between these two fault sets were not recognized in the field area. However, Zentner (1989) and Bruhn et al. (1992) documented that northeast-striking faults cross-cut northwest-striking faults in the Beaverhead Mountains and the Lemhi Range, respectively. Recorded northwest-striking faults in the Arco Hills slip dominantly toward the west-southwest, and recorded northeast-striking faults slip either to the northwest or southeast (depending on their dip direction), suggesting that the strain fields for the different fault sets are not compatible (e.g. Marrett and Allmendinger, 1990). Northwest-striking faults are well-known to accommodate Basin and Range extension because large range-bounding faults, such as the Lost River fault, strike northwest (Anders et al., 1989). Therefore, analysis was focused on northeast-striking faults in the Arco Hills because this set is of most interest to the regional deformation around the ESRP and potential lateral displacement of the ESRP relative to the Basin and Range tectonic province (Payne et al., 2012).

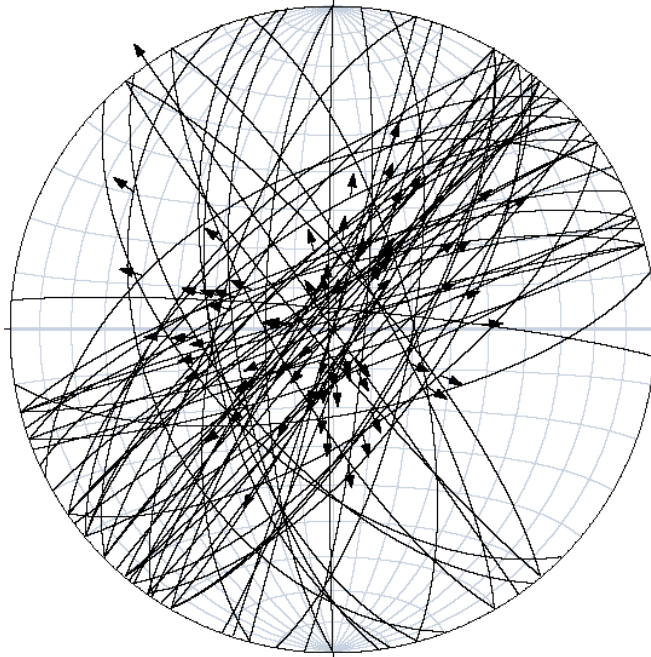


Figure 3.9: Lower hemisphere, equal area stereogram, with faults plotted as great circles and slickenlines plotted as arrows, which show hanging wall slip direction for all measured faults of the Arco Hills (n = 70).

Figure 3.11 displays all measured northeast-striking faults of the Arco Hills on a lower hemisphere, equal area stereogram showing great circles with hanging wall slip direction. Exposed fault surfaces occur throughout the Mississippian Scott Peak Formation in the Arco Hills, are usually no larger than $\frac{1}{2}$ m², and are almost exclusively preserved in chert-rich intervals of the Mississippian Scott Peak Formation. Most of the northeast-striking faults are lined with and preserved on orange silicified planes of microcrystalline silica. Furthermore, parallel-striking fracture networks are also marked by orange silicified planes of microcrystalline silica, and are often found near (a few meters) measured fault surfaces. The host rocks are often brecciated outboard from measured fault surfaces, where dark-gray to black chert and orange silicified microcrystalline silica form a matrix-supported breccia (Fig. 3.10). However, breccia is not always found near fault surfaces.

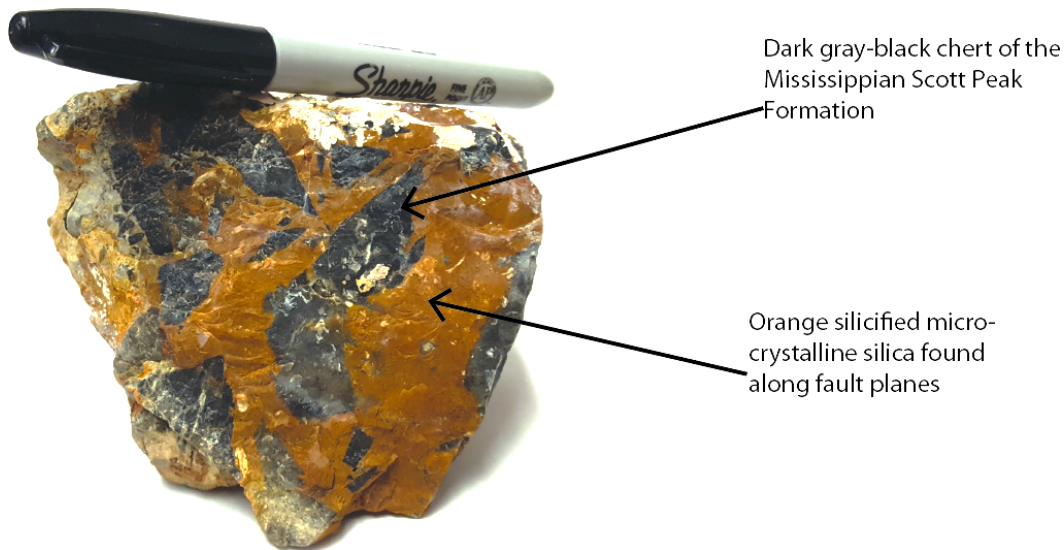


Figure 3.10: Hand sample of matrix-supported breccia with clasts of dark-gray to black chert in a matrix of orange silicified microcrystalline silica.

All faults that exhibit down-dip slickenlines, where the sense of slip could be determined, demonstrate a normal sense of slip. However, the sense of slip on some faults was poorly constrained due to limited exposures of fault surfaces or marker horizons. Therefore, in the presence of down-dip slickenlines, but in the absence of kinematic indicators or offset marker beds, faults were inferred to have slipped in a normal sense. In general, the northeast-striking faults are small displacement magnitude (<10m), and dip both toward the ESRP (southeast) and away from the ESRP (northwest) at angles of 90° to 50° with dips generally greater than 70° (Appendix G). A plot of 50 poles to fault planes yields an average fault strike of 226° and a dip of 88° (right hand rule); the average strike of the northeast-striking faults in the Arco Hills is just slightly north of the trend of the ESRP of ~052° (McQuarrie and Rodgers, 1998).

Figure 3.12 displays the fault plane solution produced from the analyzed kinematic data of every measured northeast-striking fault of the Arco Hills ($n = 50$). This fault plane solution illustrates a steeply plunging northwest to southeast extension direction. The northeast-striking faults collectively record nearly exclusively dip-slip extension.

Table 3.6 displays the values produced from analyzing the eigenvalues calculated from Stereonet[®] 9 (Allmendinger et al., 2012) using the Bingham Analysis; raw data for eigenvalues are provided in Appendix E. Poles to fault planes display a clustered habit ($K = 9.38$) and low scatter ($\ln(\lambda_1/\lambda_3) = 2.57$). Shortening axes display a slightly girdled habit ($K = 0.81$) and low scatter ($\ln(\lambda_1/\lambda_3) = 1.78$). Extension axes display a slightly girdled habit ($K = 0.87$) and low scatter ($\ln(\lambda_1/\lambda_3) = 1.89$).

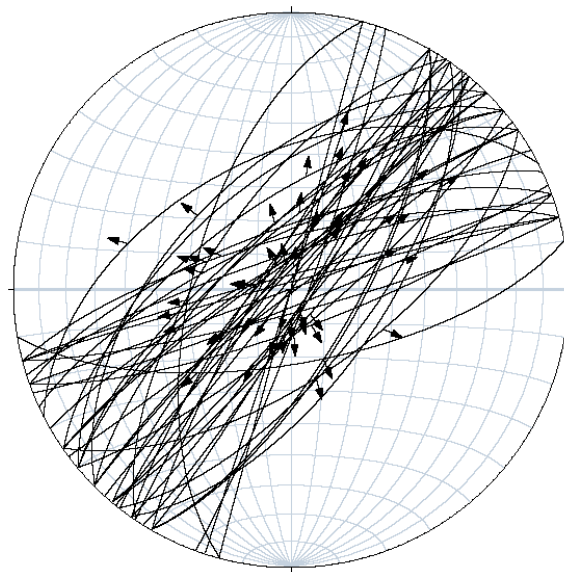


Figure 3.11: Lower hemisphere, equal area projection of great circles with hanging wall slip direction (arrows) for the northeast-striking faults of the Arco Hills ($n = 50$).

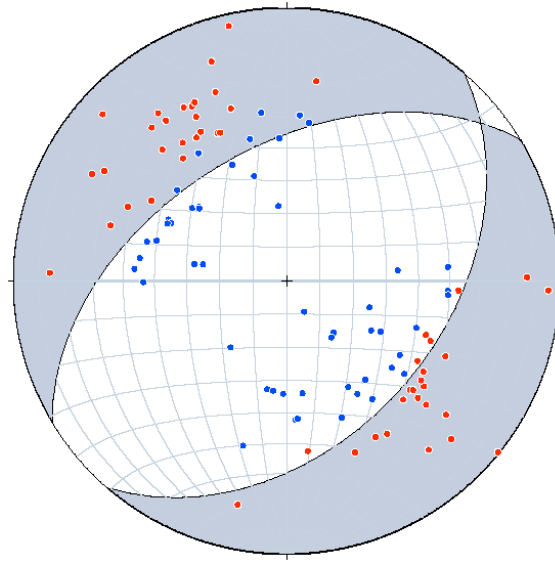


Figure 3.12: Fault plane solution produced from FaultKin, displaying all kinematic data recorded from the northeast-striking faults of the Arco Hills ($n = 50$). Shortening axes (blue) and extension axes (red) were calculated from the attitude, sense of slip, and orientation of slip direction (rake).

Table 3.6: Quantitative analysis of fit and habit of all measured faults

	Poles to Fault Planes	Shortening Axes	Extension Axes
K	9.38	0.81	0.87
Fit	2.57	1.78	1.89

Table 3.6: Quantitative analysis of fit and habit using eigenvalues ($\lambda_1, \lambda_2, \lambda_3$) calculated in Stereonet[®] 9 (Allmendinger et al., 2012). K is defined as $\ln(\lambda_1/\lambda_2)/\ln(\lambda_2/\lambda_3)$; as K approaches infinity, data display a perfect cluster habit; as K approaches 0 data display a perfect girdled habit. Fit is defined as $\ln(\lambda_1/\lambda_3)$, which approaches infinity as fit increases (Woodcock, 1977).

3.2.2 Spatial Pattern in Brittle Deformation

To evaluate the possibility that there is a spatial pattern to fault orientation, northeast-striking faults were divided by location relative to the 20° fold-plunge contour of McQuarrie and Rodgers (1998), separating two domains of faults: distal and proximal to the ESRP (Fig. 3.13). Figure 3.14 (distal faults) and figure 3.15 (proximal faults) are displayed below as fault plane solutions created from FaultKin (Allmendinger et al., 2012). Faults proximal to the ESRP record a southeast-plunging extension direction; faults distal to the ESRP record a northwest-plunging extension direction.

Distal Faults

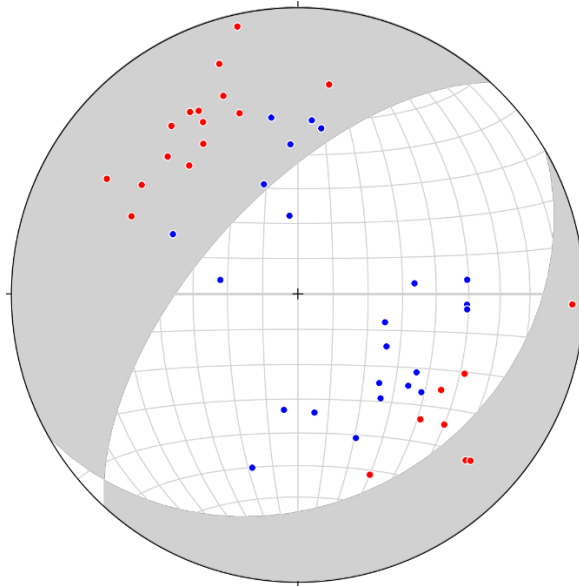


Figure 3.14: Fault plane solution of the northeast-striking faults ($n = 22$) found northwest of the 20° fold-plunge contour from McQuarrie and Rodgers (1998). These faults are referred to as the distal faults relative to the ESRP. Shortening axes (blue) and extension axes (red) were calculated from the attitude, sense of slip, and orientation of slip direction (rake).

Proximal Faults

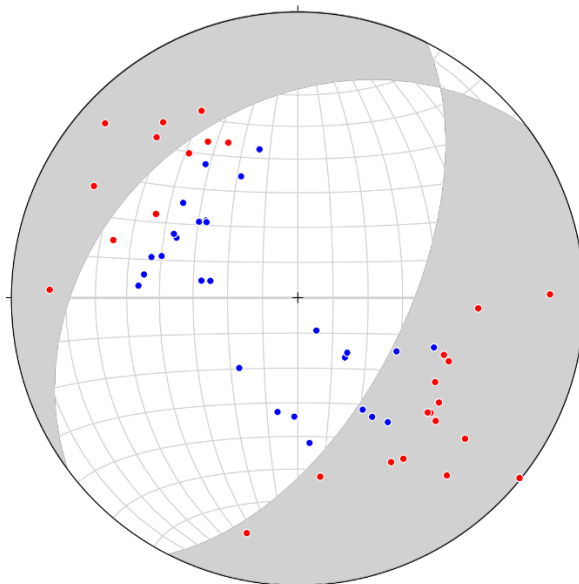


Figure 3.15: Fault plane solution of the northeast-striking faults ($n = 28$) found southeast of the 20° fold-plunge contour from McQuarrie and Rodgers (1998). These faults are referred to as the proximal faults relative to the ESRP. Shortening axes (blue) and extension axes (red) were calculated from the attitude, sense of slip, and orientation of slip direction (rake).

Mean vectors were calculated to determine if the poles to fault planes varied systematically between domains. A mean vector was calculated using Stereonet[®] 9 (Allmendinger et al., 2012) for the poles to northwest-dipping faults and southeast-dipping faults in each fault domain. The poles to northwest-dipping faults in the distal domain display a steeper magnitude of plunge relative to the northwest-dipping faults in the proximal domain (Table 3.7). Conversely, poles to southeast-dipping faults in the distal domain exhibit a shallower magnitude of plunge compared to the southeast-dipping faults in the proximal domain. However, the mean vectors from each fault domain are statistically indistinguishable.

Table 3.7: Mean vector analysis for poles to fault planes

Dip direction	N	Distal	N	Proximal
Northwest	15	141, 12 ± 7.7	12	139.5, 18 ± 11.5
Southeast	7	322, 14.9 ± 16.1	16	308.6, 9.1 ± 9.1

Table 3.7: Mean vector analyses for the poles to the northeast-striking fault planes, divided by their domain (relative to the ESRP), and by their dip. Northwest-dipping poles to fault planes increase in magnitude of plunge closer to the ESRP. Conversely, southeast-dipping poles to fault planes decrease in magnitude of plunge closer to the ESRP.

Mean vector analyses were also calculated for the magnitude of plunge of shortening axes to determine if they show a similar pattern to the poles to fault planes, and to provide a statistical analysis to evaluate the observations from FaultKin (Marrett and Allmendinger, 1990; Allmendinger et al., 2012). Shortening axes in the distal fault domain yield a steep southeasterly plunge compared to the shortening axes in the proximal domain, which yield a steep northwesterly plunge (Fig 3.16).

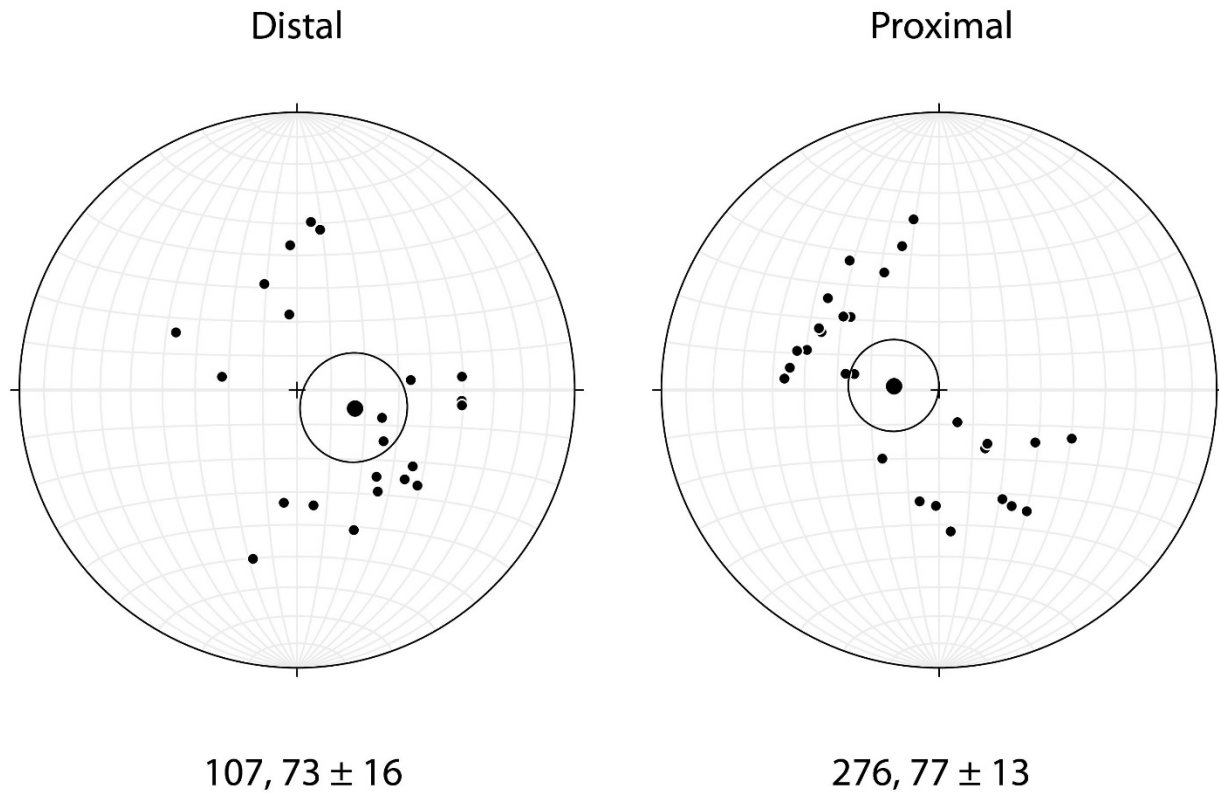


Figure 3.16: Lower hemisphere, equal area stereograms showing the shortening axes of the distal and proximal fault domains and their mean vector analyses. The circle around the mean vector outlines the uncertainty of the trend and plunge of the mean vector.

Table 3.8 displays the values produced from analyzing the eigenvalues calculated from Stereonet[®] 9 using the Bingham axial distribution analysis (Allmendinger et al., 2012; raw data for eigenvalues are provided in Appendix E). Figures of poles to fault planes, shortening and extension axes, contoured with a distribution of 2σ with 95% confidence for each fault domain (proximal and distal) and collective analyses are provided in figure 3.17. Poles to fault planes in both domains display a clustered habit and low scatter (Table 3.8). Distal domain shortening axes display a slightly clustered habit ($K = 1.66$) and low scatter ($\ln(\lambda_1/\lambda_3) = 1.77$). Proximal domain shortening axes display a slightly girdled habit ($K = 0.63$) and low scatter ($\ln(\lambda_1/\lambda_3) = 2.43$). Distal domain extension axes display a

slightly clustered habit ($K = 1.43$) and low scatter ($\ln (\lambda_1/\lambda_3) = 2.17$). Proximal domain extension axes have no preference in habit ($K=0.98$) and low scatter ($\ln (\lambda_1/\lambda_3) = 1.84$).

Table 3.8: Quantitative analysis of fit of each fault domain

	Distal Domain			Proximal Domain		
	Poles to Fault Planes	Shortening Axes	Extension Axes	Poles to Fault Planes	Shortening Axes	Extension Axes
K	11.00	1.66	1.43	9.50	0.63	0.98
Fit	2.76	1.77	2.17	2.49	2.43	1.84

Table 3.8: Quantitative analysis of fit and habit using eigenvalues ($\lambda_1, \lambda_2, \lambda_3$) (Woodcock, 1977) calculated in Stereonet[®] (Allmendinger et al., 2012). K is defined as $\ln (\lambda_1/ \lambda_2)/\ln(\lambda_2/ \lambda_3)$; as K approaches infinity data display a perfect cluster habit, as K approaches 0 data display a perfect girdled habit. Fit is defined as $\ln (\lambda_1/ \lambda_3)$, which approaches infinity as fit increases (Woodcock, 1977).

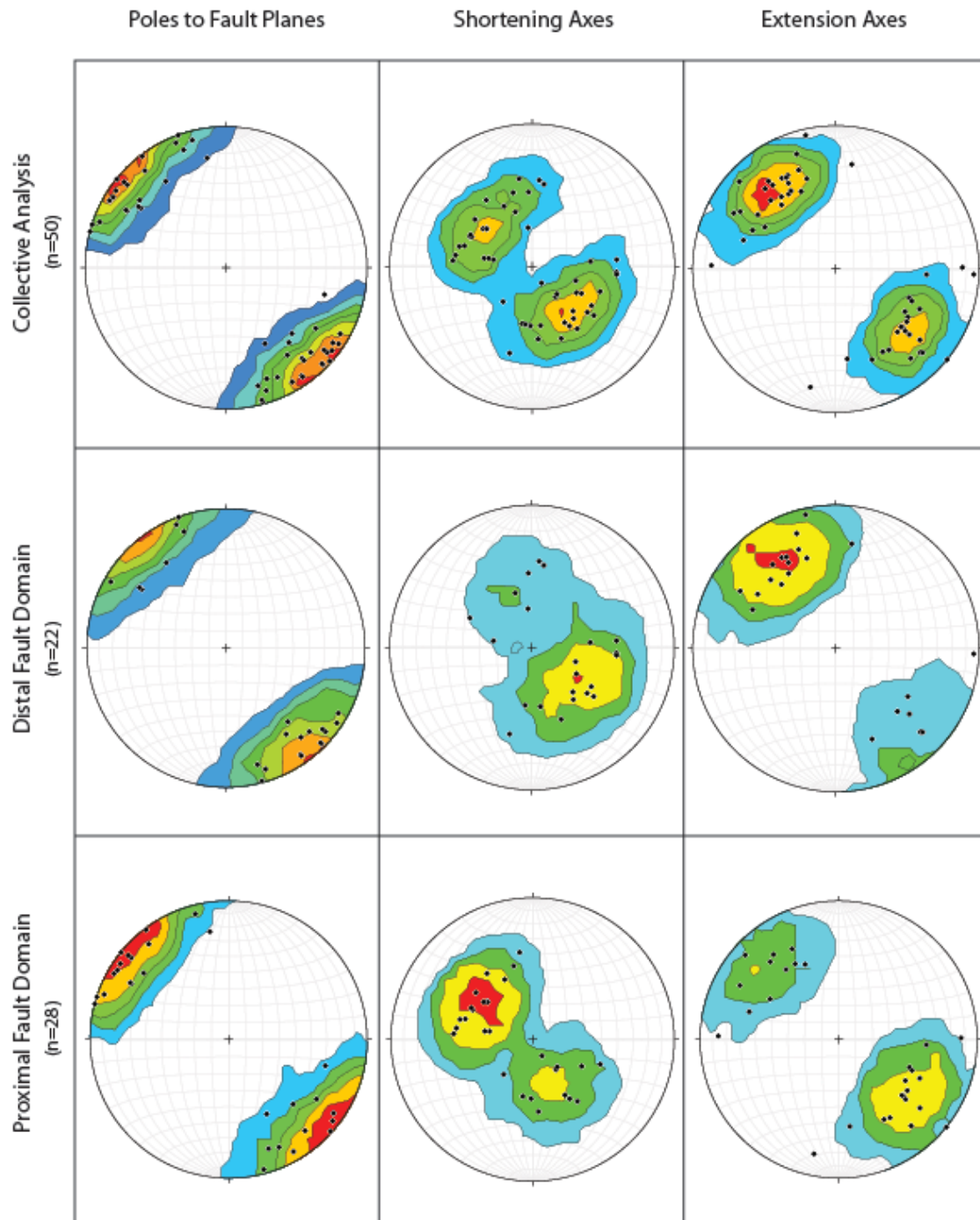


Figure 3.17: Lower hemisphere, equal area projections of the northeast-striking fault kinematic data for the Arco Hills, separated by a collective analysis, and by each fault domain. Solid dots represent poles to fault planes, shortening axes, or extension axes. Each colored contour represents distributions of 2σ with 95% uncertainty; red and yellow shaded regions represent areas with a higher density of data points, and green and blue shaded regions represent areas with a lower density of data points.

CHAPTER 4: DISCUSSION

4.1 Rhyolite Correlation

Petrographic examinations of the upper and/or lower vitrophyres of the studied rhyolites (USGS-142, Butte Quarry, and east side of Arco Hills) indicate that the matrices are composed of cusped glass shards, which were flattened and plastically deformed likely due to their high temperature of deposition (Figs. 3.1 and 3.2). Furthermore, broken phenocryst fragments occur in the studied vitrophyres and in the lowest unwelded portion of the rhyolite of USGS-142. Both of these observations suggest that the rhyolites of USGS-142, Butte Quarry, and east side of the Arco Hills are ignimbrites rather than lava flows, because lava flows generally display widespread basal autobrecciation and a lack of broken phenocrysts and cusped glass shards within the vitrophyres (Branney and Kokelaar, 1992; Branney et al., 2008).

Preliminary thin section examinations of the lower vitrophyre of the West Pocatello rhyolite could not successfully differentiate between a lava flow and an ignimbrite. Matrix textures such as cusped glass shards were not observed in the two thin sections created from this vitrophyre, which would have indicated a pyroclastic origin for this rhyolite. In addition, Drew et al. (2013) did not describe basal autobrecciation in outcrops of the West Pocatello rhyolite, which would have suggested that the West Pocatello rhyolite is a lava flow. Therefore, further outcrop-scale and petrographic analyses must be conducted to determine if it is an ignimbrite or a lava flow.

Table 4.1: Data compilation of Snake River-type rhyolites									
Volcanic Field	Unit Name	Deposit Type	Surface or borehole	Ar-Ar age (Ma)	U-Pb Zircon age (Ma)	$\delta^{18}\text{O}_{\text{melt}}$ (‰)	ϵ_{Hf} (*=inferred from Nd) Vervoort et al. (1999)	ϵ_{Nd} (*=inferred from Hf) Vervoort et al. (1999)	Petrographic descriptions/ phenocryst modes
Heise	Rhyolite of USGS-142	Ignimbrite	Borehole	6.39 ± 0.13	6.25 ± 0.7	4.7-5.0	-8.5 ± 0.9	-8.4 ± 0.9	3.7% phenocrysts of plag >> cpx > san = qtz > opq, trace zirc, apatite, and opx
Picabo	Rhyolite of Butte Quarry	Ignimbrite	Surface	-	8.13 ± 0.7	2.4-4.2	-5.3 ± 0.9	-6.0 ± 0.9	3.0% phenocrysts of plag >> cpx = qtz > san = opx = opq, trace zirc and apatite
Heise (?)	Rhyolite of the east side of the Arco Hills	Ignimbrite	Surface	6.63 ± 0.05	-	6.1	-	-	Very crystal poor (~1%) plag >> mt = cpx > ilm, trace zirc and apatite
Heise	Kilgore Tuff	Ignimbrite	Surface and possibly boreholes 2-2A and INEL-1	4.61 ± 0.01 (1) 4.45 ± 0.05 (5)	4.49 ± 0.25 4.59 ± 0.26 (4)	3.3-3.6 (2) 3.3 (4)	-7.454 to -10.1332 *	-7.65 to -9.62 (2)	Morgan and McIntosh (2005): 2-10% phenocrysts of plag >> san > aug > mt > zirc
Heise	Tuff of Wolverine Creek	Ignimbrite	Surface and borehole WO-2	5.72 ± 0.03 (1)	5.45 ± 0.14 (4)	6.5 (2) 6.1 (4)	-5.142*	-5.95 (2)	Morgan and McIntosh (2005): Upper unit orange to pink, crystal poor containing <1% phenocrysts of plag >> aug > enst > san >> zirc = mt
Heise	tuff of Conant Creek	Ignimbrite	Surface and borehole WO-2	6.01 ± 0.07 (1) 5.51 ± 0.13 (5)	5.70 ± 0.19 (4)	5.9 (2) 5.8 (4)	-6.20*	-6.73 (2)	Morgan and McIntosh (2005): Very crystal poor ignimbrite with a nearly aphyric basal vitrophyre Anders et al. (2014) indicate 10% feldspar phenocrysts near base.
Heise	Rhyolite of Upper WO-2	Lava	Borehole WO-2	6.21 ± 0.02 (1)	-	-	-	-	Anders et al. (2014): 15-20% phenocrysts of mostly sanidine McCurry and Rodgers (2009): 9% phenocrysts of plag >> qtz = cpx = opx = san = mt >> ilm, zirc, ap
Heise	Tuff of WO-2	Ignimbrite	Borehole WO-2	6.23 ± 0.14 (1)	-	-	-	-	Anders et al. (2014) indicate presence of sanidine and quartz, and that the ignimbrite is pink and eutaxitic.
Heise	Walcott Tuff undivided	Ignimbrite	Surface and borehole WO-2	6.27 ± 0.04 (5)	6.37 ± 0.26 (4)	6.1 (2) 5.9 (4)	-9.73*	-9.32 (2)	Morgan and McIntosh (2005): Crystal poor ignimbrite with less than 2% total phenocrysts of plag >> qtz > aug > opx > opq > zircon Anders et al. (2014): speculate that the Walcott Tuff B of borehole WO-2 is similar in texture to surficial exposures, suggesting that the Walcott Tuff undivided is the Walcott Tuff B
Heise	Walcott Tuff A	Ignimbrite	Borehole WO-2	6.26 ± 0.02 (1)	-	-	-	-	Anders et al. (2014): 1% feldspars and plagioclase phenocrysts with distinct orange glass shards.
Heise	Walcott Tuff B	Ignimbrite	Borehole WO-2 (4209')	6.27 ± 0.01 (1)	-	-	-8.338*	-8.3 (6)	McCurry and Rodgers (2009): 10% phenocrysts of san > plag >> pyx, mt >> ilm > zirc, ap (?) Anders et al. (2014): 1-2% feldspar crystals ~1-2mm; indicate that this ignimbrite is similar in texture to surface outcrops.

Data compilation of Heise and Picabo-age Snake River-type rhyolites . Stars indicate ϵ_{Hf} values calculated from ϵ_{Nd} values (and vice versa) using the "Terrestrial Array" equation provided by Vervoort et al. (1999). (1) = Anders et al. (2014); (2) = Watts et al. (2011); (3) Drew et al. (2013); (4) = Bindeman et al. (2007); (5) Morgan and McIntosh (2005); (6) = McCurry and Rodgers (2009); (7) = Anders et al. (2009).

Table 4.1

Table 4.1: Data compilation of Snake River-type rhyolites									
Volcanic Field	Unit Name	Deposit Type	Surface or borehole	Ar-Ar age (Ma)	U-Pb Zircon age (Ma)	$\delta^{18}\text{O}_{\text{melt}}$ (‰)	ϵHf (*=inferred from Nd) Vervoort et al. (1999)	ϵNd (*=inferred from Hf) Vervoort et al. (1999)	Petrographic descriptions/ phenocryst modes
Heise	Lidy Hot Springs rhyolite	Lava	southern Beaverheads, near Lidy Hot Springs	6.20 ± 0.04 (5)	-	4.4 (2)	-10.23*	-9.69 (2)	Morgan and McIntosh (2005) indicate presence of tiny and sparse phenocrysts of sanidine and quartz
Heise	Rhyolite of Lower WO-2	Lava	WO-2	6.45±0.02 (1)	-	-	-	-	McCurry and Rodgers (2009): 20% phenocrysts of plag > san, qtz >> pyx, mt >> ilm > zirc, ap, chev
Heise	Blacktail Creek Tuff	Ignimbrite	Surface and borehole WO-2	6.66±0.01 (1) 6.63 ± 0.03 (5)	6.92 ± 0.28 (4)	6.6 (2) 6.0 (4)	-10.11*	-9.60 (2)	Anders et al. (2014): 20-25% phenocrysts of san >> qtz >> amph (<0.1%) Morgan and McIntosh (2005): 10-20% phenocrysts of plag > qtz > san > aug > opq > zirc McCurry and Rodgers (2009): 17% phenocrysts of san >> qtz >> pyx = mt >> zirc
?	Rhyolite of Steven's Peak	Ignimbrite	South margin of ESRP	-	6.62 ± 0.12 (3)	5.9 (3)	-9.5 (3)	-7.6	Drew et al. (2013): 5-10% phenocrysts, lithophysae tuff with spherulites and a basal vitrophyre
?	Rhyolite of Steven's Peak 2	Ignimbrite	South margin of ESRP	-	6.86 ± 0.19	4.7 (3)	-9.7 (3)	-7.8 (3)	Drew et al. (2013): 10-15 % phenocrysts, description similar to Rhyolite of Steven's Peak, distinguished by U-Pb zircon ages and whole rock geochemistry
Picabo	Tuff of American Falls	Ignimbrite	South margin of ESRP	-	7.91 ± 0.16 (3)	4.1 (3)	-6.87 (3)	-7.22*	Drew et al. (2013): Refer to as a dacitic tuff with abundant pumice and lithic fragments
Picabo	West Pocatello Rhyolite	?	North end of Bannock Mts; Borehole INEL-1(?)	-	8.25±0.26 (3)	3.3 (3)	-5.5 (3)	-6.5(3)	Drew et al. (2013): 25% phenocrysts, densely welded ignimbrite This study: 20-25% phenocrysts of plag >> cpx > opq. Cannot differentiate between ignimbrite and lava flow.
Picabo	INEL-1 3686'	Ignimbrite	Borehole INEL-1	-	8.27 ± 0.27 (6) 8.31±0.22	2.1 (3)	-5.5*	-6.2 (3)	McCurry and Rodgers (2009): 9% phenocrysts of plag >> pyx = mt > qtz >> zirc = ap
Picabo	INEL-1 4860	Ignimbrite	Borehole INEL-1	-	8.04 ± 0.1 Ma (6)	-	-6.4*	-6.9(6)	McCurry and Rodgers (2009): 23% phenocrysts of san > qtz > pyx > mt >> zirc = ap
Picabo	INEL-1 10,365'	Ignimbrite	Borehole INEL-1	-	8.35±0.24 (6)	-	-7.0*	-7.3(6)	McCurry and Rodgers (2009): 26% phenocrysts of plag >> pyx > mt = qtz >> ilm = zirc = ap
Heise (?)	Tuff of Lost River Sinks	Ignimbrite	Sothern end of Lemhi Mts	8.81 ± 0.16 (7)	7.05 ± 0.13 (3)	6.8 (3)	-10.3 (3)	-11.8 (3)	Drew et al. (2013): Indicate that this tuff displays striking similarites to the Blacktail Creek Tuff, with similar major and trace element geochemistry, U-Pb zircon ages, and stable and radiometric isotope analysis. Consider this tuff to be a precursor to the Blacktail Creek Tuff

Data compilation of Heise and Picabo-age Snake River-type rhyolites . Stars indicate ϵHf values calculated from ϵNd values (and vice versa) using the "Terrestrial Array" equation provided by Vervoort et al. (1999). (1) = Anders et al. (2014); (2) = Watts et al. (2011); (3) Drew et al. (2013); (4) = Bindeman et al. (2007); (5) Morgan and McIntosh (2005); (6) = McCurry and Rodgers (2009); (7) = Anders et al. (2009).

Table 4.1 continued

Unit	Rhyolite of Butte Quarry	Rhyolite of USGS-142	Kilgore Tuff (1)	Conant Creek Tuff (1)	Wolverine Creek Tuff (1)	Lidy Hot Springs Rhyolite (1)	Rhyolite lava of WO-2 (2)	Walcott tuff B (2)	Rhyolite lava of lower WO-2 (2)	Walcott Tuff undivided (1)
<i>Major element analyses by XRF (wt %)</i>										
SiO₂	74.98	75.65	76.19	74.26	75.81	76.67	75.75	76.79	77.83	75.49
TiO₂	0.40	0.25	0.23	0.21	0.21	0.3	0.42	0.27	0.24	0.224
Al₂O₃	12.20	12.80	12.35	14.17	12.6	12.31	12.41	12.39	11.77	12.03
FeO	2.38	1.66	1.71	2.07	1.65	1.17	1.72	1.42	1.3	1.27
MnO	0.07	0.05	0.03	0.04	0.04	0.04	0.05	0.02	0.04	0.03
MgO	0.30	0.26	0.11	0.74	0.33	0.13	0.28	0.4	0.21	0.28
CaO	1.47	0.71	0.57	1.06	0.87	0.58	0.88	0.52	0.53	2.11
Na₂O	3.04	3.31	3.44	2.08	3.28	3.4	3.53	3.13	3.28	3.45
K₂O	5.08	5.27	5.33	5.36	5.2	5.38	4.89	5.04	4.78	5.09
P₂O₅	0.07	0.04	0.03	0.02	0.04	0.02	0.05	0.03	0.03	0.03
	100.00	100.00	100.00	100.01	100.03	100.00	99.98	100.01	100.01	100.01
<i>Trace element analyses by XRF (ppm)</i>										
Trace										
Ba	1109.7	1057.9	889.80	509	573	840	1069	1015	643	914
Ce	168.5	162.1	156.40	159	154	126				136
Cl	79	92								
Cr	0.7	2.2	2.83	5	8	1				2
Cu	5.3	4.4	6.50	4	5	0				5
F	328	385								
Ga	17.8	21	19.67	22	22	17				17
La	87	92.5	85.80	81	78	67				71
Nb	49.9	50.3	47.83	56	54	41				41
Nd	73.1	70.6	62.17	65	61	48				54
Ni	2.4	4.4	3.17	2	5	0				3
Pb	27.6	31.8	25.33	26	28	25				23
Rb	165.7	204	176.60	147	165	181				171
S	1472	n.d.								
Sc	5.9	2.2	4.17	3	2	3				3
Sm	11.8	12.2								
Sr	74.3	47.1	27.40	25	40	29	65	40	34	39
Th	29.9	32.5	26.60	26	25	28				26
U	8.1	7.4	6.60	5	6	9				7
V	9.1	8.4	5.17	2	9	2				24
Y	71.6	68.6	55.00	77	75					54
Zn	68.7	91.5	64.67	90	86	45				41
Zr	584.5	300.1	320.40	273	185	239	399	258	259	221

Table 4.2: Data compilation of whole rock geochemistry of Heise and Picabo-age Snake River-type rhyolites. Fe is expressed as FeO for all analyses. (1) = Watts et al. (2011); (2) = McCurry and Rodgers (2009); (3) = Drew et al. (2013).

Table 4.2: Data compilation of Snake River-type rhyolite whole rock geochemistry												
Unit	Rhyolite of Butte Quarry	Rhyolite of USGS-142	Blacktail Creek Tuff of WO-2 (2)	Blacktail Creek Tuff (1)	Rhyolite of Steven's Peak (3)	Rhyolite of Steven's Peak 2 (3)	West Pocatello rhyolite (3)	INEL-1 3686' (2)	INEL-1 4860' (2)	INEL-1 10365' (2)	Tuff of Lost River Sinks (3)	Tuff of American Falls (3)
<i>Major element analyses by XRF (wt %)</i>												
SiO ₂	74.98	75.65	77.47	74.4	76.35	74.74	74.16	73.16	76.99	72.08	75.18	67.73
TiO ₂	0.40	0.25	0.24	0.31	0.24	0.53	0.42	0.48	0.26	0.65	0.29	0.82
Al ₂ O ₃	12.20	12.80	12.32	13.14	12.34	12.35	12.77	12.9	12.13	12.69	12.96	15.47
FeO	2.38	1.66	1.44	1.95	1.36	1.83	2.57	2.93	1.84	3.86	1.84	4.77
MnO	0.07	0.05	0.02	0.05	0.04	0.08	0.05	0.14	0.04	0.07	0.03	0.08
MgO	0.30	0.26	0.32	0.31	0.21	0.31	0.2	0.84	0.44	0.52	0.33	0.63
CaO	1.47	0.71	0.49	1.22	0.76	1.78	1.28	3.46	0.74	2.17	0.98	2.46
Na ₂ O	3.04	3.31	2.50	3.3	3.04	3.71	2.95	1.9	1.85	3.12	2.67	3.61
K ₂ O	5.08	5.27	5.17	5.27	5.61	4.6	5.55	4.13	5.66	4.69	5.67	4.26
P ₂ O ₅	0.07	0.04	0.03	0.04	0.05	0.07	0.06	0.07	0.05	0.16	0.04	0.17
	100.00	100.00	100.00	99.99	100.00	100.00	100.01	100.01	100.00	100.01	99.99	100.00
<i>Trace element analyses by XRF (ppm)</i>												
Trace												
Ba	1109.7	1057.9	607	1099	888.2	1044	1085.6	1090	970	963	837.5	1869.6
Ce	168.5	162.1		120	132.4	132.9	143.4				119.5	125.2
Cl	79	92										
Cr	0.7	2.2		2	4.2	4	3.9				5.6	11.4
Cu	5.3	4.4		1	2.5	1.8	2.7				2.2	9.9
F	328	385										
Ga	17.8	21		18	16.7	18.1	18.9				16.8	21
La	87	92.5		66	67.9	69.9	74.6				63.8	67.2
Nb	49.9	50.3		32	43.4	44.3	46.2				35.3	40
Nd	73.1	70.6		45	53	57.2	59.2	79	71	55	44.3	54.6
Ni	2.4	4.4		4	1.6	1.6	4.6				4.8	6.8
Pb	27.6	31.8		26	26.9	31	25.3				28.7	23
Rb	165.7	204		174	167	149.1	165.4	129	216	171	176.7	114.2
S	1472	n.d.										
Sc	5.9	2.2		5	2.8	5.6	4.1				2.5	7.4
Sm	11.8	12.2							14	11		
Sr	74.3	47.1	38	84	27.3	95.2	87.2	118	70	128	69	174.5
Th	29.9	32.5		27	27	24.2	25.6	32.3	29.9	27.4	29.4	18.4
U	8.1	7.4		7	8.3	6.5	8.1	5.3	6.9	6.5	8	6.1
V	9.1	8.4		9	8.5	8.1	7.5				6.8	32.1
Y	71.6	68.6		44	57.6	65.6	62.4				49.9	54.7
Zn	68.7	91.5		61	56.8	75.7	66.4				57.8	84.4
Zr	584.5	300.1	226	327	234.7	510.4	523	523	420	539	299.6	719.8

Table 4.2 continued: Fe is expressed as FeO for all analyses. (1) = Watts et al. (2011); (2) = McCurry and Rodgers (2009); (3) = Drew et al. (2013).

4.1.1 Rhyolite of USGS-142

The rhyolite of USGS-142 produced an average U-Pb zircon age of 6.25 ± 0.7 Ma ($n = 17$), suggesting that initial crystallization of this ignimbrite occurred during Heise-aged volcanism. Measured Lu-Hf radiogenic isotope analyses of selected zircon phenocrysts produced an average initial ϵ_{Hf} value of -8.5 ± 0.9 ($n = 11$), which is consistent with values previously measured for other Heise-aged rhyolites such as the Walcott Tuff B found in borehole WO-2 (Table 4.1; McCurry and Rodgers, 2009).

In addition, $\delta^{18}\text{O}$ melt values calculated from pyroxene phenocryst analyses produced values of $+4.7\text{‰}$ to $+5.0\text{‰}$ (Table 4.1). Following the interpretation of Bindeman et al. (2007), who documented a progressive decrease in $\delta^{18}\text{O}$ melt values with younger Heise-aged rhyolites, the values calculated for the rhyolite of USGS-142 suggest that this ignimbrite was emplaced after the first major Heise-aged eruption of the Blacktail Creek Tuff (calculated $\delta^{18}\text{O}$ melt value of $+6.6\text{‰}$; Watts et al., 2011), but before the last major Heise-aged eruption of the Kilgore Tuff (calculated $\delta^{18}\text{O}$ melt value of $+3.3\text{‰}$; Watts et al., 2011). This interpretation is further supported by a younger mean average U-Pb zircon age of the rhyolite of USGS-142 than the Blacktail Creek Tuff (6.92 ± 0.28 Ma; Bindeman et al., 2007), and an older age than the Kilgore Tuff (4.59 ± 0.26 Ma; Bindeman et al., 2007).

The major element geochemistry of the rhyolite of USGS-142 is consistent with an analysis conducted on the Walcott Tuff B found in borehole WO-2 (Table 4.2; McCurry and Rodgers, 2009). However, the Walcott Tuff B produced higher values of SiO_2 and MgO (76.79% and 0.4%, respectively) compared to the rhyolite of USGS-142 (75.65% and 0.26%, respectively). The higher value of MgO for the Walcott Tuff B suggests that this ignimbrite represents a less petrogenetically evolved rhyolite; less-evolved rhyolites

should display high values for TiO₂, MgO, and CaO. However, the analyses conducted on the Walcott Tuff B do not display high values of TiO₂ or CaO. Rather, these values are consistent with the values measured for the rhyolite of USGS-142 (Table 4.2). Therefore, the differences in MgO between the Walcott Tuff B and the rhyolite of USGS-142 can be attributed to analytical error during XRF analyses. The values for Ba, Sr, and Zr measured for the rhyolite of USGS-142 are consistent with values measured for the Walcott Tuff B (Table 4.2; McCurry et al., 2009).

The major element geochemistry of the rhyolite of USGS-142 is also consistent with an analysis conducted on the rhyolite of Steven's Peak (Fig. 3.6 and Table 4.2; Drew et al., 2013). However, Drew et al. (2013) reported a U-Pb zircon age of 6.62 ± 0.12 (Table 4.1), which is slightly older than the rhyolite of USGS-142; furthermore, the rhyolite of Steven's Peak is only known to be found along the southern margin of the ESRP. In addition, the major element geochemistry of the rhyolite of USGS-142 is consistent with an analysis conducted for the Tuff of Wolverine Creek (Fig. 3.6 and Table 4.2; Watts et al., 2011). However, Bindeman et al. (2007) reported a U-Pb zircon age of 5.45 ± 0.14 Ma, which is statistically distinguishable from the rhyolite of USGS-142.

Thin section analyses of the rhyolite of USGS-142 indicate that plagioclase dominates as a crystal phase; pyroxene, opaque phenocrysts, sanidine, and quartz (in order of abundance) are less common. However, McCurry and Rodgers (2009) indicated a higher proportion of sanidine to plagioclase in the Walcott Tuff B in borehole WO-2, and a higher volume percentage of phenocrysts compared to the rhyolite of USGS-142 (10% versus 3.7%, respectively). Anders et al. (2014) indicated 1 to 2% of phenocrysts dominated by feldspars, which is more consistent with thin section analyses conducted for this research.

Therefore, crystal phase modes for the rhyolite of USGS-142 are slightly different than those of the Walcott Tuff B (McCurry and Rodgers, 2009), but are comparable to the description from Anders et al. (2014) in that both ignimbrites contain plagioclase, sanidine, and pyroxene.

Lastly, the rhyolite of USGS-142 produced an Ar-Ar eruption age of 6.39 ± 0.13 Ma, suggesting that this ignimbrite was emplaced during the early stages of Heise-aged volcanism, but after the Blacktail Creek Tuff (6.66 ± 0.01 Ma; Anders et al., 2014). This eruption age is consistent with the Walcott Tuff B found in borehole WO-2 (6.27 ± 0.01 Ma; Anders et al., 2014).

Thus, U-Pb zircon ages, Lu-Hf isotope analyses, major and trace element geochemistry, and Ar-Ar ages for the rhyolite of USGS-142 are consistent with a correlation to the Walcott Tuff B (Table 4.3). Although calculated $\delta^{18}\text{O}$ melt values for the rhyolite of USGS-142 are over 1‰ lower than the Walcott Tuff (Table 4.1; Fig. 3.5; Bindeman et al., 2007; Watts et al., 2011), Watts et al. (2011) did not differentiate between the Walcott Tuff A and B (e.g. Anders et al., 2014) for $\delta^{18}\text{O}$ stable isotope analysis. The values calculated for the Walcott Tuff may represent values for the Walcott Tuff A, and the later eruption, Walcott Tuff B (Anders et al., 2014), may have produced lower $\delta^{18}\text{O}$ melt values.

Table 4.3: Correlation matrix for the rhyolite of USGS-142

		major elem	trace elem	petrography	Ar/Ar age	Zircon age	εHf	δ18O
Rhyolite of USGS-142	Walcott Tuff B	2	3	2	3	na	3	na
Rhyolite of USGS-142	Walcott Tuff A	na	na	1	3	na	na	na
Rhyolite of USGS-142	Walcott Tuff undivided	1	2	2	3	3	3	2
Rhyolite of USGS-142	Kilgore Tuff	2	2	2	0	0	3	1
Rhyolite of USGS-142	Blacktail Creek Tuff	1	2	1	1	1	3	1
Rhyolite of USGS-142	Tuff of Wolverine Creek	2	1	1	0	0	3	1
Rhyolite of USGS-142	Tuff of Conant Creek	1	1	2	1	1	3	2
Rhyolite of USGS-142	Rhyolite of Upper WO-2	2	2	1	2	na	na	na
Rhyolite of USGS-142	Tuff of WO-2	na	na	2	2	na	na	na
Rhyolite of USGS-142	Lidy Hot Springs Rhyolite	2	1	1	2	na	na	3
Rhyolite of USGS-142	Rhyolite of Lower WO-2	2	1	1	3	na	na	na
Rhyolite of USGS-142	Rhyolite of Steven's Peak	3	1	2	na	1	2	2
Rhyolite of USGS-142	Rhyolite of Steven's Peak 2	1	2	2	na	1	2	3

Table 4.3: Correlation matrix comparing the rhyolite of USGS-142 to known Heise-aged rhyolites. Numbers correspond to a qualitative assessment score: 3 = excellent correlation, 2 = plausible correlation, but some anomalies or limited data, 1 = doubtful correlation, 0 = clearly not correlative. Based on this qualitative assessment, the rhyolite of USGS-142 is tentatively correlated to the Walcott Tuff B. See text for discussion.

4.1.2 Rhyolite of Butte Quarry

The rhyolite of Butte Quarry produced an average U-Pb zircon age of 8.13 ± 0.7 Ma ($n = 24$), suggesting that initial crystallization of this ignimbrite occurred during Picabo-aged volcanism (e.g. Drew et al., 2013). Measured Lu-Hf radiogenic isotope analyses on selected zircon phenocrysts produced an average initial εHf value of -5.3 ± 0.9 ($n = 14$), which is consistent with values previously measured for other Picabo-aged rhyolites, such as the West Pocatello rhyolite (Drew et al., 2013), and the upper-most Picabo-aged ignimbrites found in borehole INEL-1 (Table 4.1; hereby referred to as “INEL-1 3686”; McCurry and Rodgers, 2009).

In addition, δ¹⁸O melt values calculated from quartz and plagioclase phenocrysts analyses produced values of +2.4‰ to +4.2‰ (average of 3.2‰). Following the interpretation of Drew et al. (2013), who documented a depletion in δ¹⁸O melt values with progressively younger Picabo-aged rhyolites, these values suggest the rhyolite of Butte

Quarry was deposited after the first major Picabo-aged eruption of the Arbon Valley Tuff (calculated $\delta^{18}\text{O}$ melt value of +8.3‰; Drew et al., 2013), and before the first major Heise-aged eruption of the Blacktail Creek Tuff. This interpretation is further supported because the rhyolite of Butte Quarry produced a younger mean average U-Pb zircon age than the Arbon Valley Tuff (10.44 ± 0.27 Ma; Drew et al., 2013), and an older age than the Blacktail Creek Tuff (6.92 ± 0.28 Ma; Bindeman et al., 2007).

Major and trace element geochemistry analyzed for the rhyolite of Butte Quarry is consistent with an analysis conducted on the West Pocatello rhyolite (Fig. 3.7; Table 4.1). Conversely, major element geochemistry conducted at three intervals for Picabo-aged ignimbrites in borehole INEL-1 (3686', 4860', and 10365') are not consistent with analyses conducted on the rhyolite of Butte Quarry, although values for TiO_2 and Al_2O_3 for INEL-1 3686' (0.48% and 12.9%, respectively) are consistent with the rhyolite of Butte Quarry (0.40% and 12.20%, respectively; Table 4.4).

The rhyolite of Butte Quarry produced values for Ba, Nd, Th, and Zr that are consistent with INEL-1 3686' (Table 4.1), yet the rhyolite of Butte Quarry produced a lower Sr value compared with INEL-1 3686' (74.3 ppm versus 118 ppm, respectively; Table 4.1). Values for Nd, Sr, and Th for the rhyolite of Butte Quarry are consistent with INEL-1 4860', but Ba and Zr are not consistent (Table 4.1). Values for Th and Zr for the rhyolite of Butte Quarry are consistent with INEL-1 10365', but Ba, Nd, and Sr are not consistent. In conclusion, major and trace element geochemistry measured for the rhyolite of Butte Quarry is not consistent with analyses conducted at three intervals for Picabo-aged ignimbrites in borehole INEL-1.

Thin section analyses of the rhyolite of Butte Quarry indicate that plagioclase dominates as a crystal phase, whereas pyroxene, opaque phenocrysts, quartz, and sanidine (in order of abundance) are less common. Thin section observations indicate some similarities with INEL-1 3686', described by McCurry and Rodgers (2009) (Table 4.1), although INEL-1 3686' contains a higher volume percentage of phenocrysts (9%) than the rhyolite of Butte Quarry (3%). INEL-1 4860' contains only sanidine, quartz, pyroxene, and opaque phenocrysts, and a much higher volume percentage of phenocrysts of 23% (McCurry and Rodgers, 2009), so this interval is likely not correlative to the rhyolite of Butte Quarry. INEL-1 10365' contains plagioclase, pyroxene, opaque phenocrysts, and quartz (26% volume percentage of phenocrysts; McCurry and Rodgers, 2009); the lack of sanidine phenocrysts and the significantly higher proportion of phenocrysts suggests that this interval is not correlative to the rhyolite of Butte Quarry. Therefore, crystal phase modes for the rhyolite of Butte Quarry are relatively consistent with INEL-1 3686'.

Thus, U-Pb zircon ages, Lu-Hf isotope analyses, and calculated $\delta^{18}\text{O}$ melt values for the rhyolite of Butte Quarry are consistent with a correlation to INEL-1 3686' (Table 4.4). The major and trace element geochemistry of the rhyolite of Butte Quarry is not consistent with any of the analyses conducted for the Picabo-aged ignimbrite of borehole INEL-1, although trace element geochemistry (aside from Sr) is consistent with INEL-1 3686'. Average ϵ_{Hf} values and thin section petrography of INEL-1 3686' are most consistent with the rhyolite of Butte Quarry compared to the lower Picabo-aged ignimbrites in borehole INEL-1.

Given that U-Pb zircon ages, Lu-Hf isotope analyses, calculated $\delta^{18}\text{O}$ melt values, phenocryst textures (type 2 glomerocryst), and major and trace element geochemistry

between the rhyolite of Butte Quarry and the West Pocatello rhyolite are consistent, these separate rhyolites may also be correlative (Table 4.4). However, thin sections created for the West Pocatello rhyolite do not contain textures that would suggest a pyroclastic origin for this rhyolite, and phenocryst compositions between the rhyolite of Butte Quarry and West Pocatello rhyolite are not consistent (e.g. West Pocatello rhyolite did not contain orthopyroxene). Also, the West Pocatello rhyolite contains significantly more phenocrysts per volume (~20%) compared to the rhyolite of Butte Quarry (~2-3%). Further research must be conducted on the West Pocatello rhyolite to provide a plausible correlation with the rhyolite of Butte Quarry.

Table 4.4: Correlation matrix for the rhyolite of Butte Quarry

		major elem	trace elem	petrography	Ar/Ar age	Zircon age	εHf	d18O
Rhyolite of Butte Quarry	West Pocatello rhyolite	3	3	1	na	3	3	3
Rhyolite of Butte Quarry	INEL-1 3686'	2	2	3	na	3	3	3
Rhyolite of Butte Quarry	INEL-1 4860'	2	2	1	na	3	2	na
Rhyolite of Butte Quarry	INEL-1 10365'	2	2	2	na	3	2	na
Rhyolite of Butte Quarry	Tuff of Lost River Sinks	2	1	na	na	0	1	1
Rhyolite of Butte Quarry	Tuff of American Falls	1	1	na	na	2	2	3

Table 4.4: Correlation matrix comparing the rhyolite of Butte Quarry to Picabo-aged rhyolites. Numbers correspond to a qualitative assessment score: 3 = excellent correlation, 2 = plausible correlation, but some anomalies or limited data, 1 = doubtful correlation, 0 = clearly not correlative. See text for discussion.

4.1.3 Rhyolite of the East Side of the Arco Hills

The rhyolite of the east side of the Arco Hills produced an Ar-Ar eruption age of 6.63 ± 0.05 , suggesting that it was emplaced during the earliest stages of Heise-aged volcanism. This eruption age is consistent with that of the Blacktail Creek Tuff (6.66 ± 0.01 Ma).

A $\delta^{18}\text{O}$ melt value of 6.1‰ was calculated from an analysis conducted on a pyroxene phenocryst in the rhyolite of the east side of the Arco Hills. This calculated $\delta^{18}\text{O}$ melt value is consistent with values reported for the Blacktail Creek Tuff by Bindeman et al. (2007), and slightly lower for values reported by Watts et al. (2011) (Table 4.1). Also, the $\delta^{18}\text{O}$

value is consistent with the Tuff of Conant Creek, rhyolite of Steven’s Peak and the Walcott Tuff; however, given the Ar-Ar eruption age of the rhyolite of the east side of the Arco Hills these potential correlatives can be discarded.

Thin section analyses for the lower vitrophyre of the rhyolite of the east side of the Arco Hills indicate that this portion of the ignimbrite is nearly aphyric (~1%). However, field observations of the overlying microcrystalline center zone suggest that this portion of the ignimbrite contains significantly more phenocrysts (~5-10%) than recorded in the lower vitrophyre, both of which are dominated by feldspar.

Thus, Ar-Ar age dates and $\delta^{18}\text{O}$ melt values of the rhyolite of the east side of the Arco Hills are consistent with a correlation to the Blacktail Creek Tuff. Although the lower vitrophyre of the rhyolite of the east side of the Arco Hills has an enigmatic low percentage of phenocrysts compared to stratigraphic sections described by Morgan and McIntosh (2005), the overlying microcrystalline center zone displays a volume percentage of phenocrysts that is more consistent with the Blacktail Creek Tuff.

Table 4.5: Correlation matrix for the rhyolite of the east side of the Arco Hills

		major elem	trace elem	petrography	Ar/Ar age	Zircon age	ϵHf	$\delta^{18}\text{O}$
East side of Arco Hills	Blacktail Creek Tuff	na	na	2	3	na	na	3
East side of Arco Hills	Walcott Tuff A	na	na	2	1	na	na	na
East side of Arco Hills	Walcott Tuff B	na	na	2	1	na	na	na
East side of Arco Hills	Walcott Tuff	na	na	2	1	na	na	3
East side of Arco Hills	Kilgore Tuff	na	na	2	0	na	na	0
East side of Arco Hills	Tuff of Wolverine Creek	na	na	1	1	na	na	3
East side of Arco Hills	Tuff of Conant Creek	na	na	2	1	na	na	3
East side of Arco Hills	Rhyolite of Upper WO-2	na	na	1	1	na	na	na
East side of Arco Hills	Tuff of WO-2	na	na	2	1	na	na	na
East side of Arco Hills	Lidy Hot Springs Rhyolite	na	na	2	1	na	na	0
East side of Arco Hills	Rhyolite of Lower WO-2	na	na	1	2	na	na	na
East side of Arco Hills	Rhyolite of USGS-142	na	na	2	1	na	na	2
East side of Arco Hills	Rhyolite of Steven’s Peak	na	na	1	na	na	na	3
East side of Arco Hills	Rhyolite of Steven’s Peak 2	na	na	1	na	na	na	2

Table 4.5: Correlation matrix comparing the rhyolite of the east side of the Arco Hills to ESRP rhyolites. Numbers correspond to a qualitative assessment score: 3 = excellent correlation, 2 = plausible correlation, but some anomalies or limited data, 1 = doubtful correlation, 0 = clearly not correlative. See text for discussion.

4.2 Kinematic Analysis of Northeast-Striking Faults

Aforementioned, northeast-striking faults that roughly parallel the ESRP are located within 20-30 km of the margins of the ESRP within what is termed the collapse shadow of the seismic parabola (Anders et al., 1989; Zentner, 1989; Rodgers et al., 2002). The northeast-striking faults of the Arco Hills have an average strike of 046° ($n = 50$), slightly north of the trend of the ESRP (052° ; McQuarrie and Rodgers, 1998), suggesting that the northeast-striking faults are related to the development of the ESRP. Furthermore, the poles to the northeast-striking faults form a tight cluster ($K = 9.38$), which suggests these faults have consistent strikes. Figure 3.13 displays a map with measured northeast-striking faults in the Arco Hills, where their strikes are relatively parallel to the ESRP.

The collective kinematic analysis of 50 northeast-striking faults in the Arco Hills demonstrate that the northeast-striking faults accommodated extension northwest to southeast in a nearly exclusively dip-slip sense (Fig. 3.12).

The fault plane solutions produced from FaultKin (Allmendinger et al., 2012) show evidence that the northeast-striking faults accommodated extension differently in the distal and proximal fault domains, where the proximal fault plane solution appears to be “rotated” relative to the distal fault plane solution (Figs. 3.14 and 3.15). Furthermore, mean vector analyses of poles to fault planes demonstrate that northwest-dipping faults dip more shallowly toward the ESRP, whereas southeast-dipping faults steepen toward the ESRP (Table 3.6). Therefore, the northeast-striking faults are interpreted to have been rotated, which is likely a result of flexure outboard of a subsiding ESRP. The estimated magnitude of rotation of shortening axes is $\sim 4.1^{\circ}$ about an axis parallel to the trend of the ESRP (052° ; McQuarrie and Rodgers, 1998), suggesting that the faults rotated slightly less than the

measured plunge of Mesozoic fold-hinges, where the Mesozoic fold-hinges have rotated $\sim 5^{\circ}$ - 10° southeast of the 20° fold-plunge contour.

Collectively, shortening and extension axes form a girdled distribution ($K = 0.81$, 0.87 respectively; Table 3.5). Shortening and extension axes in the distal fault domain form clustered distributions, yet in the proximal fault domain they form girdled distributions (Table 3.8). The collective analysis likely reflects that new northeast-striking faults formed as older faults were rotated; thus, older northeast-striking faults would be rotated more than newly formed ones, producing a girdled, rather than clustered distribution.

Given that the northeast-striking faults of the Arco Hills form a tight clustered distribution, have an average strike comparable to previous research on these northeast-striking faults both north and south of the ESRP (e.g. Allmendinger, 1982; Zentner, 1989), and do not show any significant along-strike curvature throughout the field area (Fig. 3.13), these faults are likely not related to caldera subsidence.

In addition, fault plane solutions demonstrate that the northeast-striking faults accommodated extension in a nearly exclusively dip-slip sense (Figs. 3.12, 3.14, and 3.15), so they are not a result of right-lateral slip due to differential extension between the Basin and Range and ESRP (e.g. Payne et al., 2012). Although the northeast-striking faults of the Arco Hills display no evidence for right-lateral oblique slip accommodation, dextral shear between the northern Basin and Range and the ESRP may have been accommodated along distinct segment boundaries of the Lost River fault north of this study area, rather than throughout the entire northern Basin and Range.

Northwest-striking faults are well known to accommodate Basin and Range extension, and the strain as recorded by northwest-striking Basin and Range faults and

northeast-striking faults are not compatible. Therefore, the northeast-striking faults are likely not a result of an along-strike decrease in slip of Basin and Range faults as they approach the ESRP (cf. Bruhn et al., 1992).

The northeast-striking faults in the Arco Hills dip both toward and away from the ESRP and show evidence for being rotated similarly to Mesozoic fold-hinges (McQuarrie and Rodgers, 1998), where shortening axes collectively demonstrate a girdled distribution and the mean vector of shortening axes shallow toward the ESRP. Therefore, the northeast-striking faults likely formed as a result of crustal flexure outboard of a subsiding ESRP.

Anderson's theory of faulting suggests that faults and fractures should form $\sim 30^\circ$ from the maximum principal stress (σ_1) (Anderson, 1951). Given that the northeast-striking faults accommodated extension in a nearly exclusively dip-slip sense, σ_1 should have been near-vertical during brittle deformation, and the northeast-striking faults should have formed with $\sim 60^\circ$ dips (relative to horizontal) toward and away from the ESRP prior to rotation. However, the majority of faults dip $\geq 70^\circ$, suggesting that (prior to rotation) the northeast-striking faults formed at steeper dips than is suggested by Anderson (1951). The northeast-striking faults may have originally formed as high-angle hybrid faults in a transitional tensile-compressive stress regime; alternatively fractures may have initially formed as mode 1 extension fractures under tension, and were later reactivated as mode 2 fractures (faults). This may have been followed by further rotation with the onset of flexure outboard of the subsidence of the ESRP.

Furthermore, the shortening and extension axes shown in the fault plane solutions are widely dispersed rather than forming a tight cluster. This is likely a result of 1) rotation of fault planes after faulting ceased and 2) the steeply-dipping nature of these faults.

Regardless, the northeast-striking faults in the Arco Hills did not accommodate right-lateral oblique extension, and were likely rotated as discussed above.

4.3 Geometry of the Western Boundary of the ESRP near the Arco Hills

The tentative correlations for the rhyolites of USGS-142 and Butte Quarry are used to determine the continuity and geometry of subsurface ignimbrites in the western INL near the Arco Hills, which directly reflects whether a fault is required to have accommodated subsidence of the ESRP relative to the Arco Hills.

Given that the rhyolite of USGS-142 is tentatively correlated to the Walcott Tuff B in borehole WO-2, the upper contact of the rhyolite of USGS-142 was projected through the subsurface of the ESRP to borehole WO-2 (Fig. 4.1). The top of the rhyolite of USGS-142 is found at an elevation of 1097 m (relative to mean sea level; Twining et al., 2017). The top of Walcott Tuff B is found at an elevation of 235 m (relative to mean sea level; Anders et al., 2014). The extrapolations between these two ignimbrites defines a gently southeast-dipping surface, which projects through borehole INEL-1 (Fig. 4.1).

The rhyolite of the east side of the Arco Hills is tentatively correlated to the Blacktail Creek Tuff, which was also encountered near the base of borehole WO-2. The rhyolite of the east side of the Arco Hills is found at an elevation of 1600 m (relative to mean sea level), whereas the Blacktail Creek Tuff in borehole WO-2 is found at an elevation of six meters below mean sea level. The projection of this unit also defines a gently south-east dipping surface, which projects through borehole INEL-1. Furthermore, borehole USGS-142 did not encounter the Blacktail Creek Tuff, so its projection must occur just below the base of borehole USGS-142.

In addition, the rhyolite of Butte Quarry is tentatively correlated to the upper-most Picabo-aged ignimbrite found in borehole INEL-1 (INEL-1 3686') at an elevation of 362 m (relative to mean sea level; McCurry and Rodgers, 2009). If the 20° dip of the rhyolite of Butte Quarry is constant through the subsurface of the ESRP, then the base of this contact would project below the base of borehole INEL-1. However, based on U-Pb zircon ages, stable and radiometric isotope analyses, and thin section petrography the rhyolite of Butte Quarry is tentatively correlated to INEL-1 3686'. Therefore, the projection of the base of the rhyolite of Butte Quarry to INEL-1 3686' defines a gently southeast-dipping surface (Fig. 4.1), where the surficial dip of the rhyolite of Butte Quarry shallows toward borehole INEL-1 and the steeper dip of the rhyolite of Butte Quarry is confined near the margin between the ESRP and the Arco Hills. The 20° south dip of the exposure of the rhyolite of Butte Quarry must shallow as the projection of this rhyolite approaches borehole INEL-1, suggesting that the dips of subsurface Snake River-type rhyolites are steeper along the margin of the ESRP, and are shallower in the center of the ESRP.

McBroome et al. (1981) interpreted that rhyolite sampled at ~770 m below land surface in borehole INEL-1 was correlative to the Kilgore Tuff. Furthermore, a fission-track age of 4.2 ± 0.3 Ma, which is roughly consistent with the Kilgore Tuff, supported this interpretation (Morgan et al., 1984). Furthermore, Anders et al. (2014) documented approximately 122 m of Snake River-type rhyolite overlies the Walcott Tuff B in borehole WO-2. Therefore, younger Snake River-type rhyolites that overly the Walcott Tuff B in borehole WO-2 must pinch out toward the northwest closer to the Arco Hills before borehole USGS-142, or were eroded away before basalt volcanism could conceal the ~122 m of rhyolite.

4.3.1 Subsurface Architecture of the ESRP

Based upon the correlations of the studied rhyolites, a cross section from the Arco Hills through deep boreholes USGS-142, INEL-1, and WO-2 was created to interpret the architecture of subsurface rhyolites in the west-central INL (Fig. 4.1). The base exposure of the rhyolite of Butte Quarry was projected east-northeast around the Arco Hills from its surficial exposure south of the Arco Hills (Fig. 2.7), attempting to keep the map distance from the 20° fold-plunge contour of McQuarrie and Rodgers (1998) constant. However, borehole USGS-142 and the exposure of the rhyolite of Butte Quarry are found at the same distance from the 20° fold-plunge contour, and the rhyolite of Butte Quarry was not encountered in borehole USGS-142. Therefore, the Mesozoic fold-plunge contours near borehole USGS-142 must be closely spaced in the subsurface of the ESRP, which would imply a zone of localized subsidence in this area. This may suggest that the ESRP did not subside uniformly relative to the northern Basin and Range, which is a similar conclusion to McQuarrie and Rodgers (1998).

The correlations of the Walcott Tuff B between borehole USGS-142 and borehole WO-2, the rhyolite of Butte Quarry to borehole INEL-1, and the rhyolite of the east side of the Arco Hills to the Blacktail Creek Tuff in borehole WO-2 demonstrate that subsurface Snake River-type rhyolites are at a structurally higher elevation at the margin between the ESRP near the Arco Hills compared to the center of the ESRP. Furthermore, the dips of subsurface rhyolites are steep near the margin of the ESRP, and shallow toward the center of the ESRP. This observation suggests that flexure is confined to the margin of the ESRP and the northern Basin and Range. In addition, this also suggests that tilting of subsurface

rhyolites does not exceed the maximum plunge of Mesozoic fold-hinges of McQuarrie and Rodgers (1998).

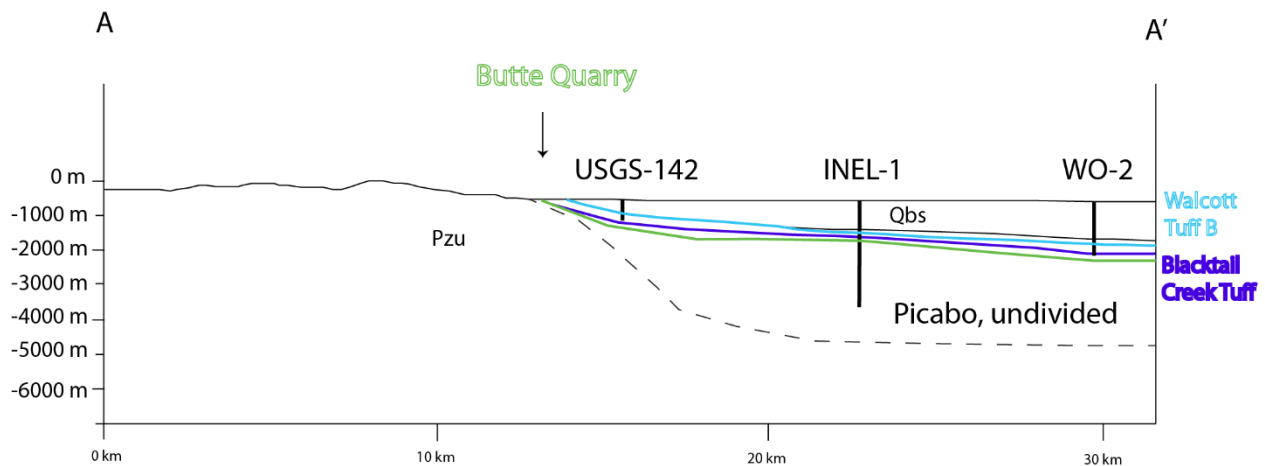


Figure 4.1: Cross section A-A' through deep boreholes USGS-142, INEL-1, and WO-2. Based on the correlations of the studied rhyolites, subsurface Snake River-type rhyolites are found at a structurally higher elevation at the margin of the ESRP near the Arco Hills. Furthermore, the dips of subsurface rhyolites are more shallow toward the center of the ESRP.

The rhyolite of Butte Quarry is found between the 20 and 25° fold-plunge contours of McQuarrie and Rodgers (1998), suggesting that this rhyolite was tilted similarly to the Mesozoic fold-hinges north of the ESRP. The structural relief between the outcrop of Butte Quarry and borehole INEL-1 can be attributed to the regional subsidence of the ESRP, rather than a significant normal fault down dropping the ESRP relative to the northern Basin and Range. Therefore, all structural relief calculated for rhyolites emplaced after the rhyolite of Butte Quarry can be attributed to regional subsidence of the ESRP (see below). Furthermore, no significant fault was active post emplacement of the Walcott Tuff B.

4.4 Implications for the Hydrogeology of the Western Idaho National Laboratory

At the margin of the ESRP near the Arco Hills, the base of the ESRP aquifer is likely confined by the contact between subsurface rhyolites and overlying basalts and sediments. Furthermore, the rhyolite of USGS-142 is denser than the overlying basalt based on the

thickness of the unit and neutron logs that indicated a lower permeability in the rhyolite of USGS-142 (Twining et al., 2017), so subsurface Snake River-type rhyolites are likely not highly permeable because they lack rubble zones in this region and are thus confining units for the ESRP aquifer. Data from Twining et al. (2017) suggests that geothermal waters below the ESRP aquifer upwelled through the annular zone of borehole USGS-142 after the final stage of drilling. Therefore, lower geothermal waters may be contained within subsurface rhyolites in the western INL. Given that no fault is required to accommodate the differences in structural relief of subsurface rhyolites between margin and center of the ESRP after Walcott Tuff B was emplaced, there may not be an efficient conduit for interaction with cooler waters of the ESRP aquifer and lower geothermal waters in the western INL where borehole USGS-142 was drilled.

In spite of the likelihood near borehole USGS-142 that subsurface Snake River-type rhyolites impede flow of the ESRP aquifer, the rhyolite of Butte Quarry crops out south of the Arco Hills. Therefore, the base of the ESRP aquifer may flow through subsurface rhyolites adjacent to the Arco Hills. Furthermore, there are indications of geothermal water being present near Butte City, Idaho (Ross, 1971; Hodges, M., 2018, personnel communication); the interpretation used for this thesis is that the rhyolite of Butte Quarry was a continuous sheet from its exposure to borehole INEL-1, but more data is needed to better confirm this. The rhyolite of Butte Quarry could be a continuous sheet with through-going fractures south of its exposure, or could be at its current location due to faulting near the margins of the ESRP.

Regardless, subsurface Snake River-type rhyolites are confining units for the base of the ESRP aquifer in the western INL because 1) they are dense in borehole USGS 142 and

are thus impermeable and 2) they are found at shallower depths at the margin of the ESRP near the Arco Hills. Furthermore, the depth to the base of the ESRP aquifer decreases toward the Arco Hills (Ackerman et al., 2006), suggesting that the depth to the base of the ESRP aquifer is partially controlled by the geometries of subsurface Snake River-type rhyolites.

4.5 Implications for the Subsidence of the Eastern Snake River Plain

4.5.1 Estimation of the Amount of Subsidence

The interpreted cross section and tentative correlations of the rhyolites of USGS-142, Butte Quarry, and the east side of the Arco Hills provide a minimum amount of subsidence of the ESRP in the western INL between the margin of the ESRP (near the Arco Hills) and to boreholes INEL-1 and WO-2. The minimum amount of subsidence can be calculated assuming the studied ignimbrites were deposited on a flat surface. Table 4.6 summarizes the elevations of selected rhyolites on the margin and in the subsurface of the ESRP.

Table 4.6: Depth and elevation to selected rhyolites

	Latitude (decimal degrees)	Longitude (decimal degrees)	Landsurface elevation (m)	Depth of rhyolite (m) below land surface	Elevation of rhyolite (m)
USGS-142	43.6437	-113.0193	1522	425	1097
WO-2 (Walcott Tuff B)	43.5808	-112.8756	1503	1268	235
East side of Arco Hills	43.7251	-113.0382	1600		1600
WO-2 (Blacktail Creek Tuff)	43.5808	-112.8756	1503	1508.76	-6
INEL-1 (3686')	43.6214	-112.9431	1485	1123	362
Butte Quarry	43.6045	-113.2102	1646		1646

Table 4.6: Table summarizing elevation to selected rhyolites. Latitude, longitude and elevation are referenced to the World Geodetic System of 1984 (WGS-84). Note that similar colors are the tentatively correlated rhyolites; blue is the Walcott Tuff B, yellow is the Blacktail Creek Tuff, and green in the rhyolite of Butte Quarry.

The tentative correlation of the rhyolite of USGS-142 to the Walcott Tuff B in borehole WO-2 provides a minimum amount of subsidence between boreholes USGS-142 and WO-2 post emplacement of the Walcott Tuff B (Table 4.6). The relative elevation of the top of the Walcott Tuff B in borehole USGS-142 is 1097 m (relative to mean sea level), whereas the relative elevation of the top of the Walcott Tuff B in borehole WO-2 is 235 m (relative to mean sea level; Table 4.6). The change in elevation between the projections of the top of Walcott Tuff B is thus 862 m over ~13.5 km. Therefore, 862 m of subsidence occurred between boreholes USGS-142 and WO-2 after the emplacement of the Walcott Tuff B. The regional dip of the Walcott Tuff B between boreholes USGS-142 and WO-2 is ~3.7°.

The tentative correlation of the rhyolite of Butte Quarry to the uppermost Picaboged rhyolite in borehole INEL-1 (INEL-1 3686') provides a minimum amount of subsidence between the surficial exposure of the rhyolite of Butte Quarry to borehole INEL-1 following emplacement of the rhyolite of Butte Quarry (Table 4.6). The elevation of the rhyolite of Butte Quarry is 1646 m (relative to mean sea level), and the elevation of INEL-1 3686' is 362 m (relative to mean sea level). The change in elevation between the surficial exposure of the rhyolite of Butte Quarry and INEL-1 3686' is thus 1284 m over ~21 km.

The tentative correlation of the rhyolite of the east side of the Arco Hills to the Blacktail Creek Tuff provides a minimum amount of subsidence between the surficial exposure of the rhyolite of the east side of the Arco Hills to borehole WO-2 post-emplacement of the Blacktail Creek Tuff (Table 4.6). The elevation of the rhyolite of the east side of the Arco Hills is 1600 m (relative to mean sea level) and the elevation of the Blacktail Creek Tuff in borehole WO-2 is -6 m (relative to mean sea level) over a distance of ~21 km. Therefore, 1.6 km of subsidence occurred between the surficial exposure of the Blacktail Creek Tuff on the east side of the Arco Hills and borehole WO-2, which is nearly consistent with the structural relief of the Blacktail Creek Tuff at Howe Point (1.5 km; Rodgers et al., 2002). The regional dip between these correlative rhyolites is ~4.4 °.

4.5.2 Implications for Flexure along the Western Margin of the Eastern Snake River Plain

Previous research attempted to constrain the timing of crustal flexure along the western margin of the ESRP by dating and correlating volcanic and volcanoclastic rocks associated with ESRP volcanism. The south-southeastern dips of Miocene volcanic rocks in the northern Basin and Range province was interpreted as a result of crustal flexure outboard of the subsided ESRP (McQuarrie and Rodgers 1998; Hough, 2001; Rodgers et al.,

2002; Michalek, 2009). Previous studies have suggested that crustal flexure initiated prior to Snake River-type rhyolite emplacement because these rhyolites dip more shallowly than the maximum plunge of Mesozoic fold-hinges north of the ESRP (McQuarrie and Rodgers, 1998; Hough, 2001; Rodgers et al., 2002; Michalek, 2009).

Given that the surficial exposure of the rhyolite of Butte Quarry dips 20° south toward the ESRP, $\sim 5^\circ$ less than the maximum plunge of Mesozoic fold-hinges in the Arco Hills, the emplacement of this rhyolite must have occurred after flexure initiated (~ 8.1 Ma). Therefore, no more than 5° of southward plunge of Mesozoic fold-hinges could have occurred prior to the emplacement of the rhyolite of Butte Quarry (Fig. 4.2). Figure 4.2 provides a cumulative flexure plot of the northern Basin and Range comparing the maximum plunge of fold-hinges and age dates of emplaced Snake River-type rhyolites in the Lake Hills (Pioneer Mountains), Arco Hills (Lost River Range), southern Lemhi Range, and the southern Beaverhead Mountains. This plot shows the cumulative tilting, constrained by the age dates and southward dips of Snake River-type rhyolites, and the associated uncertainties with amount of crustal flexure following emplacement of Snake River-type rhyolites, where flexure may have occurred any time after the emplacement of rhyolites, or before present. The Arco Hills overlaps in uncertainty with all previous study areas, which may imply flexure deformed Snake River-type rhyolites all along the northern Basin and Range after the emplacement of the Blacktail Creek Tuff (6.66 Ma) (Fig. 4.2). The plot shows that there was significant heterogeneity in timing and magnitude of tilting along the northern margin of the ESRP. Recent results corroborate prior data (McQuarrie and Rodgers, 1998; Rodgers et al., 2002) suggesting that tilting (and flexure, by inference) is coincident with or pre-dates rhyolitic magmatism beneath the adjacent ESRP.

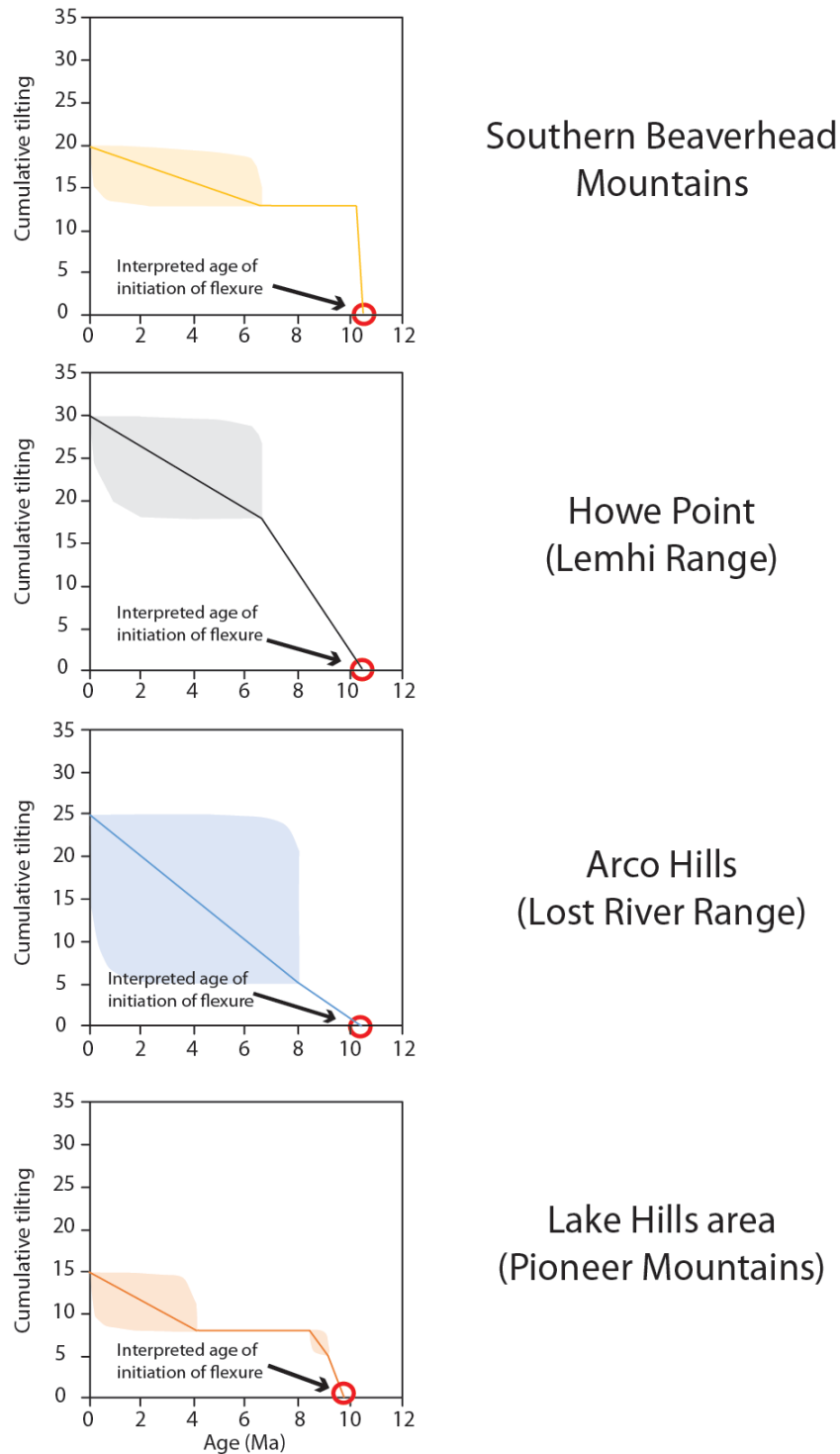


Fig. 4.2: Cumulative tilting plot from previous research and this study. The y-axis represents the maximum plunge of fold-hinges found in each field area. Boxes encompass the uncertainties of the rate of crustal flexure constrained by data Snake River-type rhyolites. Horizontal lines indicate periods of time where flexure ceased in a given area. Data gathered from Hough (2001), Rodgers et al. (2002), and Michalek (2009). Plots are arranged from southwest (bottom) to northeast (top).

The tentative correlation between the rhyolite of Butte Quarry and INEL-1 3686' suggests approximately 1.3 km of subsidence that occurred after emplacement of the rhyolite of Butte Quarry between the outcrop of the rhyolite of Butte Quarry and borehole INEL-1 (Fig. 2.7). McQuarrie and Rodgers (1998) calculated 8.5 km of subsidence of the ESRP relative to the Lost River Range based on flexural modeling of the plunge of Mesozoic fold-hinges. However, they measured the amount of subsidence relative to the location and elevation of their measured 0° fold plunge contour, which is ~ 20 km to the northwest of and ~ 1 km above the rhyolite of Butte Quarry. The difference in the calculated amount of subsidence following emplacement of the rhyolite of Butte Quarry and the modeled subsidence of the ESRP by McQuarrie and Rodgers (1998) can be partially explained by 1) crustal flexure and subsidence of the ESRP that initiated prior to the emplacement of the rhyolite of Butte Quarry, given that at most 5° of south-southeast tilt of Mesozoic fold-hinges could have occurred prior to its emplacement and 2) McQuarrie and Rodgers (1998) calculated the minimum magnitude of subsidence from the 0° fold-plunge contour that is approximately 1 km above the outcrop of the rhyolite of Butte Quarry.

McQuarrie and Rodgers (1998) indicated that the plunge contours of Mesozoic fold-hinges do not match the topographic relief. This observation is further supported because the location of borehole USGS-142 and the outcrop of the rhyolite Butte Quarry are nearly the same distance from the projected 20° fold plunge contour, yet the rhyolite of Butte Quarry is ~ 0.8 km from exposed Paleozoic sedimentary rocks, and borehole USGS-142 is ~ 3 km from exposed Paleozoic sedimentary rocks (Fig. 2.7). Given that the 20° south dip of the rhyolite of Butte Quarry is nearly coincident with the plunge of Mesozoic fold-hinges, the structure contours of McQuarrie and Rodgers (1998) do reflect the structural

downwarp of deformed Snake River-type rhyolites. However, the topographic downwarp is less than the structural downwarp of the ESRP, which is a similar conclusion to McQuarrie and Rodgers (1998).

4.5.3 Migration of the Flexural Hinge Line

The tentative correlations of the rhyolites of USGS-142 and Butte Quarry suggest that the dips of these Snake River-type rhyolites steepen toward the margin of the ESRP near the Arco Hills and beneath the western INL. Also, previous research along the southern extents of the Pioneer Mountains (Michalek, 2009), the Lemhi Range (Rodgers et al., 2002), and the Beaverhead Mountains (Hough, 2001) indicate that surficial exposures of Snake River-type rhyolites of the same age in the same locality, in general, dip uniformly to the south-southeast close to the margin between the ESRP and northern Basin and Range. Regionally, this would define a broad-scale monocline whose inflection point occurs somewhere near the margin of the ESRP near the northern Basin and Range province.

The location of the flexural hinge line, as defined by the 0° fold-plunge contour (McQuarrie and Rodgers, 1998), may not have been in its current position after the emplacement of the rhyolite of Butte Quarry. Given that the projection of the Picabo volcanic field occurs south-southwest from the Arco Hills (Fig. 1.2; Drew et al., 2013), and the rhyolite of Butte Quarry is interpreted to have been produced during the latest stages of Picabo-age volcanism, the hotspot must have been in close proximity to the outcrop of the rhyolite of Butte Quarry shortly after its emplacement. The close proximity of the hotspot would increase heat flux near the Arco Hills, and decrease the flexural rigidity of the surrounding country rock. Consequently, the flexural hinge-line may have been in closer proximity to the margin between the ESRP and the Arco Hills. After the hotspot

migrated, the surrounding country rock would have cooled and increased its flexural rigidity, forcing the flexural hinge line to migrate northwest, perhaps coincident with the migration of the seismic parabola (Anders et al., 1989).

The interpreted rotation of northeast-striking faults in the Arco Hills suggested from the fault plane solutions, the shallowing of shortening axes toward the ESRP, the steepening of southeast-dipping faults toward the ESRP, and shallowing of northwest-dipping faults toward the ESRP also provides evidence for a migrating flexural hinge line. The shortening and extension axes of the distal fault domain illustrate relatively clustered distributions ($K = 1.65$ and 1.43 , respectively), whereas shortening and extension axes of the proximal fault domain illustrate relatively girdled to no preference in fabric distribution ($K = 0.63$ and 0.98 , respectively). A plausible interpretation for the difference in fabric shape between these fault domains is that the faults in the proximal fault domain formed prior to faults in the distal domain, early in the subsidence of the ESRP and flexure along the northern margin of the ESRP. Older faults in the proximal fault domain may have formed and started to rotate, similar to the Mesozoic fold-hinges (Fig. 4.3). Subsequently, the flexural hinge line migrated to the northwest and continued to form flexural-related faults in the distal fault domain (Fig. 4.3). Given that the proximal fault domain is southeast of the 20° fold-plunge contour of McQuarrie and Rodgers (1998), it is plausible to assume that the faults in the proximal domain were rotated more than those found in the distal fault domain.

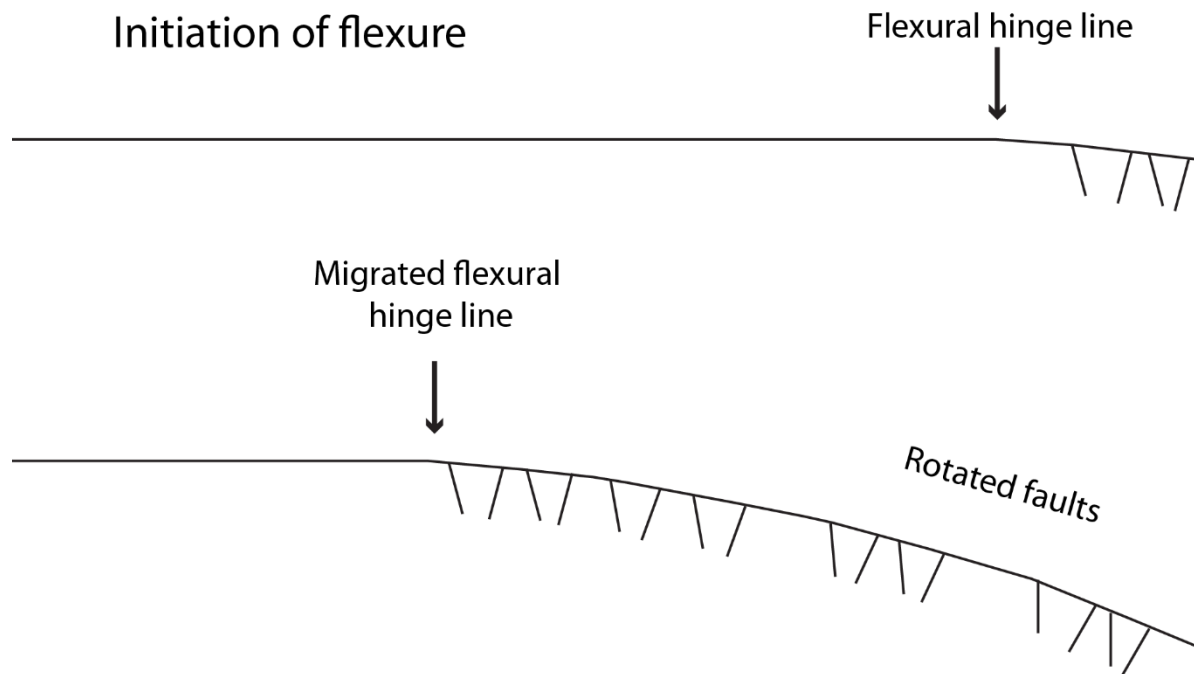


Figure 4.3: Schematic representation of a migrating flexural hinge line.

Figures 4.4 and 4.5 are cartoons of the hypothesized temporal evolution of the ESRP with regard to the migration of the Yellowstone hotspot and the seismic parabola. In these cartoons, the migration of the seismic parabola is coincident with the migration of the flexural hinge line, and flexure is confined to the “collapse shadow” (Anders et al., 1989). As McQuarrie and Rodgers (1998) indicated, the proposed mid-crustal sill that produced the subsidence of the ESRP and the observed flexure north of the ESRP is not responsible for strengthening the interior of the seismic parabola (collapse shadow) because the mid crustal sill is modeled to not project past the boundary of the ESRP. Therefore, another explanation must be applied to explain the aseismicity of the ESRP and surrounding Basin and Range found in the collapse shadow. The subsidence and flexure outboard of the ESRP, where the crust near the ESRP has effectively reduced its gravitational potential energy from the subsidence of the ESRP, likely drives the aseismicity in the collapse shadow of the

seismic parabola. As Basin and Range faults approach the collapse shadow, they cease to extend because the crust near the ESRP has a lower gravitational potential energy.

Given that no Snake River-type rhyolites or related volcanoclastic rocks dip as steeply as the plunges of Mesozoic fold-hinges along the ESRP, except south of the Arco Hills, more steeply-dipping volcanic and volcanoclastic rocks south-southeast of the Pioneer Mountains, Lemhi Range, and Beaverhead Mountains must be buried by younger Snake River-type rhyolites and basalts (Fig. 4.5). Furthermore, figures 4.4 and 4.5 illustrate that the margin of the ESRP widens with time, which is plausible because the Yellowstone volcanic field is confined to a discrete cluster, whereas the ESRP to the southwest is wider. However, this does not explain why the ESRP is nearly the same width throughout the volcanic province. Northeast-striking flexural related faults also rotate with time, where faults associated with the onset of flexure are continuously rotated with the migration of the flexural hinge line, and faults proximal to the ESRP are rotated more than faults distal to the ESRP.

The northeast-striking faults in the Arco Hills accommodated extension in a nearly exclusively dip-slip sense. Therefore, right-lateral shear associated with the Centennial shear zone may be accommodated elsewhere, such as in discrete zones, possibly along distinct segment boundaries of Basin and Range faults (Fig. 4.4) or along localized zones that have not been previously documented.

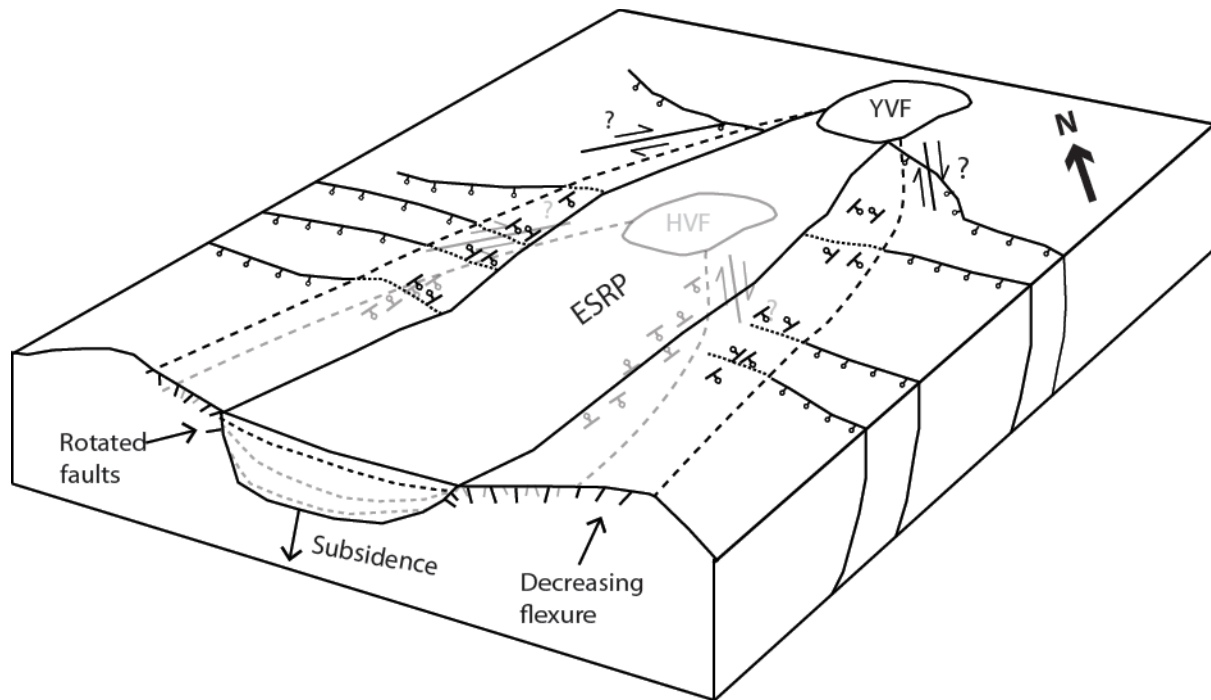


Figure 4.4: 3D block model illustrating an interpreted temporal evolution of the ESRP with regards to the migration of the hotspot, and the seismic parabola. Dashed lines indicate the geographic extent of the collapse shadow of the seismic parabola. The Centennial shear zone is projected southwest of the Yellowstone volcanic field. Gray objects indicate Heise-aged events. HVF = Heise volcanic field; YVF = Yellowstone volcanic field. Modified from Anders et al. (1989).

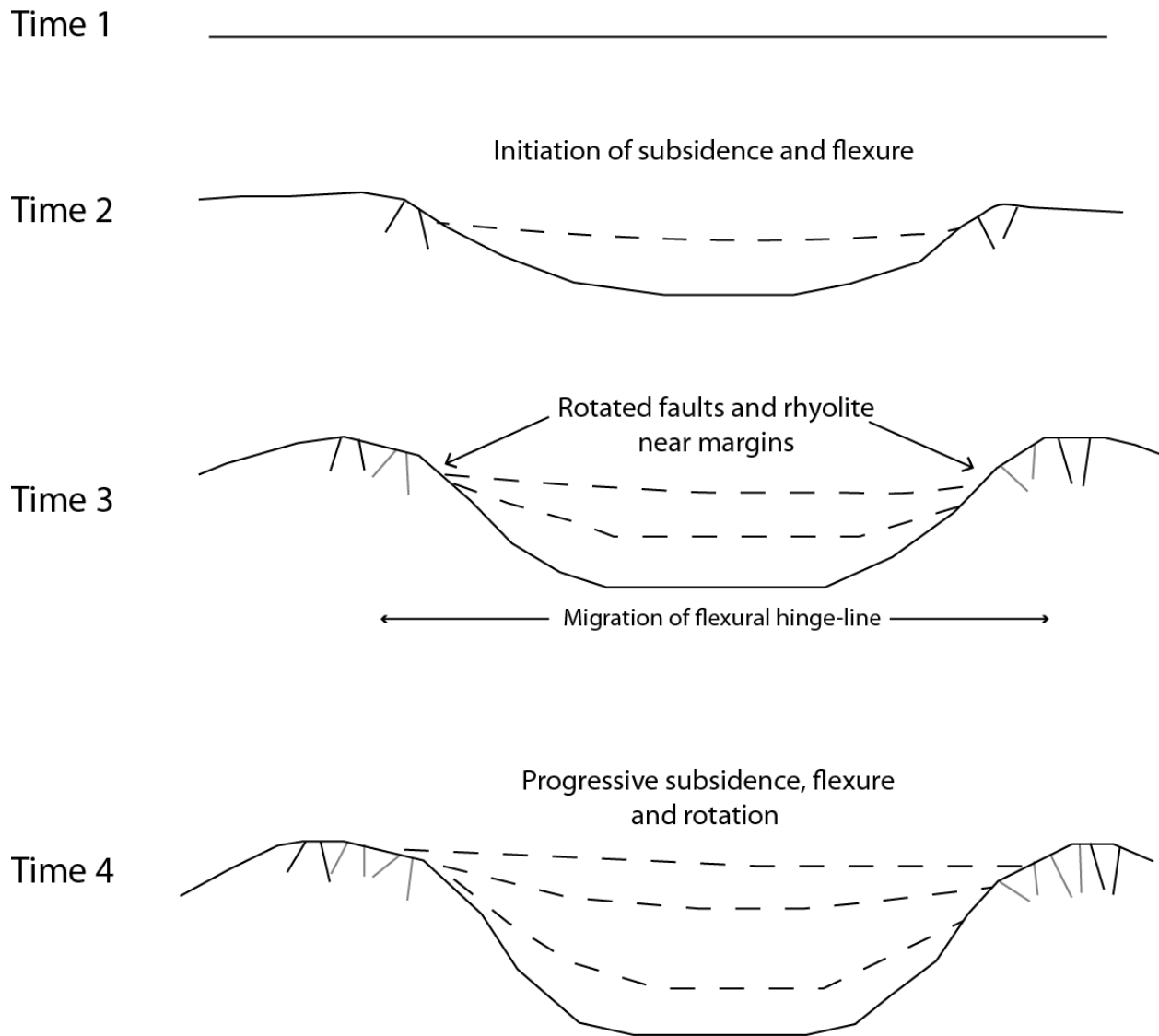


Figure 4.5: Schematic cross sections for the temporal evolution of the ESRP near the Arco Hills from northwest to southeast across the ESRP. Gray faults represent older faults that have been rotated with flexure outboard of the subsided ESRP. Time 3 would correlate to the Heise-aged volcanism (Fig. 4.4), whereas time 4 would correlate with present day (Fig. 4.4).

CHAPTER 5: CONCLUSIONS

Through the correlation of the studied rhyolites, this thesis was able to constrain the geometry of subsurface rhyolites near the margin of the ESRP in the western INL and establish minimum amounts of subsidence of the ESRP after their emplacement. Furthermore, the regional significance of northeast-striking faults outboard of the margin of the ESRP has been interpreted. New data and interpretations suggest the following:

1. The rhyolite of USGS-142 is tentatively correlated to the Walcott Tuff B found in borehole WO-2. This not only constrains the degree of continuity of Heise-aged rhyolites in the western INL, but also establishes a minimum amount of subsidence of ~860 m between boreholes USGS-142 and WO-2 following the emplacement of the Walcott Tuff B.
2. The rhyolite of Butte Quarry is tentatively correlated to the upper-most Picabo-aged ignimbrite found in borehole INEL-1 at a depth of 3686' below land surface. This correlation constrains the degree of continuity of subsurface Picabo-aged ignimbrites beneath the western INL, and establishes a minimum amount of subsidence following the emplacement of the rhyolite of Butte Quarry of ~1.3 km between the surface exposure of the rhyolite of Butte Quarry to borehole INEL-1.
3. The rhyolite of the east side of the Arco Hills is tentatively correlated to the Blacktail Creek Tuff. This correlation suggests ~1.6 km of subsidence occurred post-emplacement of the Blacktail Creek Tuff over a distance of ~21 km, and defines a regional dip of this rhyolite of ~4.4°.
4. The northeast-striking faults of the Arco Hills accommodated crustal extension in a nearly exclusively dip-slip sense, which suggests that they did not accommodate

differential extension between the northern Basin and Range and the ESRP (cf. Payne et al., 2012). Rather, they likely accommodated crustal flexure from the subsidence of the ESRP.

5. The rhyolite of Butte Quarry dips 20° south and yielded a U-Pb zircon age of 8.13 ± 0.7 Ma. This suggests that the majority of flexure, and perhaps subsidence of the ESRP, occurred after emplacement of this rhyolite because its dip is nearly the same as previously documented fold-plunge contours of McQuarrie and Rodgers (1998). Approximately 5° of southeast tilt of Mesozoic fold-hinges may have occurred prior to the emplacement of the rhyolite of Butte Quarry.
6. The 20° south dip of the rhyolite of Butte Quarry and the interpreted rotation of northeast-striking faults in the Arco Hills together suggest that the majority of flexure is confined to the margin of the ESRP near the Arco Hills and the southern extent of the northern Basin and Range, and does not occur throughout the subsurface of the ESRP. The clustered distribution of shortening and extension axes of the northeast-striking faults in the distal fault domain and the mostly girdled distribution of shortening and extension axes in the proximal fault domain suggests that a “flexural wave,” likely related to the “collapse shadow” of the seismic parabola (Anders et al., 1989), moved toward the northwest away from the ESRP and, at present resides near the current flexural hinge line (McQuarrie and Rodgers, 1998).
7. All structural relief of subsurface rhyolites between the margin of the ESRP and the Arco Hills post emplacement of the rhyolite of Butte Quarry can be attributed to regional subsidence and local flexure of the ESRP.

CHAPTER 6: SUGGESTIONS FOR FUTURE WORK

The tentative correlation of the rhyolite of USGS-142 to the Walcott Tuff B in borehole WO-2 suggests that the Walcott Tuff B should project through borehole INEL-1. However, only the Kilgore Tuff was reported as a Heise-aged rhyolite in borehole INEL-1 based on a fission-track age of 4.2 ± 0.3 Ma on the uppermost rhyolitic unit in borehole INEL-1 (Morgan et al., 1984). Unfortunately, only drill cuttings and limited core are available for borehole INEL-1, so to confirm the presence (or absence) of the Walcott Tuff B in borehole INEL-1, U-Pb zircon ages must be obtained from drill cuttings in the rhyolites above the Picabo-aged rhyolites (3686' below land surface). In addition, $\delta^{18}\text{O}$ stable isotope analyses could also be conducted on drill cuttings as a useful finger print tool for correlation.

Bindeman et al. (2007) and Watts et al. (2011) provide abundant $\delta^{18}\text{O}$ melt data for Heise and Yellowstone-aged rhyolites. However, neither Bindeman et al. (2007) nor Watts et al. (2011) divided the Walcott Tuff into its two members: A and B (e.g. Anders et al., 2014). Therefore, $\delta^{18}\text{O}$ stable isotope analyses should be conducted for both members to 1) confirm that the Walcott Tuff B is depleted in heavy oxygen isotopes, as suggested from this research and 2) to determine whether $\delta^{18}\text{O}$ varies significantly within each member of the Walcott Tuff. Furthermore, XRF analyses should be conducted for the Walcott Tuff A in borehole WO-2 to 1) confirm that the Walcott Tuff A and B are compositionally distinct and 2) to determine if whole rock geochemistry varies between subsurface and surface Snake River-type rhyolites.

An XRF analyses conducted for a Snake River-rhyolite at a depth of 4997' in WO-2 by McCurry and Rodgers (2009), which was later confirmed to be the Blacktail Creek Tuff

by Anders et al. (2014) based on Ar-Ar geochronology and paleomagnetic inclinations, suggests that whole rock geochemistry analyses vary between subsurface and surface exposures of the Blacktail Creek Tuff (Table 4.2). The analyses reported by Watts et al. (2011) and McCurry and Rodgers (2009) display notable differences in SiO₂ (74.4 % and 77.47%, respectively), TiO₂ (0.31% and 0.24%, respectively), CaO (1.22% and 0.49%, respectively), Ba (1099 ppm and 607 ppm, respectively), and Sr (84 ppm and 38 ppm, respectively). Future whole rock geochemistry analyses should determine whether analyses vary between subsurface and surface Snake River-type rhyolites.

Thin section analyses conducted for the West Pocatello rhyolite could not differentiate this rhyolite between an ignimbrite and lava flow. Therefore, a future research project could be incrementally sampling the exposure of the West Pocatello rhyolite for thin section analyses to 1) differentiate between an ignimbrite and lava flow and 2) determine an accurate representation of phenocryst modes to correlate the West Pocatello rhyolite to the rhyolite of Butte Quarry. Although U-Pb zircon ages, Hf isotope analyses, whole rock geochemistry, and $\delta^{18}\text{O}$ stable isotope analyses are consistent between the rhyolite of Butte Quarry and the West Pocatello rhyolite, the West Pocatello rhyolite could still be a lava flow, which would deny a plausible correlation between these separated rhyolites.

Thin sections created from the microcrystalline core of the rhyolite of Butte Quarry displayed rotated plagioclase phenocrysts, which define porphyroclasts. Future research for this rhyolite should incrementally sample the rhyolite of Butte Quarry for oriented thin sections, where δ -objects (porphyroclasts) could be identified to indicate the direction of shear, which will allow for the interpretation for the direction of transport for the rhyolite

of Butte Quarry. Given that stretched vesicles in the rhyolite of Butte Quarry indicate an east-west lineation, a future project could differentiate the direction of transport with abundant kinematic data (e.g. Andrews and Branney, 2010).

Lastly, the northeast-striking faults in the Arco Hills are interpreted to be rotated similar to Mesozoic fold-hinges (e.g. McQuarrie and Rodgers, 1998) because: shortening axes plunge more shallowly in the proximal fault domain compared to the distal domain, and northwest-dipping fault planes shallow toward the ESRP, whereas southeast-dipping fault planes steepen toward the ESRP. A similar kinematic analysis of northeast-striking faults should be conducted on the southern side of the ESRP to determine if the rotation of faults is seen on both sides of the ESRP.

REFERENCES

- Ackerman, D.J., Rattray, G.W., Rousseau, J.P., Davis, L.C., and Orr, B.R., 2006, A conceptual model of ground-water flow in the eastern Snake River Plain aquifer at the Idaho National Laboratory and vicinity with implications for contaminant transport: U.S. Geological Survey Scientific Investigations Report 2006-5122, 62 p.
- Allmendinger, R.W., 1982, Sequence of late Cenozoic deformation in the Blackfoot Mountains, southeastern Idaho, *in* Bonnicksen, B. and Breckenridge, R.M., eds., Cenozoic Geology of Idaho: Idaho Bureau of Mines and Geology Bulletin 26, p. 505-516.
- Allmendinger, R.W., Cardozo, N., and Fisher, D., 2012, Structural geology algorithms: Vectors and tensors in structural geology: Cambridge University Press, 304 p.
- Anders, M.H., Geissman, J.W.M., Piety, L.A., and Sullivan, J.T., 1989, Parabolic distribution of circumeastern Snake River Plain seismicity and latest Quaternary faulting: migratory pattern and association with the Yellowstone Hotspot: *Journal of Geophysical Research*, v. 94, no. B2, p. 1589-1621.
- Anders, M.H., Rodgers, D.W., Hemming, S.R., Saltzman, J., DiVenere, V.J., Hagstrum, J.T., Embree, G.F., and Walter, R.C., 2014, A fixed sublithospheric source for the late Neogene track of the Yellowstone hotspot: implications of the Heise and Picabo volcanic fields: *Journal of Geophysical Research: Solid Earth*, v. 119, p. 2871-2906, doi: 10.1002/2013JB010483.
- Anderson, E.M., 1951, The dynamics of faulting and dyke formations: Edinburg and London, Oliver & Boyd, 206 p.

- Anderson, S.R., and Liszewski, M.J., 1997, Stratigraphy of the unsaturated zone and the Snake River Plain aquifer at and near the Idaho National Engineering Laboratory, Idaho: U.S. Geological Survey Water-Resources Investigations Report 97-4183 (DOE/ID-22142), 65 p.
- Andrews, G.D.M., and Branney, M.J., 2010, Emplacement and rheomorphic deformation of a large, lava-like rhyolitic ignimbrite: Grey's Landing, southern Idaho: Geological Society of America Bulletin, v. 123, no. 3-4, p. 725-743, doi: 10.1130/B30167.1.
- Bartholomay, R.C., Maimer, N.V., Rattray, G.W., and Fisher, J.C., 2017, An update of hydrologic conditions and distribution of selected constituents in water, eastern Snake River Plain aquifer and perched groundwater zones, Idaho National Laboratory, Idaho, emphasis 2012-2015: U.S. Geological Survey Scientific Investigations Report 2017-5021 (DOE/ID-22242), 87 p., doi: 10.3133/sir20175021.
- Bindeman, I.N., and Valley, J.W., 2003, Rapid generation of both high- and low- $\delta^{18}\text{O}$, large-volume silicic magmas at the Timber Mountain/ Oasis Valley caldera complex, Nevada: Geological Society of America Bulletin, v. 115, no. 5, p. 581-595.
- Bindeman, I.N., Watts, K.E., Schmitt, A.K., Morgan, L.A., and Shanks, P.W.C., 2007, Voluminous low $\delta^{18}\text{O}$ magmas in the late Miocene Heise Volcanic Field, Idaho: implications for the fate of Yellowstone hotspot calderas: *Geology*, v. 35, no. 11, p. 1019-1022, doi: 10.1130/G24141A.1.
- Branney, M.J., and Acocella, V., 2015, Calderas, in Sigurdsson, H., Houghton, B., McNutt, S., Rymer, H., and Stix J., eds., *The Encyclopedia of Volcanoes*: Elsevier Inc., p. 299-315, doi: 10.1016/B978-0-12-385938-9.00016-X.

Branney, M.J., Bonnicksen, B., Andrews, G.D.M., Ellis, B., Barry, T.L., and McCurry, M., 2008, 'Snake River (SR)-type' volcanism at the Yellowstone hotspot track: distinctive products from unusual, high temperature silicic super-eruptions: *Bulletin of Volcanology*, v. 70, p. 293-314, doi: 10.1007/s00445-007-0140-7.

Branney, M.J., and Kokelaar, P., 1992, A reappraisal of ignimbrite emplacement: progressive aggradation and changes from particulate to non-particulate flow during emplacement of high-grade ignimbrite: *Bulletin of Volcanology*, v. 54, p. 504-520.

Bruhn, R.L., Wu, D., and Lee, J.J., 1992, Final report on the structure of the southern Lemhi and Arco Fault Zone, Idaho, EGG-NPR-10680 Informal Report prepared for the U.S. Department of Energy, 59 p.

Christiansen, R.L., 2001, The Quaternary and Pliocene Yellowstone plateau volcanic field of Wyoming, Idaho, and Montana: U.S. Geological Survey Professional Paper 729-G, 156 p.

Coble, M.A., and Mahood, G.A., 2012, Initial impingement of the Yellowstone plume located by widespread silicic volcanism contemporaneous with Columbia River flood basalts: *Geology*, v. 40, no. 7, p. 655-658, doi: 10.1130/G32692.

Doherty, D.J., McBroome, L.A., and Kuntz, M.A., 1979, Preliminary geological interpretation and lithologic log of the exploratory geothermal test well (INEL-1), Idaho National Engineering Laboratory, eastern Snake River Plain, Idaho: U.S. Geological Survey Open File Report 79-1248, 10 p.

Drew, D.L., Bindeman, I.N., Watts, K.E., Schmitt, A.K., Fu, B., and McCurry, M., 2013, Crustal-scale recycling in caldera complexes and rift zones along the Yellowstone hotspot track: O and Hf isotopic evidence in diverse zircons from voluminous rhyolites of the

- Picabo volcanic field, Idaho: *Earth and Planetary Science Letters*, v. 381, p. 63-77, doi: 10.1016/j.epsl.2013.08.007.
- Gehrels, G., and Pecha, M., 2014, Detrital zircon U-Pb geochronology and Hf isotope geochemistry of Paleozoic and Triassic passive margin strata of western North America: *Geosphere*, v. 10, no. 1, p. 49-65, doi: 10.1130/GES00889.1.
- Helm-Clark, C., Ansley, S., McLing, T., and Wood, T., 2005, Borehole and well middle-1823 and its relationship to the stratigraphy of the south-central Idaho National Laboratory: U.S. Geological Survey Idaho Completion Project/ EXT-05-00790, 36 p.
- Hodges, M.K.V., 2006, Tertiary stratigraphy of the Idaho Medicine Lodge Valley, Clark County, Idaho: [Master's Thesis] Idaho State University Pocatello, 177 p.
- Hough, B.G., 2001, Temporal constraints on crustal flexure adjacent to the eastern Snake River Plain, Idaho: [Master's thesis] Idaho State University Pocatello, 94 p.
- Janecke, S.U., 1992, Kinematics and timing of three superposed extensional systems, east central Idaho: evidence for an Eocene tectonic transition: *Tectonics*, v. 11, no. 6, p. 1121-1138.
- Janecke, S.U., 1995, Eocene to Oligocene half grabens of east-central Idaho: structure, stratigraphy, age, and tectonics: *Northwest Geology*, v. 24, p. 159-199.
- Kelley, S., 2002, K-Ar and Ar-Ar Dating: The Open University, 34 p., doi: 10.2138/rmg.2002.47.17.
- Kuntz, M.A., Skipp, B.A., Lanphere, M.A., Scott, W.E., Pierce, K.L., Dalrymple, G.B., Champion, D.E., Embree, G.F., Page, W.R., Morgan, L.A., Smith, R.P., Hackett, W.R., and Rodgers, D.W., 1994, Geologic map of the Idaho National Engineering Laboratory and

- adjoining areas, eastern Idaho: U.S. Geological Survey Miscellaneous Investigations Series Map I-2330.
- Kuntz, M.A., Anderson, S.R., Champion, D.E., Lanphere, M.A., and Grunwald, D.J., 2002, Tension cracks, eruptive fissures, dikes, and faults related to late Pleistocene-Holocene basaltic volcanism and implications for the distribution of hydraulic conductivity in the eastern Snake River Plain, Idaho, *in* Link, P.K, and Mink, L.L., *Geology, Hydrogeology and Environmental Remediation: Idaho National Engineering and Environmental Laboratory, Eastern Snake River Plain, Idaho: Boulder, Colorado, Geological Society of America Special Paper 353*, p. 111-134.
- Link, P.K., and Janecke, S.U., 1999, Geology of east-central Idaho: geologic roadlogs for the Big and Little Lost River, Lemhi, and Salmon River Valleys, *in* Hughes, S.S., and Thackray, G.D., eds., *Guidebook to the Geology of Eastern Idaho: Pocatello, Idaho Museum of Natural History*, p. 295-334.
- Lipman, P.W., 1997, Subsidence of ash-flow calderas: relation to caldera size and magma-chamber geometry: *Bulletin of Volcanology*, v. 59, p. 198-218.
- Ludwig, K.R., 2008, User's manual for Isoplot/Excel rev. 3.70: Berkeley Geochronology Center, Special Publication.
- Mann, L.J., 1986, Hydraulic properties of rock units and chemical quality of water for INEL-1, a 10,365-foot deep test hole drilled at the Idaho National Engineering Laboratory, Idaho: U.S. Geological Survey Water-Resources Investigations Report 86-4020 (IDO-22070), 23 p.
- Marrett, R., and Allmendinger, R.W., 1990, Kinematic analysis of fault-slip data: *Journal of*

- Structural Geology, v. 12, no. 8, p. 973-986.
- Mazurek, J., 2004, Genetic controls on basalt alteration within the eastern Snake River Plain aquifer system, Idaho: [Master's Thesis] Idaho State University Pocatello, 227 p.
- McBroome, L.A., Doherty, D.J., and Embree, G.F., 1981, Correlation of major Pliocene and Miocene ash-flow sheets, eastern Snake River Plain, Idaho, *in* Montana Geological Society 1981 Field Conference and Symposium Guidebook to Southwest Montana, p. 323-330.
- McCurry, M., and Rodgers, D.W., 2009, Mass transfer along the Yellowstone hotspot track I: petrologic constrains on the volume of mantle-derived magma: *Journal of Volcanology and Geothermal Research*, v. 188, p. 86-98, doi: 10.1016/j.jvolgeores.2009.04.001.
- McCurry, M., McLing, T., Smith, R.P., Hackett, W.R., Goldsby, R., Lochridge, W., Podgorney, R., Wood, T., Pearson, D., Welhan, J., and Plummer, M., 2016, Geologic setting of the Idaho National Laboratory Geothermal Resource Research Area, *in* Proceedings, 41st Workshop on Geothermal Reservoir Engineering: Stanford University, Stanford California, SGP-TR-209, 20 p.
- McQuarrie, N., and Rodgers, D.W., 1998, Subsidence of a volcanic basin by flexure and lower crustal flow: the eastern Snake River Plain, Idaho: *Tectonics*, v. 17, no. 2, p. 203-220.
- Michalek, M., 2009, Age and amount of crustal flexure in the Lake Hills, south-central Idaho, and implications for the subsidence of the eastern Snake River Plain: [Master's thesis] Idaho State University Pocatello, 125 p.

- Morgan, L.A., Doherty, D.J., and Leeman, W.P., 1984, Ignimbrites of the eastern Snake River Plain: evidence for major caldera-forming eruptions: *Journal of Geophysical Research*, v. 89, no. B10, p. 8665-8678.
- Morgan, L.A., and McIntosh, W.C., 2005, Timing and development of the Heise volcanic field, Snake River Plain, Idaho, western USA: *Geological Society of America Bulletin*, v. 117, no. 3/4, p. 288-306, doi: 10.1130/B25519.1.
- Morse, L.H., 2002, Basalt alteration and authigenic mineralization near the effective base of the Snake River Plain aquifer at the Idaho National Engineering and Environmental Laboratory, Idaho: [Master's Thesis] Idaho State University Pocatello, 189 p.
- Parker, S.D., 2016, Tectonic alteration of a major Neogene river drainage of the Basin and Range: [Master's Thesis] University of Montana, 122 p.
- Payne, S.J., McCaffrey, R., King, R.W., and Kattenhorn, S.A., 2012, A new interpretation of deformation rates in the Snake River Plain and adjacent basin and range regions based on GPS measurements: *Geophysical Journal International*, v. 189, p. 101-122, doi: 10.1111/j.1365-246X.2012.05370.x.
- Pierce, K.L., and Morgan, L.A., 1992, The track of the Yellowstone hotspot: volcanism, faulting and uplift, *in* Link, P.K., Kuntz, M.A., and Platt, L.B., eds., *Regional Geology of Eastern Idaho and Western Wyoming: Geological Society of America Memoir 179*, p. 1-52.
- Rodgers, D.W., Hackett, W.R., and Ore, H.T., 1990, Extension of the Yellowstone plateau, eastern Snake River Plain, and Owyhee plateau: *Geology*, v. 18, p. 1138-1141.
- Rodgers, D.W., Ore, H.T., Bobo, R.T., McQuarrie, N., and Zentner, N., 2002, Extension and subsidence of the eastern Snake River Plain, Idaho, *in* Bonnicksen, B., White, C.M.,

- and McCurry, M., eds., Tectonic and Magmatic Evolution of the Snake River Plain Volcanic Province: Idaho Geological Survey Bulletin 30, p. 121-155.
- Ross, S.H., 1971, Geothermal potential of Idaho: Idaho Bureau of Mines and Geology, pamphlet no. 150, 73 p.
- Shervais, J.W., Vetter, S.K., and Hanan, B.B., 2006, Layered mafic sill complex beneath the eastern Snake River Plain: evidence from cyclic geochemical variations in basalt: *Geology*, v. 34, no. 5, p. 365-368, doi: 10.1130/G22226.1.
- Skipp, B., 1988, Cordilleran thrust belt and faulted foreland in the Beaverhead Mountains, Idaho and Montana, *in* Schmidt, C.J., and Perry, W.J., Jr., eds., Interaction of the Rocky Mountain foreland and the Cordilleran thrust belt: Geological Society of America Memoir, v. 171, p. 237-266.
- Skipp, B., Snider, L.G., Janecke, S.U., and Kuntz, M.A., 2009, Geologic map of the Arco 30 X 60 minute quadrangle, South-Central Idaho: Idaho Geological Survey Publication GM-47, scale 1:100,000, doi: 10.1029/2003GC000661.
- Sparlin, M.A., and Braile, L.W., 1982, Crustal structure of the eastern Snake River Plain determined from ray trace modeling of seismic refraction data: *Journal of Geophysical Research*, v. 87, no. B4, p. 2619-2633.
- Twining, B.V., Hodges, M.K.V., Schusler, K.L., and Mudge, C., 2017, Drilling, construction, geophysical log data, and lithologic log for boreholes USGS-142 and USGS-142A, Idaho National Laboratory, Idaho: U.S. Geological Survey Data Series 1058 (DOE/ID-22243), 21 p., doi: 10.3133/ds1058.

- U.S. Geological Survey, 1985, National Water summary 1984—Hydrologic events, selected water-quality trends, and ground-water resources: U.S Geological Survey Water-Supply Paper 2275, 467 p.
- Vervoort, J.D., Patchett, P.J., Blichert-Toft, J., and Albarède, F., 1999, Relationships between Lu-Hf and Sm-Nd isotopic systems in the global sedimentary system: *Earth and Planetary Science Letters*, v. 168, p. 79-99.
- Watts, K.E., Bindeman, I.N., and Schmitt, A.K., 2011, Large-volume rhyolite genesis in caldera complexes of the Snake River Plain: insights from the Kilgore Tuff of the Heise volcanic field, Idaho, with comparison to Yellowstone and Bruneau-Jarbridge rhyolites: *Journal of Petrology*, v. 52, no. 5, p. 857-890, doi: 10.1093/petrology/egr005.
- Welhan, J.A., Clemo, T.M., and Gégó, E.L., 2002, Stochastic simulation of aquifer heterogeneity in a layered basalt aquifer system, eastern Snake River Plain, Idaho, *in* Link, P.K, and Mink, L.L., eds., *Geology, hydrogeology and environmental remediation: Idaho National Engineering and Environmental Laboratory, Eastern Snake River Plain, Idaho: Boulder, Colorado, Geological Society of America Special Paper 353*, p. 225-247.
- Whitehead, R.L., 1992, Geohydrologic framework of the Snake River Plain regional aquifer system, Idaho and eastern Oregon: U.S. Geological Survey Professional Paper 1408-B, 32 p.
- Woodcock, N.H., 1977, Specification of fabric shapes using an eigenvalue method: *Geological Society of America Bulletin*, v. 88, p. 1231-1236.

Zentner, N.C., 1989, Neogene normal faults related to the structural origin of the eastern Snake River Plain, Idaho: [Master's Thesis] Idaho State University Pocatello, 57 p.

Zheng, Y., 1993, Calculation of oxygen isotope fractionation in anhydrous silicate minerals: *Geochimica et Cosmochimica Acta*, v. 57, p. 1079-1091.

APPENDIX A: ZIRCON SEPARATION AND TROUBLES WITH SEPARATING ZIRCONS FROM IGNIMBRITE VITROPHYRES

Zircon Separation and Mounting

Samples were individually crushed in a Braun Chipmunk to ~1 cm sized pieces. These pieces were then ground in a rotating disc mill, and sieved to insure to collect grains smaller than 425 μm . Iron filings were removed by passing a hand magnet over the sand-sized sample, prior to sorting the sample by density difference using a Holman-Wilfley table. The densest portion of each sample were dried in an oven at $\sim 60^\circ\text{C}$ for seven hours immediately after removing from the Holman-Wilfley table. Dried samples were further separated by passing them through a Frantz barrier field magnetic separator to remove magnetic grains. Each sample was passed through the Frantz at 0.3, 0.7, 1.0, and 1.8 amps, leaving behind nonmagnetic phenocrysts. Phenocrysts from each sample were sorted via specific gravity by suspending them in methylene iodide within a separatory funnel. Phenocrysts that sank to the bottom of the separatory funnel were then collected onto a filter paper and cleaned of methylene iodide using acetone.

Cleaned phenocrysts were observed under a binocular microscope, and zircon phenocrysts were picked with tweezers, insuring each zircon best represented the whole population present. I picked approximately 50 zircon phenocrysts for each sample, and embedded them in an epoxy mount in separate, ordered rows. Standards for U-Pb geochronology and Hf analysis were placed around the samples, and in the center of the epoxy mount. Samples were imaged using an SEM with an attached cathodoluminescence detector.

Problems with Zircon Recovery

Initially, approximately 10 pounds of rhyolitic ignimbrite vitrophyre was sampled to separate zircons for the rhyolite of Butte Quarry and the rhyolite of the east side of the Arco Hills. The exact process was followed as outlined above, but each sample yielded only a few or no zircons. The microcrystalline center zone of the rhyolite of USGS-142 was originally sampled, because there is not enough vitrophyre to process for zircons in the core; this sample produced ~60 zircons. Therefore, ~15 pounds of the microcrystalline center zone of the rhyolite of Butte Quarry was resampled, and processed, which produced ample zircon phenocrysts.

This observation is perplexing, because based on prior XRF geochemistry work by Dr. Mike McCurry, both the vitrophyre and microcrystalline center zone contained a high concentration of Zr, which implied a presence of zircon (McCurry 2017, personal communication), and a zircon phenocryst is found in a thin section of the vitrophyre of the rhyolite of Butte Quarry. After hand-crushing vitrophyre samples for Ar-Ar and δO^{18} analyses (see Appendix B), phenocrysts were clearly mantled by dark gray-black glass. Although grains run through the disc mill are finer than those that were hand crushed, zircons from vitrophyre samples run separation may have been mantled by glass. If this is the case, during the specific gravity separation process, glass-mantled zircons would float because their effective specific gravity would be much lower ($<3.33 \text{ g/cm}^3$; less than methylene iodide) than the average zircon (4.85 g/cm^3), or zircons were lost during the density separation process of the Wilfley Table.

APPENDIX B: SEPARATING PHENOCRYSTS FROM VITROPHYRE USING HF DISSOLUTION

Overview

Samples of vitrophyre from the studied rhyolitic ignimbrites were hand crushed with a clean hammer on a clean iron plate. Crushed rock was sieved, separating grains between $X < 425\mu\text{m}$ and $425\mu\text{m} < X < 1.18\text{ mm}$; sand-sized samples ($425\mu\text{m} < X < 1.18\text{ mm}$) were used for phenocryst separation because average feldspar widths were $\sim 500\mu\text{m}$ in thin section for each sample. After sieving, sand-sized samples were separately cleaned by placing them into a beaker with tap water, and decanting the water into the sink, refilling the beaker several times until the decanted water was more or less clear. This allowed for dust to float off the grains/phenocrysts for inspection.

Cleaned sand-sized samples were observed under a binocular microscope. Due to the aphanitic nature of each rhyolitic ignimbrite, samples consisted mostly of dark gray-black glass grains; phenocrysts noted in the sand-sized samples were commonly mantled by glass. Therefore, glass had to be removed from phenocrysts prior to Ar-Ar age dating and δO^{18} isotope analyses. Hydrofluoric acid (HF) dissolution was used because it was hypothesized that HF would dissolve amorphous glass faster than phenocrysts, leaving behind clean feldspar, pyroxene, and quartz phenocrysts.

Process for HF Dissolution

1. Place 5-6 500 mL Teflon beakers, Teflon graduated cylinder, 1 L Teflon beaker (or a Teflon container of similar dimensions), HF, magnetic plate, Teflon magnetic stir rod, and Teflon stir rod under an enclosed hood. Fill 1 L Teflon beaker with $\sim 1/2$ L of tap water, fill a 500 mL Teflon beaker full with tap water, and fill another 500 mL Teflon beaker full with DI water. Tap water is initially used because, in general, tap

water in Pocatello, ID is more basic than DI water. After HF dissolution, use an ultrasonic bath to clean off any residue precipitated; a Fisher Scientific FS20 Ultrasonic Bath was used for this process.

2. Weigh out a sample of sand-sized material and measure HF in graduated cylinder; a ratio of 1g of sample for every 10mL of 49% HF was used. No more than 10 g of sample was used at a time, since the solution does not mix well with a lot of sample. HF is extremely volatile and hazardous, so keep it underneath the hood. Note: it is useful to label beakers/cylinders with what was used in the container because to the naked eye HF and water are identical. For example, write "HF" on side of beaker used for HF, and "H₂O – tap" on a beaker used for tap water.
3. Pour HF from graduated cylinder into a 500 mL Teflon beaker; pour along the side of the beaker to avoid splashing. Slide Teflon magnetic stir bar on the side of the same beaker to avoid splashing. Place beaker on magnetic plate and spin on mid-range; insure that HF will not overflow when sample is added. Change the spin to a setting suitable for the amount of sample.
4. Slowly add sample to stirring HF and begin timing immediately after the last of the sample is added; the Teflon stir rod may have to be used to force the magnetic stir bar to spin. Dissolution times varied between 4-12 minutes depending on the size of phenocrysts and degree of welding. In general, the best results were produced from 4-7 minute trials.
5. Decant the HF solution into the ~1/2 filled 1L Teflon beaker, avoid losing any sample. Carefully add tap water to the remainder of the sample in the same beaker used for dissolution, filling it ~3/4 full, mix with Teflon stir bar, and decant into 1L

beaker. Repeat two more times, the 1L beaker may fill up, so add the overflow to a 500 mL Teflon beaker. Do this same process with DI water to clean the sample. At this point, the remaining sample is neutralized and clean. Use the Teflon stir rod to remove magnetic stir bar, place both into an empty Teflon beaker.

6. Keep a small amount of DI water in sample Teflon beaker, and transfer sample into the glass beaker next to the ultrasonic bath. Place glass beaker in the center of the ultrasonic bath; make sure water surrounding beaker is high enough to allow the machine to work, but not so high that it over-tops the glass beaker.
7. Sonicate for at least 10 minutes. Then remove glass beaker, decant the DI water, and clean sample two to three times to remove any solute. Filter sample and dry by either air drying or on low on a heat plate.

APPENDIX C: METHOD FOR CALCULATING $\delta^{18}\text{O}$ OF MELT FROM $\delta^{18}\text{O}$ OF PHENOCRYSTS

Unit	Mineral	d $^{13}\text{C}/^{12}\text{C}$ Mean	δ $^{13}\text{C}/^{12}\text{C}$ Std Dev	δ $^{18}\text{O}/^{16}\text{O}$ Mean	δ $^{18}\text{O}/^{16}\text{O}$ Std Dev	Yield (μmol)	$\delta^{18}\text{O}$ (corrected)	s.d.
USGS-142	Pyroxene	-23.924	0.022	3.126	0.049	24	3.197	0.049
USGS-142	Pyroxene	-23.864	0.017	3.379	0.051	13.92	3.45	0.051
East Arco Hills	Pyroxene	-23.936	0.02	4.481	0.032	24.08	4.552	0.032
Butte Quarry	Quartz	-23.935	0.006	4.497	0.019	24.11	4.568	0.019
Butte Quarry	Quartz	-23.955	0.006	2.246	0.019	21.59	2.317	0.019
Butte Quarry	Plagioclase	-23.804	0.004	1.945	0.059	7.5	2.13	0.059

Table C1: Raw data from individual phenocryst analyses.

Method for calculating $\delta^{18}\text{O}$ of melt from $\delta^{18}\text{O}$ of minerals

$$\delta^{18}\text{O} = (R_{\text{Sa}}/R_{\text{Std}} - 1) \times 1000$$

Where R_{Sa} and R_{St} are absolute ratios of $^{18}\text{O}/^{16}\text{O}$ in sample (sa) and standard (std). The standard is Vienna Mean Standard Ocean Water (VSMOW) with $^{18}\text{O}/^{16}\text{O}$ absolute ratios of 0.020052

$$\frac{\delta^{18}\text{O}}{1000} = \frac{R_{\text{sa}}}{R_{\text{std}}} - 1$$

$$\frac{\delta^{18}\text{O}}{1000} + 1 = \frac{R_{\text{sa}}}{R_{\text{std}}}$$

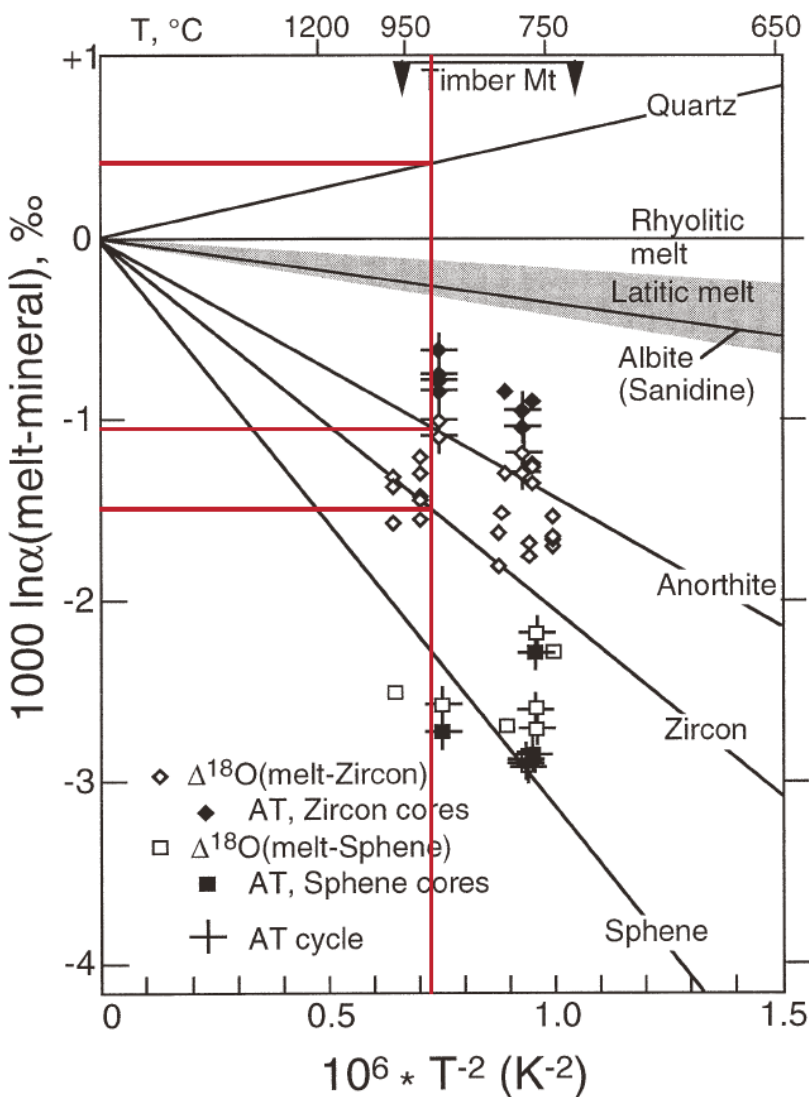
$$\left(\frac{\delta^{18}\text{O}}{1000} + 1\right) R_{\text{std}} = R_{\text{sa}}$$

$$\frac{^{18}\text{O}}{^{16}\text{O}}_{\text{sa}} = \left(\frac{\delta^{18}\text{O}}{1000} + 1\right) \frac{^{18}\text{O}}{^{16}\text{O}}_{\text{std}}$$

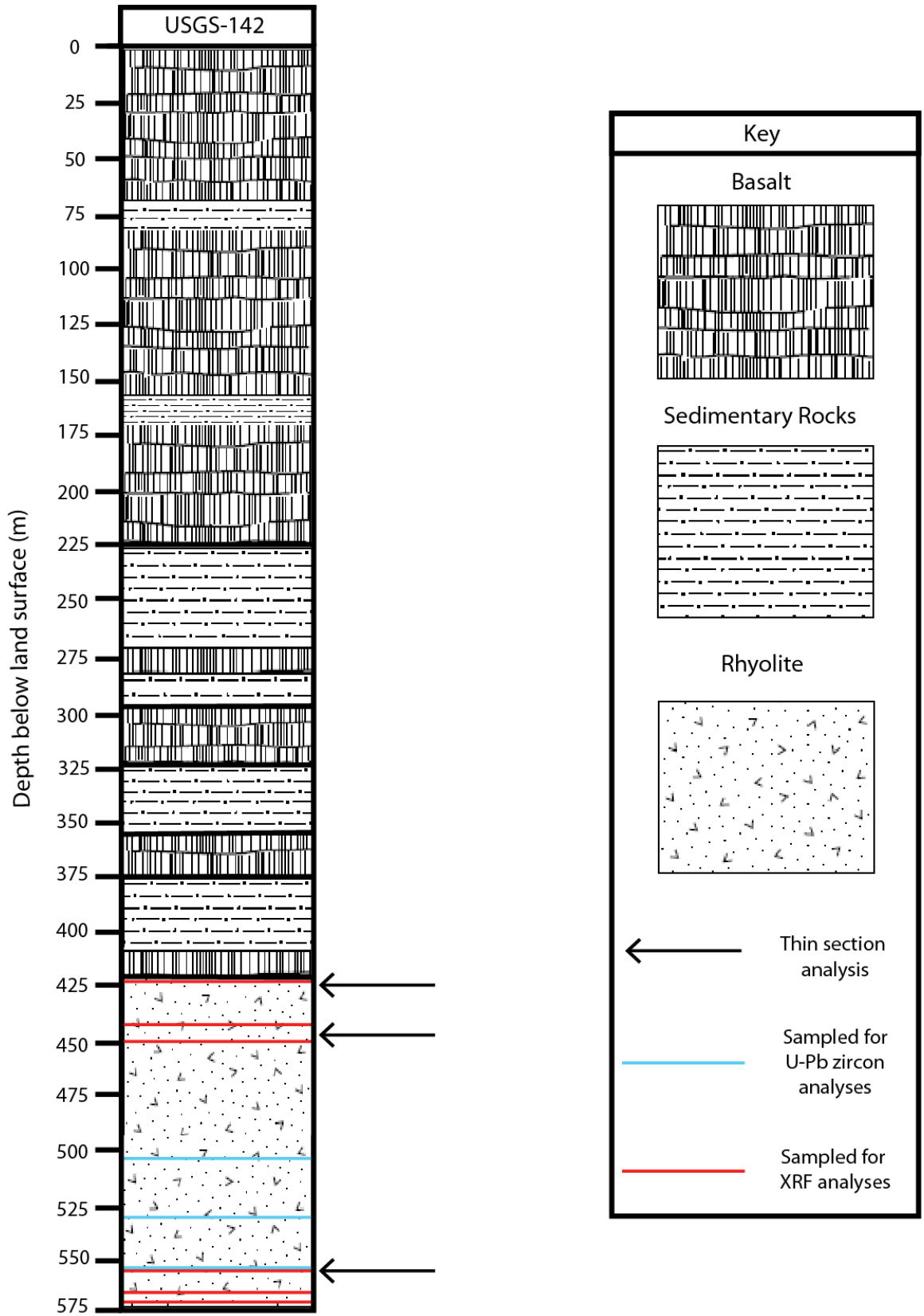
$$1000 \ln \alpha = X \quad \alpha = \frac{R_{\text{melt}}}{R_{\text{sa}}}$$

Where α is the ratio of isotope ratios in two phases, calculated here as the fractionation factor between a rhyolitic melt and a mineral (R_{sa}). X is an interpolated value gathered from figure 4 of Bindeman and Valley (2003) (see below), with units of “per mil” (‰). See figure below from Bindeman and Valley (2003), which illustrates the fractionation factors of selected minerals normalized to a rhyolitic melt as a function of temperature. Extrapolated values from an assumed temperature (900°C used in this study), give values of “ X ”, which can then be used to calculate α and ultimately $\delta^{18}\text{O}_{\text{melt}}$.

$$\alpha = e^{\frac{X}{1000}}$$



APPENDIX D: SIMPLIFIED STRATIGRAPHIC COLUMN OF BOREHOLE USGS-142



APPENDIX E: EIGENVALUES USED FOR CALCULATING FABRIC SHAPE

	Collective Analysis			Distal Domain			Proximal Domain		
	Poles to Fault Planes	Shortening Axes	Extension Axes	Poles to Fault Planes	Shortening Axes	Extension Axes	Poles to Fault Planes	Shortening Axes	Extension Axes
λ_1	0.8515	0.6183	0.6378	0.8753	0.6665	0.718	0.8412	0.6767	0.6411
λ_2	0.0834	0.2778	0.2656	0.0695	0.2205	0.2001	0.0887	0.2638	0.2573
λ_3	0.0651	0.1039	0.0966	0.0552	0.1131	0.0819	0.07	0.0595	0.1016

APPENDIX F: RAW DATA FOR AR-AR AGE DATING

Rhyolite of USGS-142

Summary Results

Sample	USGS-142	Material		Spectrometer	LDEO
Time	6:56:25 AM	Project	Mark Anders	Script	Unknown
Date	3/20/2018	Cleanup	180/0	Heating Device	CO2
Irradiation	USGS84A	Signal Norm.	1	Beam diameter	0.0
37Ar Decay	1.143e+1	Fraction to ms	0	Positions	67
39Ar Decay	1.001e+0	Weight	0	Power Requested	7
Moles 40	1.07e-14	Time at temp.(s)	45	Power Achieved	7.0
I (database irradiation position)	1.758e-3 ± 6.2e-6 (0.35%)	%40Ar*	57.2	Ca/K	5.971 ± 0.038

Isotopes (Na)	Signal	±1 s.d.	% s.d.	Backgrounds	±1 s.d.	% s.d.	Fit	GOF	Bs	Bk	Iso	Det
Ar40	0.480620	± 0.001005	0.21%	0.026137	± 0.0003802	1.5%	L	0.975	0%	14%	86%	MuA
Ar39	0.136298	± 0.000190	0.14%	0.000240	± 0.0000092	3.8%	L	0.994	0%	0%	100%	MuA
Ar38	0.001897	± 0.000031	1.61%	0.000269	± 0.0000096	3.6%	L	0.762	0%	10%	90%	MuA
Ar37	0.036278	± 0.000160	0.44%	0.000091	± 0.0000074	8.1%	L	0.987	0%	0%	100%	MuA
Ar36	0.000806	± 0.000018	2.21%	0.000847	± 0.0000096	1.1%	L	0.276	0%	29%	71%	MuA
Multiplier Baseline	0.000030	± 0.000001	3.07%				A	0.000				MuA
Ar40/Ar36	0.00000e+0	± 0.0e+0	----		0.000							
Ar40/Ar38	0.00000e+0	± 0.0e+0	----		0.000							
AGE (Ma)	6.3855	± 0.1339	2.10%									
Monte Carlo int. err.		± 0.1359	2.13%									
Excluding error in I		± 0.1320	2.07%									

Rhyolite of the east side of the Arco Hills

Summary Results

Sample	16KS01	Material		Spectrometer	LDEO
Time	7:31:36 AM	Project	Mark Anders	Script	Unknown
Date	3/20/2018	Cleanup	180/0	Heating Device	CO2
Irradiation	USGS84A	Signal Norm.	1	Beam diameter	0.0
37Ar Decay	1.144e+1	Fraction to ms	0	Positions	68
39Ar Decay	1.001e+0	Weight	0	Power Requested	7
Moles 40	3.77e-14	Time at temp.(s)	45	Power Achieved	7.0
I (database irradiation position)	1.758e-3 ± 6.2e-6 (0.35%)	%40Ar*	68.4	Ca/K	2.349 ± 0.015

Isotopes (Na)	Signal	±1 s.d.	% s.d.	Backgrounds	±1 s.d.	% s.d.	Fit	GOF	Bs	Bk	Iso	Det
Ar40	1.695477	± 0.001258	0.07%	0.026294	± 0.0003773	1.4%	L	0.995	0%	9%	91%	MuA
Ar39	0.552999	± 0.000550	0.10%	0.000240	± 0.0000091	3.8%	L	0.997	0%	0%	100%	MuA
Ar38	0.007464	± 0.000059	0.79%	0.000269	± 0.0000092	3.4%	L	0.939	0%	2%	98%	MuA
Ar37	0.057955	± 0.000250	0.43%	0.000090	± 0.0000077	8.5%	L	0.989	0%	0%	100%	MuA
Ar36	0.001981	± 0.000023	1.16%	0.000848	± 0.0000092	1.1%	L	0.037	0%	16%	84%	MuA
Multiplier Baseline	0.000036	± 0.000001	2.44%				A	0.000				MuA
Ar40/Ar36	0.00000e+0	± 0.0e+0	----		0.000							
Ar40/Ar38	0.00000e+0	± 0.0e+0	----		0.000							
AGE (Ma)	6.6300	± 0.0535	0.81%									
Monte Carlo int. e.		± 0.0535	0.81%									
Excluding error in I		± 0.0480	0.72%									

APPENDIX G: MEASURED NORTHEAST-STRIKING FAULTS OF THE ARCO HILLS

Strike	Dip	Striation		Shortening Axis		WGS - 84	
		Trend	Plunge	Trend	Plunge	Latitude	Longitude
15	90	195.0	83.7	278.8	44.7	43.62297	-113.22020
18	90	198.0	76.1	274.5	43.4	43.62252	-113.20915
20	85	34.2	70.4	309.6	46.7	43.61359	-113.21520
30	85	158.7	83.6	295.6	49.8	43.63593	-113.24730
30	85	187.7	77.0	287.1	48.6	43.61568	-113.19140
30	70	48.9	41.6	345.4	45.4	43.62259	-113.20226
30	71	155.3	67.1	280.3	61.8	43.61768	-113.19199
32	84	161.9	82.2	296.4	50.8	43.62297	-113.22020
35	63	55.9	34.9	357.0	46.6	43.67931	-113.17419
35	65	153.6	62.0	280.5	67.4	43.68375	-113.18321
35	85	179.6	81.4	297.4	49.5	43.62297	-113.22020
38	67	164.3	62.2	281.2	64.4	43.61633	-113.21127
39	90	39.0	73.0	325.3	42.5	43.65214	-113.17106
40	81	142.6	80.8	307.6	54.0	43.61333	-113.19016
40	84	206.8	65.3	285.7	45.8	43.61496	-113.19265
50	79	176.4	76.4	310.0	55.3	43.62368	-113.19122
53	89	54.6	58.0	351.3	37.7	43.66405	-113.17027
55	64	113.6	60.2	353.6	67.5	43.68100	-113.17955
68	85	75.9	57.7	7.9	41.2	43.65916	-113.17979
70	90	70.0	63.0	4.4	39.1	43.67525	-113.16675
70	78	150.5	77.8	342.6	57.0	43.63581	-113.24690
75	83	217.4	78.6	334.8	51.2	43.62368	-113.19122
80	68	228.1	52.6	309.6	55.8	43.62157	-113.20817
195	61	251.0	56.0	141.8	68.6	43.61359	-113.21520
210	82	19.9	51.3	85.0	40.6	43.68263	-113.17897
214	85	26.4	56.7	93.5	40.7	43.68236	-113.17683
214	65	287.8	64.1	138.1	69.2	43.61085	-113.19135
215	81	237.2	67.2	148.1	49.7	43.62113	-113.20836
218	84	19.1	72.0	109.9	48.3	43.61568	-113.19140
220	82	29.9	51.3	95.0	40.6	43.66615	-113.17206
220	79	281.2	77.5	137.5	55.6	43.68598	-113.18509
222	88	231.3	77.8	144.2	45.7	43.64631	-113.15325
225	86	6.4	83.6	129.6	48.8	43.68030	-113.17657
225	73	346.1	70.4	120.4	60.8	43.69157	-113.16199
225	85	236.6	66.5	158.1	45.2	43.69963	-113.17758
225	55	308.0	54.8	150.8	79.5	43.64858	-113.15368
230	58	17.7	40.5	84.5	56.5	43.68839	-113.16876
230	72	263.5	59.5	172.2	55.9	43.69963	-113.17758
230	74	6.1	67.5	118.4	58.0	43.62052	-113.19513
235	82	34.1	68.5	123.3	49.1	43.69239	-113.17492
235	83	348.3	82.4	141.6	51.9	43.69608	-113.17347
235	64	7.7	56.4	107.7	64.1	43.68729	-113.18972
240	82	330.0	82.0	150.0	53.0	43.64076	-113.15025
243	50	285.6	38.9	220.3	63.9	43.61329	-113.19011
245	74	280.7	63.8	182.0	56.0	43.64068	-113.15018
250	72	286.1	61.1	190.4	56.9	43.64068	-113.15018
252	80	57.6	54.7	128.4	44.4	43.68003	-113.16413
255	88	258.0	55.9	195.0	37.6	43.68777	-113.16739
255	75	295.2	67.5	187.1	56.7	43.68814	-113.16921
255	86	276.6	79.2	175.6	48.1	43.62354	-113.19196

APPENDIX H: DATA TABLES FOR U-Pb, Hf, AND CATHODOLUMINESCENCE (CL) IMAGES OF ZIRCONS

Data tables for U-Pb zircon ages

Rhyolite of Butte Quarry																		
Analysis	U	206Pb	U/Th	206Pb*	±	207Pb*	±	206Pb*	±	error	206Pb	±	207Pb*	±	206Pb*	±	Best age	±
	(ppm)	204Pb		207Pb*	(%)	235U*	(%)	238U	(%)	corr.	238U*	(Ma)	235U	(Ma)	207Pb*	(Ma)	(Ma)	(Ma)
-SAMPLE 1 Spot 29	2194	34388	1.3	20.8070	1.6	0.0077	2.1	0.0012	1.3	0.62	7.4	0.1	7.7	0.2	101.2	38.5	7.4	0.1
-SAMPLE 1 Spot 3	60	571	1.3	36.9105	51.0	0.0044	51.1	0.0012	3.6	0.07	7.5	0.3	4.4	2.3	NA	NA	7.5	0.3
-SAMPLE 1 Spot 27	41	738	1.5	79.4877	6.5	0.0021	8.1	0.0012	4.7	0.58	7.7	0.4	2.1	0.2	NA	NA	7.7	0.4
-SAMPLE 1 Spot 19	51	427	1.5	37.3473	54.2	0.0044	54.3	0.0012	3.2	0.06	7.7	0.2	4.5	2.4	NA	NA	7.7	0.2
-SAMPLE 1 Spot 20	1427	7874	1.4	22.0468	1.8	0.0075	2.3	0.0012	1.5	0.65	7.7	0.1	7.6	0.2	NA	NA	7.7	0.1
-SAMPLE 1 Spot 9	49	401	1.4	48.6912	10.5	0.0035	10.9	0.0012	2.8	0.26	7.9	0.2	3.5	0.4	NA	NA	7.9	0.2
-SAMPLE 1 Spot 16	156	810	1.1	23.4534	17.9	0.0072	18.0	0.0012	1.8	0.10	7.9	0.1	7.3	1.3	NA	NA	7.9	0.1
-SAMPLE 1 Spot 10	125	2410	1.5	23.2067	5.9	0.0074	6.2	0.0012	1.8	0.30	8.0	0.1	7.5	0.5	NA	NA	8.0	0.1
-SAMPLE 1 Spot 26	934	16673	1.1	20.1172	2.6	0.0086	2.9	0.0013	1.3	0.45	8.1	0.1	8.7	0.2	180.4	60.4	8.1	0.1
-SAMPLE 1 Spot 25	160	3144	1.0	25.3268	4.9	0.0068	5.2	0.0013	1.9	0.37	8.1	0.2	6.9	0.4	NA	NA	8.1	0.2
-SAMPLE 1 Spot 28	41	420	1.6	68.9274	8.4	0.0025	9.0	0.0013	3.3	0.36	8.1	0.3	2.5	0.2	NA	NA	8.1	0.3
-SAMPLE 1 Spot 4	56	350	1.5	208.3643	148.1	0.0008	148.1	0.0013	3.6	0.02	8.1	0.3	0.8	1.2	NA	NA	8.1	0.3
-SAMPLE 1 Spot 15	54	304	1.3	41.1340	107.9	0.0043	108.0	0.0013	2.7	0.03	8.2	0.2	4.3	4.6	NA	NA	8.2	0.2
-SAMPLE 1 Spot 24	55	697	1.8	88.5173	15.7	0.0020	15.9	0.0013	2.4	0.15	8.2	0.2	2.0	0.3	NA	NA	8.2	0.2
-SAMPLE 1 Spot 8	102	559	1.9	180.6871	179.9	0.0010	179.9	0.0013	2.4	0.01	8.2	0.2	1.0	1.8	NA	NA	8.2	0.2
-SAMPLE 1 Spot 33	47	480	1.7	43.4212	21.0	0.0041	21.1	0.0013	2.4	0.11	8.2	0.2	4.1	0.9	NA	NA	8.2	0.2
-SAMPLE 1 Spot 7	35	436	1.5	360.5103	317.4	0.0005	317.4	0.0013	3.8	0.01	8.3	0.3	0.5	1.6	NA	NA	8.3	0.3
-SAMPLE 1 Spot 35	30	668	1.6	12.5936	13.6	0.0142	14.2	0.0013	4.1	0.29	8.3	0.3	14.3	2.0	1181.4	269.3	8.3	0.3
-SAMPLE 1 Spot 23	38	2647	1.4	14.2194	10.8	0.0126	11.5	0.0013	4.0	0.35	8.4	0.3	12.8	1.5	937.0	222.4	8.4	0.3
-SAMPLE 1 Spot 5	59	432	1.4	31.7190	16.4	0.0057	16.6	0.0013	2.8	0.17	8.5	0.2	5.8	1.0	NA	NA	8.5	0.2
-SAMPLE 1 Spot 31	105	1353	1.6	29.8918	10.5	0.0062	10.7	0.0013	2.2	0.20	8.6	0.2	6.2	0.7	NA	NA	8.6	0.2
-SAMPLE 1 Spot 2	40	1895	1.6	39.0506	6.2	0.0047	6.8	0.0013	3.0	0.44	8.7	0.3	4.8	0.3	NA	NA	8.7	0.3
-SAMPLE 1 Spot 30	43	1523	1.7	23.5726	8.3	0.0079	9.0	0.0013	3.3	0.37	8.7	0.3	8.0	0.7	NA	NA	8.7	0.3
-SAMPLE 1 Spot 34	108	817	1.3	27.1530	10.9	0.0069	11.2	0.0014	2.3	0.21	8.8	0.2	7.0	0.8	NA	NA	8.8	0.2
-SAMPLE 1 Spot 18	835	8060	1.4	22.1482	2.1	0.0091	2.5	0.0015	1.3	0.51	9.4	0.1	9.2	0.2	NA	NA	9.4	0.1
-SAMPLE 1 Spot 13	55	1481	1.6	42.9412	7.1	0.0049	20.2	0.0015	18.9	0.94	9.9	1.9	5.0	1.0	NA	NA	9.9	1.9
-SAMPLE 1 Spot 12	109	7324	2.1	5.9943	23.6	0.0393	24.9	0.0017	8.0	0.32	11.0	0.9	39.1	9.6	2525.3	401.7	11.0	0.9
-SAMPLE 1 Spot 21	36	5712	1.6	24.8625	6.2	0.0104	30.6	0.0019	30.0	0.98	12.1	3.6	10.5	3.2	NA	NA	12.1	3.6
-SAMPLE 1 Spot 22	47	1877	1.8	2.8250	44.7	0.1063	45.8	0.0022	10.2	0.22	14.0	1.4	102.6	44.8	3723.6	1574.9	14.0	1.4
-SAMPLE 1 Spot 6	39	288	1.4	1.8294	50.0	0.2576	50.2	0.0034	4.3	0.09	22.0	0.9	232.8	104.8	4371.5	NA	22.0	0.9

Rhyolite of USGS-142																		
Analysis	U	206Pb	U/Th	206Pb*	±	207Pb*	±	206Pb*	±	error	206Pb	±	207Pb*	±	206Pb*	±	Best age	±
	(ppm)	204Pb		207Pb*	(%)	235U*	(%)	238U	(%)	corr.	238U*	(Ma)	235U	(Ma)	207Pb*	(Ma)	(Ma)	(Ma)
-Sample 2 Spot 40	143	258	1.5	33.5165	35.1	0.0037	35.2	0.0009	2.5	0.07	5.8	0.1	3.7	1.3	NA	NA	5.8	0.1
-Sample 2 Spot 61	131	392	1.7	907.4241	#####	0.0001	1880.5	0.0009	2.6	0.00	6.0	0.2	0.1	2.7	NA	NA	6.0	0.2
-Sample 2 Spot 47	129	483	1.2	27.0262	8.8	0.0047	9.1	0.0009	2.3	0.26	6.0	0.1	4.8	0.4	NA	NA	6.0	0.1
-Sample 2 Spot 60	175	1169	1.3	27.5936	18.7	0.0047	18.8	0.0009	1.6	0.08	6.1	0.1	4.8	0.9	NA	NA	6.1	0.1
-Sample 2 Spot 38	171	702	1.2	47.0502	10.0	0.0028	10.3	0.0010	2.1	0.21	6.2	0.1	2.8	0.3	NA	NA	6.2	0.1
-Sample 2 Spot 43	151	968	1.5	30.0180	9.8	0.0044	10.0	0.0010	2.1	0.20	6.2	0.1	4.5	0.5	NA	NA	6.2	0.1
-Sample 2 Spot 42	124	1606	1.6	38.0854	11.7	0.0035	11.9	0.0010	2.2	0.19	6.3	0.1	3.6	0.4	NA	NA	6.3	0.1
-Sample 2 Spot 39	119	383	1.5	242.2313	69.2	0.0006	69.3	0.0010	2.1	0.03	6.3	0.1	0.6	0.4	NA	NA	6.3	0.1
-Sample 2 Spot 48	147	2010	1.3	20.3986	6.4	0.0066	6.7	0.0010	1.8	0.27	6.3	0.1	6.7	0.4	147.9	151.2	6.3	0.1
-Sample 2 Spot 58	117	506	1.3	37.5378	33.9	0.0036	34.0	0.0010	2.5	0.07	6.3	0.2	3.6	1.2	NA	NA	6.3	0.2
-Sample 2 Spot 46	207	884	1.5	19.0245	17.7	0.0071	17.8	0.0010	1.8	0.10	6.3	0.1	7.2	1.3	309.0	406.5	6.3	0.1
-Sample 2 Spot 45	188	528	1.3	38.6521	9.4	0.0035	9.6	0.0010	1.9	0.20	6.3	0.1	3.6	0.3	NA	NA	6.3	0.1
-Sample 2 Spot 44	161	409	1.4	70.8676	11.5	0.0019	11.7	0.0010	2.1	0.18	6.4	0.1	1.9	0.2	NA	NA	6.4	0.1
-Sample 2 Spot 56	147	938	1.6	22.2161	20.0	0.0062	20.1	0.0010	2.5	0.12	6.4	0.2	6.2	1.3	NA	NA	6.4	0.2
-Sample 2 Spot 55	167	860	1.4	15.0397	9.1	0.0092	9.3	0.0010	1.6	0.17	6.5	0.1	9.3	0.9	821.0	191.0	6.5	0.1
-Sample 2 Spot 59	187	1001	1.3	27.4439	6.0	0.0050	6.2	0.0010	1.8	0.29	6.5	0.1	5.1	0.3	NA	NA	6.5	0.1
-Sample 2 Spot 37	145	5986	1.7	21.0548	5.7	0.0067	6.1	0.0010	2.2	0.36	6.6	0.1	6.8	0.4	73.1	135.7	6.6	0.1
-Sample 2 Spot 36	184	1283	1.3	9.0994	13.8	0.0162	14.1	0.0011	2.9	0.21	6.9	0.2	16.3	2.3	1796.9	252.1	6.9	0.2
-Sample 2 Spot 41	270	1443	1.3	18.6035	8.0	0.0080	8.2	0.0011	1.5	0.18	7.0	0.1	8.1	0.7	359.7	181.7	7.0	0.1

Rhyolite of Butte Quarry

Sample	$(^{176}\text{Yb} + ^{176}\text{Lu}) / ^{176}\text{Hf}$ (%)	Volts Hf	$^{176}\text{Hf}/^{177}\text{Hf}$	\pm (1 σ)	$^{176}\text{Lu}/^{177}\text{Hf}$	$^{176}\text{Hf}/^{177}\text{Hf}$ (T)	E-Hf (O)	E-Hf (O) \pm (1 σ)	E-Hf (T)	Age (Ma)
17KS03-SPOT25	26.6	3.7	0.282717	0.000021	0.001693	0.282717	-2.4	0.7	-2.2	8
17KS03-SPOT28	9.1	4.2	0.282615	0.000022	0.000549	0.282615	-6.0	0.8	-5.8	8
17KS03-SPOT24	10.6	4.5	0.282615	0.000020	0.000648	0.282615	-6.0	0.7	-5.8	8
17KS03-SPOT8	12.1	4.0	0.282624	0.000021	0.000687	0.282624	-5.7	0.8	-5.5	8
17KS03-SPOT33	15.6	4.2	0.282636	0.000017	0.000920	0.282636	-5.3	0.6	-5.1	8
17KS03-SPOT7	11.5	4.1	0.282619	0.000020	0.000688	0.282619	-5.9	0.7	-5.7	8
17KS03-SPOT23	11.3	4.0	0.282566	0.000020	0.000676	0.282566	-7.7	0.7	-7.6	8
17KS03-SPOT5	14.5	4.0	0.282659	0.000018	0.000853	0.282659	-4.5	0.6	-4.3	9
17KS03-SPOT31	15.7	4.2	0.282553	0.000019	0.000923	0.282553	-8.2	0.7	-8.0	9
17KS03-SPOT2	9.8	4.2	0.282626	0.000025	0.000589	0.282626	-5.6	0.9	-5.4	9
17KS03-SPOT12	20.9	3.7	0.282643	0.000018	0.001005	0.282643	-5.0	0.6	-4.8	11
17KS03-SPOT21	9.1	4.2	0.282599	0.000025	0.000554	0.282599	-6.6	0.9	-6.3	12
17KS03-SPOT22	11.5	4.7	0.282630	0.000014	0.000688	0.282630	-5.5	0.5	-5.2	14
17KS03-SPOT6	10.8	4.0	0.282716	0.000023	0.000698	0.282716	-2.4	0.8	-1.9	22

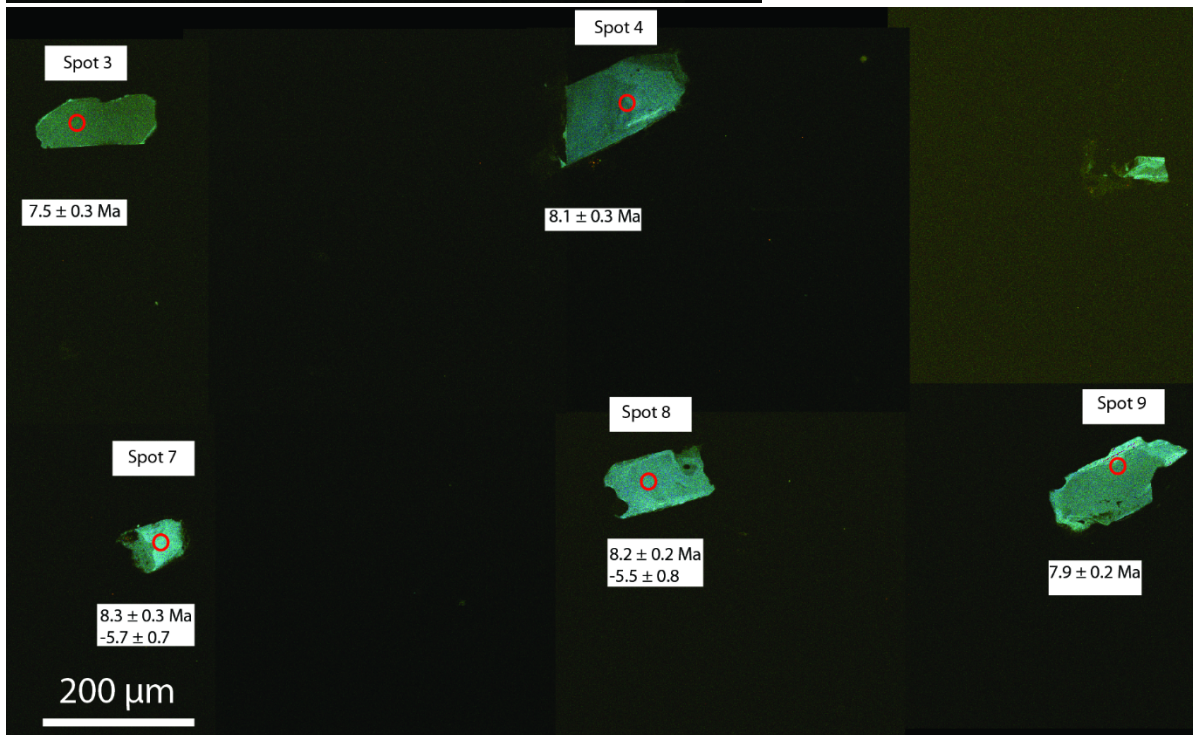
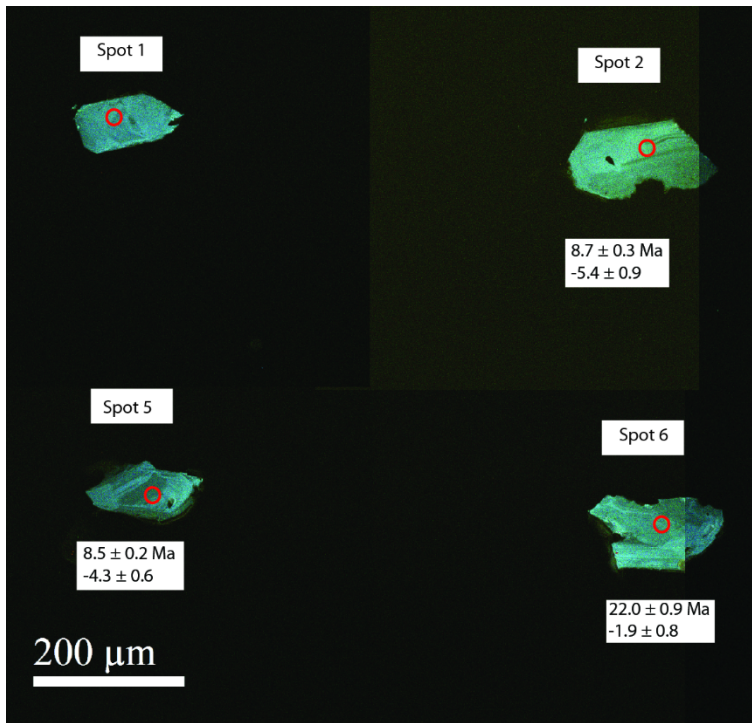
Rhyolite of USGS-142

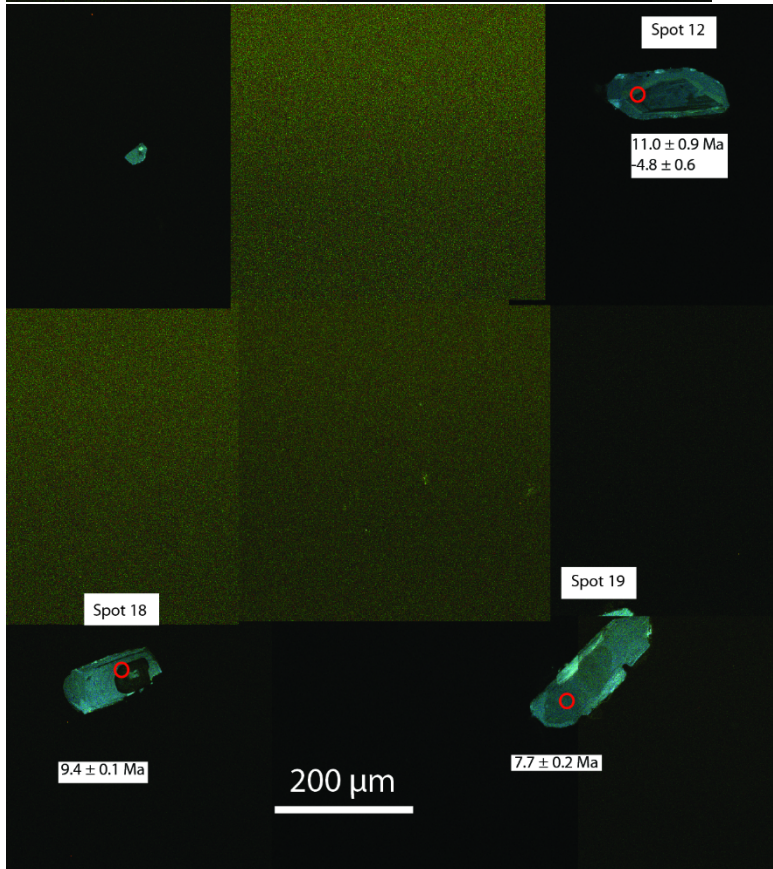
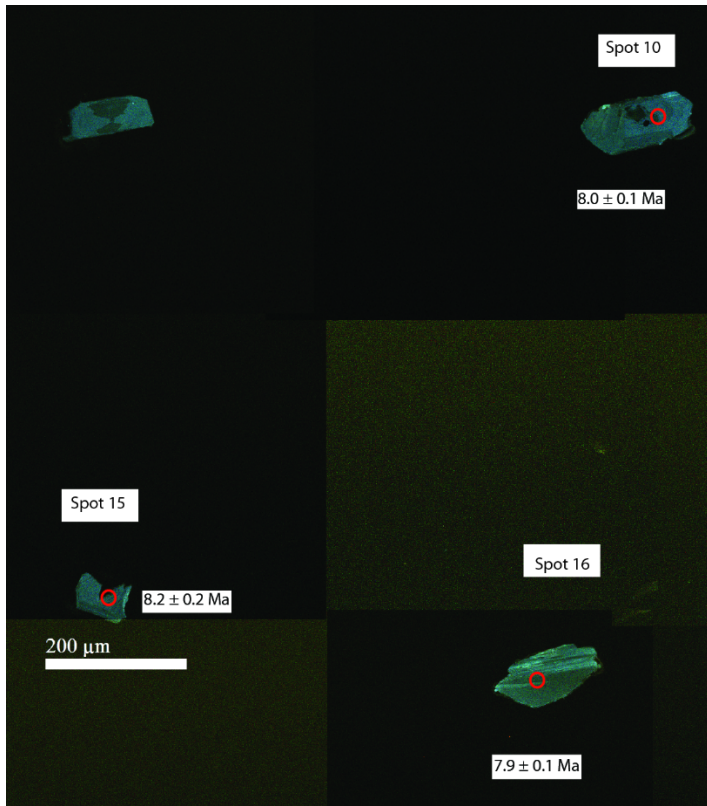
Sample	$(^{176}\text{Yb} + ^{176}\text{Lu}) / ^{176}\text{Hf}$ (%)	Volts Hf	$^{176}\text{Hf}/^{177}\text{Hf}$	\pm (1 σ)	$^{176}\text{Lu}/^{177}\text{Hf}$	$^{176}\text{Hf}/^{177}\text{Hf}$ (T)	E-Hf (O)	E-Hf (O) \pm (1 σ)	E-Hf (T)	Age (Ma)
USGS142-SPOT38	26.8	4.0	0.282531	0.000023	0.001545	0.282531	-9.0	0.8	-8.8	6
USGS142-SPOT43	24.4	4.4	0.282479	0.000022	0.001429	0.282479	-10.8	0.8	-10.7	6
USGS142-SPOT42	23.4	4.5	0.282507	0.000016	0.001385	0.282507	-9.8	0.6	-9.7	6
USGS142-SPOT39	17.5	4.2	0.282578	0.000017	0.001040	0.282578	-7.3	0.6	-7.2	6
USGS142-SPOT48	25.2	4.3	0.282562	0.000018	0.001485	0.282562	-7.9	0.7	-7.8	6
USGS142-SPOT58	25.2	4.3	0.282626	0.000022	0.001484	0.282626	-5.6	0.8	-5.5	6
USGS142-SPOT46	28.4	4.2	0.282559	0.000019	0.001673	0.282559	-8.0	0.7	-7.8	6
USGS142-SPOT44	22.5	4.2	0.282511	0.000023	0.001319	0.282511	-9.7	0.8	-9.6	6
USGS142-SPOT56	23.0	3.5	0.282219	0.000023	0.001339	0.282219	-20.0	0.8	-19.9	6
USGS142-SPOT55	22.1	4.4	0.282513	0.000017	0.001261	0.282513	-9.6	0.6	-9.5	7
USGS142-SPOT59	24.8	4.6	0.282534	0.000021	0.001460	0.282534	-8.9	0.7	-8.7	7
USGS142-SPOT37	26.9	5.0	0.282560	0.000022	0.001586	0.282560	-8.0	0.8	-7.8	7

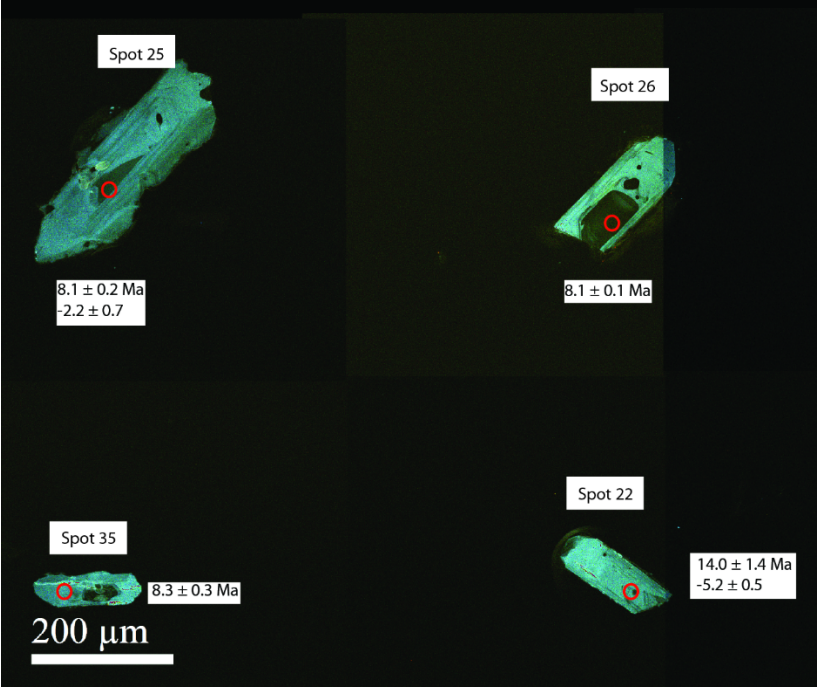
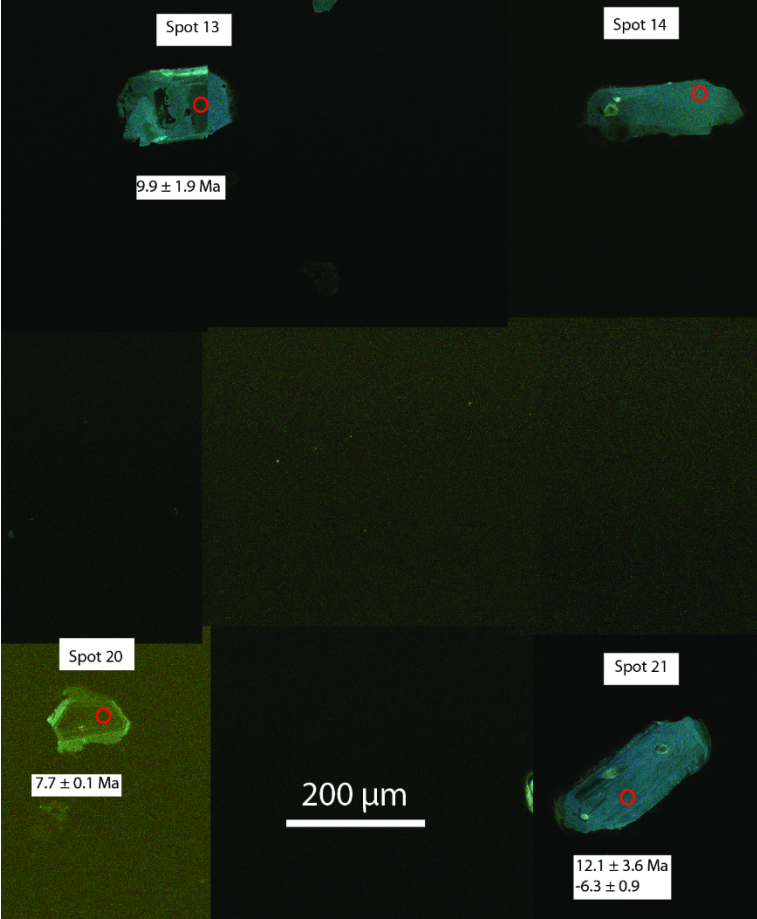
Data tables for Hf analyses

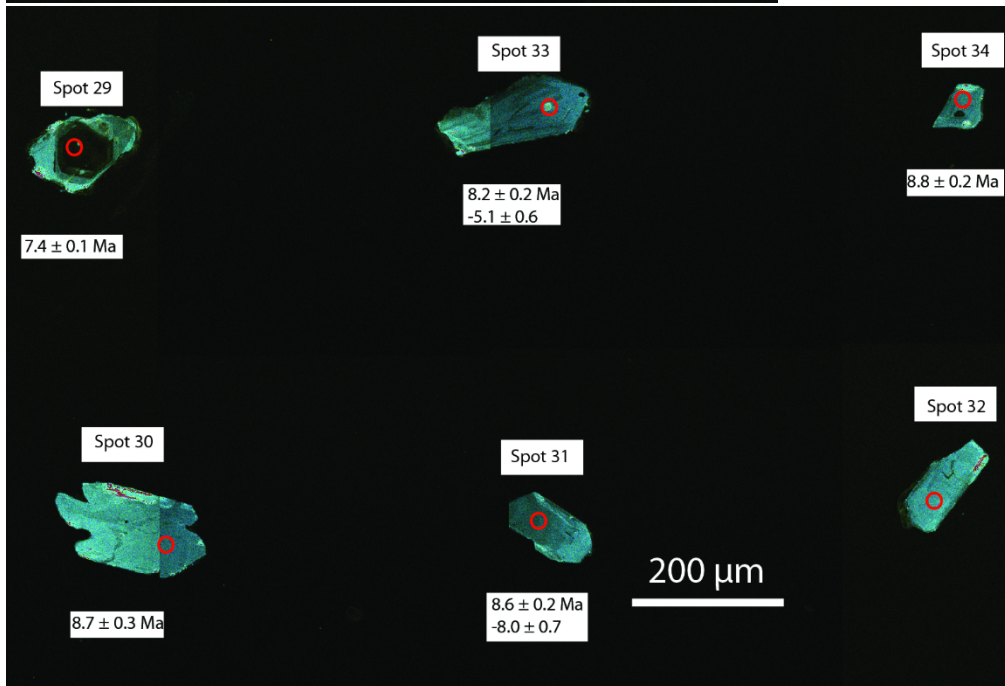
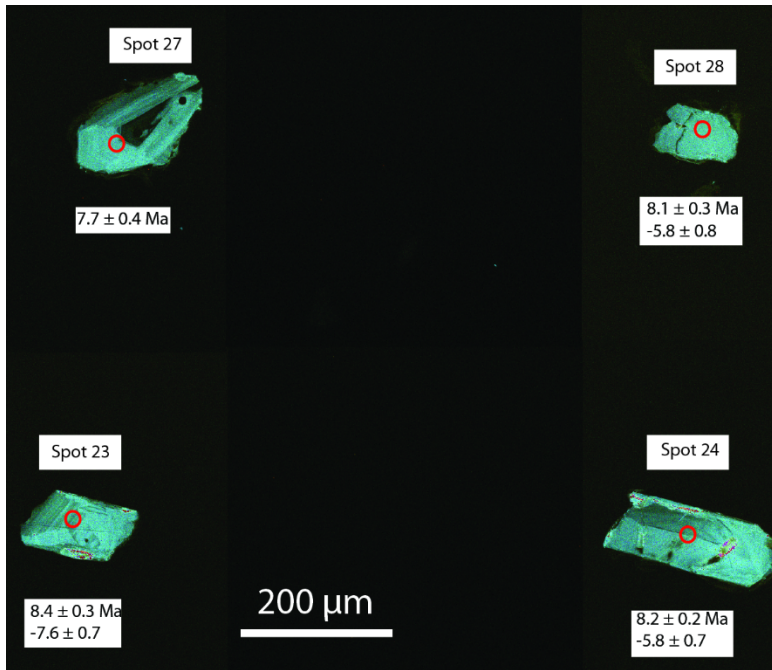
CL images with spot locations

Rhyolite of Butte Quarry









Rhyolite of USGS-142

